Study of turbulent dispersion modelling effects on dispersed multiphase flows properties

Vom Fachbereich Maschinenbau
an der Technischen Universität Darmstadt
zur
Erlangung des Grades eines Doktor-Ingenieurs (Dr.-Ing.)
genehmigte

Dissertation

vorgelegt von

Dipl.-Ing. Wahidullah Ahmadi

aus Kabul (Jalrez Maidan), Afghanistan

Berichterstatter:	Prof. Dr.-Ing. J. Janicka
Mitberichterstatter:	Prof. Dr. rer. nat. A. Sadiki
Mitberichterstatter:	Prof. Dr.-Ing. Bernd Epple
Tag der Einreichung:	5. Februar 2013
Tag der mündlichen Prüfung:	04. June 2013

D-17, Darmstadt 2013

Hiermit erkläre ich an Eides Statt, dass ich die vorliegende Dissertation selbstständig verfasst und keine anderen als die von mir angegebenen Hilfsmittel verwendet habe. Ich erkläre außerdem, dass ich bisher noch keinen Promotionsversuch unternommen habe.

Wahidullah Ahmadi

Darmstadt, den 25. Januar 2013

" Habe Mut, dich deines eigenen Verstandes zu bedienen."
(Immanuel Kant, 1784)

" If you repeatedly dive it will come to your hand Who said that there is no pearl in the ocean."
(Khushal Khan Khattak, 1613-1689)

Acknowledgements

The present work has been done during my 3 years scientific work at the Institute of Energy and Power Plant Technology, Darmstadt University of Technology.
First of all I would like to thank my supervisor as head of the department Prof. Dr.-Ing. Johannes Janicka, for giving me the opportunity of promotion and for providing me with the optimum work conditions. I also would like to thank, my closest supervisor, Prof. Dr. Amsini Sadiki for his very kind and excellent guidance and constant encouragement. His enthusiasm and patience have been a source of inspiration throughout the course of this work. Many thanks are due to Prof. Dr.-Ing. B. Epple for his interest by taking over the referee process.

I would like to thank Dr.-Ing. Mouldi Chrigui, Pradeep Pantangi and especially my friend and colleague Dr.-Ing. Amir Mehdizadeh, with whom I had very good teamwork as well as a very useful guidness throughout my scientific work including a very good cooperation and useful professional discussions

My appreciations are also extended to a number of my colleagues for useful discussions and suggestions as well as their technical and moral support during my time in Darmstadt. In particular I would like to thank Dipl. -Ing. Benjamin Börk, Dipl -Ing. Thabo Stahler, Dipl.-Ing Kaushal Nishad, Dipl. -Ing Arash Hosseinzadeh and MSc Amer Avdic̀.

Last, but not least, I would like to thank my family. My parents, who parent and motivate me to become that person, what I am now. Due to this a big part of this work and my special thanks belong to them. I would like to thank also my brothers (especially Mirwais and Shafi and Shahir) and sisters for their motivation, heartiness and oppenness, which can only be done by brothers and sisters.

A lot of thanks to my dear wife Shabnam for having so much patience and faith in me to finish my work, which gives me the possibility to reach my goals in my life.

Darmstadt, January 2013 Wahidullah Ahmadi

Abstract

The recent trend in energy research sought for a gas turbine combustor with highest possible thermal efficiency in compliance with the present environment regulation norms. Such a design improvement requires a detailed understanding of all the physical process involved from the air intake to turbine compressor to final exhaust. The CFD is one of the most widely used technique for design and process optimization of gas turbine, that considerably reduces the cost involved and overall design time line. The fuel injection is one of the vital process that determine the course of combustion inside the combustion chamber as it is primarily responsible for the fuel-air mixture formation and subsequent combustion. The fuel injection itself is a complex process that is highly turbulence in nature and mean time it undergoes different kind of physical phenomena such as such as breakup (atomization), dispersion, evaporation and subsequent combustion.

The present thesis work is mainly on the development and application of different mathematical sub-models to describe the physics of turbulent spray, which is typical for gas turbine combustors. The applied models were formulated in the Eulerian-Lagrangian context in Lag-3D code and coupled with FASTEST code as a gas phase solver.

In order to quantify the instantaneous velocity seen by the particle as it appears in the particle motion equation and its effect on the particle distribution, dispersion model is needed. Turbulent dispersion is very important which influences the particle trajectories that are especially important when evaporation takes place. In the present thesis, three dispersion models, namely RWM-Iso, RWM-Aniso and PLM, are integrated and compared in this work. Furthermore a systematical study of different dispersion models and their influence on mass transfer and different turbulent intensities has been satisfactory carried out.

The results show that the PLM is able to achieve better results with respect to radial mean velocities, mean diameter and axial mean velocity fluctuations of droplets. So the simulations have shown that the PLM model allows for achieving results that agree very well with the experimental measurement of the droplet mass flux in particular in upper sections. This means that the consideration of the advanced dispersion models like PLM enables to account well for anisotropic turbulence as well as vortex structures inherent to complex turbulent two phase flows.

In order to capture well the unsteady dynamics using RANS calculation, a modified SAS model has been adopted and compared with the standard k-ϵ model. Comparisons with experimental data shows that the SAS model is able to capture well the overall flow dynamics.

To represent the actual atomization dynamics for the dispersed phase in vicinity of particle injection nozzle, a stochastic model of drops air-blast breakup following the Kolmogorov´s model is implemented first time in Lag-3D and respective improvement is shown in the results.

Kurzfassung

Der Trend in Energie-Forschung ist den Wirkungsgrad (z.B bei Gasturbinen, Verbrennungsmotoren) zu erhöhen und gleichzeitig die schädlichen Emissionen, die bei der Verbrennung entstehen, zu senken. Für dieses Vorhaben ist das Verständniss der grundlegenden physikalischen Prozesse von Eintritt der Luft im Brennkammer bis zum Austritt der Abgase aus dem Brennkammer von großer Bedeutung. CFD (Computational Fluid Dynamics) ist ein zeit- und geldsparender Technique, um die obengenannten Ziele zu erreichen.
Hierrin ist die Brennstoffzerstäubung ein wichtiger Prozess sowohl für die Gemischbildung als auch für die nachfolgende Verbrennung in dem Brennkammer. Schon die Zerstäubung der flüssigen Brennstoffe is ein komplexer Prozess, der zusätzlich mit Zerstäubung, Dispersion, Verdampfung und Verbrennung behaftet ist.

In dieser Arbeit ist der Hauptfokus auf die Entwicklung und Verwendung von verschiedenen Untermodelle gelegen, um die physikalischen Prozesse bei der turbulenten Sprayverbrennung im Gasturbinen-Kontext zu untersuchen. Die verwendeten Modelle wurden in Eulerian-Lagrangian-Kotext durchgeführt. Für die Gasphase wurde der Code FASTEST und für die disperse Phase den Code LAG3D verwendet.

Turbulente Dispersion beeinflusst die Partikel-Trajektorie und wird insbesondere wichtig, wenn Verdampfung eine grosse Rolle spielt. Um die instantane Geschwindigkeit des Fluidfeldes an der Stelle des Partikels, welche für die Berechnung der Tropfen-Bewegungsgleichung wichtig ist, zu bistimmen, wird ein Dispersionsmodells benötigt.

In der vorliegenden Arbeit wurden 3 Dispersionsmodelle, RWM-Iso, RWM-Aniso und PLM, zusammengefasst und miteinander verglichen. Für den Vergleich wurden 3 Konfiguration herangezogen, um die Modelle in unterschiedlichen instationäre Intensitäten zu testen und zu vergleichen.

Die erste Konfiguration war ein Vertikal Kanal, wo die instationäre Effekte vergleichsweise niedrig waren. Der Vergleich von berechneten und experimentellen Daten für Partikelgeschwindigkeit und Partikelgeschwindigkeitsfluktuationen im Inlet-Bereich der Konfiguration zeigte für alle drei Modelle gleich gute Übereinstimmung. Weit weg von dem Inlet-Bereich leistete PLM bessere Übereinstimmung mit den experimentellen Daten. Die RWMs lieferten dagegen in diesem Bereich konstante Fluktuationen.

Um mehr Instationarität im RANS-Kontext zu bekommen, wurde eine modifizierte SAS Modell adaptiert und mit standard k-ϵ Model verglichen. Der Vergleich mit den experimentellen Daten zeigt, dass SAS Modell die turbulenten Strukturen gut lösen kann.

Um die Anfangsbedingung für die dispersen Phase von den experimentellen Daten unabhängig zu machen, wurde ein stochastisches Breakupmodell, das Kolmogorov' s Model, für die Zerstäubung implementiert und konnte gute Ergebnisse erzielt werden.

Contents

1 **Introduction** 1
- 1.1 State of the art . . . 2
  - 1.1.1 Dispersion modeling . . . 3
  - 1.1.2 Evaporation of droplets . . . 6
  - 1.1.3 Spray atomization . . . 6
  - 1.1.4 Objectives and outlines of the work . . . 8

2 **Fundamentals of turbulent flows** 11
- 2.1 The scales of turbulent motion . . . 11
- 2.2 Numerical simulation and modeling approach . . . 13
  - 2.2.1 Direct numerical simulation (DNS) . . . 14
  - 2.2.2 Large eddy simulation (LES) . . . 14
  - 2.2.3 Reynolds averaged numerical simulation (RANS) method . . . 15
- 2.3 Modeling Reynolds stresses . . . 17
  - 2.3.1 First order turbulence modeling and k-ϵ two-equations modeling . . . 17
  - 2.3.2 Mathematical background and basic of the SAS model . . . 18

3 **Multiphase flow properties and description approaches** 25
- 3.1 Relevant parameter characterizing dispersed phase flows . . . 25
- 3.2 Main Multi-phase Flow Approaches . . . 26
  - 3.2.1 Eulerian Eulerian approach . . . 26
  - 3.2.2 PDF approach . . . 27
  - 3.2.3 Eulerian-Lagrangian approach . . . 28

4 **Eulerian-Lagrangian Approach** 29
- 4.1 Eulerian treatment of the continuous (carrier) phase . . . 29
- 4.2 Lagrangian treatment of the dispersed phase . . . 29
- 4.3 Interaction of phases and two way coupling . . . 30

5 **Two-phase system and microprocesses under investigation** 33
- 5.1 Atomization . . . 33
  - 5.1.1 Primary breakup . . . 33
  - 5.1.2 Secondary breakup . . . 34
    - 5.1.2.1 Kolmogorov's (1941) Theory of the Particle Breakup . . . 35
    - 5.1.2.2 Implementation into Computational Code . . . 37
    - 5.1.2.3 Critical radius, breakup frequency . . . 38
    - 5.1.2.4 Choice of parameters . . . 40
- 5.2 Turbulent Dispersion . . . 41
  - 5.2.1 Particle Langevin Model (PLM) . . . 41

5.2.2 Isotropic Random Walk Model (RWM-Iso) 43
5.2.3 Anisotropic Random Walk Model (RWM-Aniso) 44
5.3 Evaporation 44
5.3.1 Abramzon and Sirignano model: Uniform temperature model 45

6 Numerical procedure **51**
6.1 Solution procedure of the transport equations for the continuous phase 51
6.1.1 Finite volume method 52
6.1.2 Coordinate transformation 53
6.1.3 Discretization of the convective and diffusion terms 56
6.1.4 Time dependent discretization 57
6.1.5 Pressure velocity coupling 58
6.1.6 Boundary conditions 60
6.1.7 Inlet boundary conditions 60
6.1.8 Wall boundary conditions 61
6.1.9 Symmetry boundary conditions 65
6.1.10 Periodic boundary conditions 65
6.1.11 Solvers 65
6.2 Numerical method of the transport equations for the dispersed phase 68
6.2.1 Solving the equation of motion and time discretization 68
6.2.2 Statistical sampling 69
6.3 Euler-Lagrange coupling and underrelaxation of dispersed phase source terms . . . 70
6.3.1 Steady coupling 70
6.3.2 Unsteady coupling 71
6.3.3 Two-way coupling 71
6.3.4 Under-relaxation of source terms 73

7 Particle dispersion without droplet phase change **75**
7.1 Particle dispersion in a vertical channel flow 75
7.1.1 Experimental and numerical setup 75
7.1.2 Configuration 75
7.1.3 Results and discussions 76
7.1.4 Conclusion 77
7.2 Particle-laden shear flow 82
7.2.1 Configuration 82
7.2.2 Numerical setup 83
7.2.3 Results and discussions 83
7.2.4 Conclusion 91

8 Particle dispersion coupled to droplet phase change **93**
8.1 A simple test case for the validation of the evaporation model 93
8.2 Spray issuing into a co-flowing heated air stream 95
8.2.1 Configuration 95
8.2.2 Numerical setup 96
8.2.3 Results and discussions 97
8.2.4 Comparison of k-ϵ and SAS models 101
8.2.5 Conclusion 104

9 Particle dispersion coupled to breakup process **105**
9.1 Air-blast Configuration . . . 105
9.2 Results and Discussion . . . 105
9.2.1 Qualitative Results . . . 105
9.2.2 Quantitative Results . . . 107
9.3 Conclusion . . . 112

10 Summary and Outlook **113**

11 Zusammenfassung und Ausblick **115**

Nomenclature

Latin symbols

B_M	$-$	Spalting mass transfer number
B_T	$-$	Spalting heat transfer number
c	$J/(KgK)$	Specific heat capacity of the droplet
c_p	$J/(KgK)$	Specific heat capacity by constant pressure
C_W	$-$	Drag coefficient
C_W	$-$	Resistance coefficient
$C_{\epsilon,3}^{k-\epsilon}$	$-$	Constant model for the turbulence modulation of the $k-\epsilon$
$C_{\epsilon,3}^{RS}$	$-$	Constant model for the turbulence modulation of the RSM model
D	s^{-1}	Diffusion term within skalar transport equation
D_d	m	particle diameter
$\vec{F}$	N	Force
$\vec{g}/g_i$	m/s^2	Gravity acceleration vector/Cartesian components
h_v	J	Latent heat of vaporization
k	m^2s^{-2}	Turbulent kinetic energy
L	m	Characteristic length scale
Le	$-$	Lewis number
l_t	m	Turbulent length scale
$\dot{m}_{p,v}$	Kg/s	Droplet evaporation rate
N_p	$-$	number of real particles represented by one numerical parcel
Pr	$-$	Prandtl number
R	$J/(kg.K)$	Universal gas constant
Re	$-$	Reynolds number
Re_p	$-$	Particle Reynolds number
Sh	$-$	Sherwood number
St	$-$	Stokes number
$S_{\psi,p,s}$	$Variable\ \psi\ dependent$	Source term of the variable ψ for a non-evaporating droplet
$S_{\psi,p,v}$	$Variable\ \psi\ dependent$	Source term of the variable ψ due to evaporation
T	K	temperature
t	s	time
T_t	s	turbulent time scale
$\vec{u}/u_i$	m/s	Velocity vector/Cartesian components

V	m^3	Volume
$V_{i,j,k}$	m^3	Volume of the cell ijk
W_k	Kg/mol	Molecular weight
x_i	m	Cartesian coordinates
Z_L	$-$	Mass loading

Greek Symbols

Γ_ψ	$-$	heat
Π_{ij}	m^2/s^3	Pressure-strain correlation tensor (Cartesian components)
α_p	$-$	Volume fraction
β_J	$J/mole$	Activation energy of species k in reaction j
δ_{ij}	$-$	Cartesian components of unit tensor (Kronecker delta)
ϵ	m^2/s^3	heat
η_k	m	Kolmogorov length scale
μ/μ_t	$Kg/(m.s)$	Dynamic molecular/turbulent viscosity
ν/ν_t	$m^2/(s)$	kinematic molecular/turbulent viscosity
ρ	kg/m^3	density
τ_p	s	Particle relaxation time
ψ_ψ	$-$	General scalar quantity

Operators

$\overline{(\bullet)}$	Reynolds averaging
$\sum$	Sum
Δ	Difference
$\vec{(\bullet)}$	Vector
∞	Infinity
$(-)_p$	Particle/droplet

Abbreviations

ASM	Algebraic Reynolds Stress Model
$RANS$	Reynolds Averaging based numerical Simulation
CDS	Central Difference Scheme
CFD	Computational Fluid Dynamics
CV	Control Volume
DNS	Direct Numerical Simulation
$E-E$	Eulerian-Eulerian
$E-L$	Eulerian-Lagrangian
LDA	Laser Doppler Anemometry
LES	Large Eddy Simulation

PDA	Phase Doppler Anemometry
RMS	Root Mean Square
RSM	Reynolds Stress Model
SAS	Scale Adaptive Simulation
UDS	Upwind Difference Scheme
$URANS$	Unsteady RANS
UTM	Uniform Temperature Model

1 Introduction

More than 80 % of all the energy conversion is produced by combustion (Coal, Gas, Oil) [123]. The trend of energy demand is expected to grow by 50 % by the year 2030. The nonrenewable nature of fossil fuels, the co-production of greenhouse gas, particulate, and heavy metal emissions during combustion are the representative bottle necks of energy conversion by combustion. Towards a more sustainable approach to energy development, the renewable energy sector (water, solar and wind) characterized by their environmental cleanliness and virtual inexhaustibility remains up today limited for large-scale power generation and restricted by relative costliness to build and maintain. In spite of its known disadvantages combustion is still the cheapest and the most direct way to convert energy. It is therefore important to look for improvements of combustion processes and to promote the efficiency of the energy conversion in combustion systems.

Combustion systems are often constituted by various components flowed by the liquid, gaseous or solid fuel. Through these components, the fuel experiences specific thermodynamic behavior change that may be relatively complex and undergoes elementary transformations or processes that can interact each other and whose analysis can be delicate. The processes that accompany the movement of the fuel through engineered systems are of particular interest once understanding of the flow properties has to be gained or prediction, optimization and design tasks have to be carried out.

Several important combustion systems involve particles or liquid droplets flowing within a turbulent flow resulting in multiphase flow systems. This is the case of IC engines or aircraft combustion chambers in which the liquid fuel used undergoes breakup, atomization, dispersion, evaporation and subsequent combustion. Other systems use solid particles or bubbles under reacting or isothermal conditions (e.g. firing of wastes, coals; fluidized bed combustion; Cryogenic engine, chemical looping etc.). The overall common feature is the multi-scale and multi-physical character of the systems whereby various physical and chemical processes may occur and interact. In particular, the multiphase flows involve movements of many individual particles and their interaction with the carrier flow turbulence, mass transfer between fluid and particulate phase, heat transfer between the phases and their surrounding phase and interaction between the individual particles themselves. It is even more complicated when the particles/droplets change their physical state and experience combustion after appropriate mixture formation at both micro- and meso-scale levels.

Especially for spray combustion, an accurate determination of droplet and vapor spatial distribution, and a reliable control of the interaction between the spray with the surrounding turbulent gas flow are very important. The droplet characteristics influence the spray vaporization, which in turn influences the combustion performance [2]. In a feedback effect the rate of combustion affects the rate of vaporization. Droplet trajectories that are influenced by various forces acting on droplets, strongly affect the droplet distribution primarily determined by the breakup process. So, the droplet trajectories affect the local vaporization rate along with the droplet characteristics and the whole spray vaporization in a complex interacting manner.

In order to provide reliable design criteria and to handle with complex flow systems, early detailed information of different design variants and parametric studies is necessary [8]-[10], [13], [45]. For systems that are extremely costly to build and to test, only CFD based analysis is capable of delivering deeper insight into transport processes of interest [8]-[10], [13], [45].

The numerical simulation of turbulent two-phase flows has been quite improved during the past decades. Direct numerical simulation (DNS) is the most physical since it requires a minimum of closure models. Due to the computational cost this method is restricted to a very low number of particles (5000 particles) at low to moderate Reynolds (Re) numbers. Therefore this method is not of interest in industrial and engineering applications [1], [44]. For complex turbulent flows of practical importance, RANS and LES have merged as realistic alternatives. LES is expected to be more reliable, where the flow is governed by large turbulent structures. Experiences show that LES is mostly not able to deal with the near wall effects properly. For this reason very fine grids are needed with correspondingly increasing of computational costs [1], [44]. This may disqualify LES nowadays for design and optimization needs in many industrial environments.

For statistically steady engineering flow applications, using RANS methods for the carrier phase coupled with particle Lagrangian tracking has shown acceptable compromise between simplicity and accuracy. RANS based investigations have been conducted to simulate various configurations, especially the transport and deposition of nano- and micro-particles in channel and pipe flows [4]-[7] and in more complex geometries such as human extrathoracic and lung airways [8]-[10] delivering acceptable prediction trends.

As most multiphase flows feature unsteady behavior, unsteady RANS (URANS) based predictions is used as practical platform for the most engineering purposes. Appropriate techniques need to be suggested or improved. This is the main motivation of this work.

Due to the multifaceted character of turbulent multiphase flows, many researchers have focused their work on specific aspects, like turbulent dispersion, modulation, evaporation, etc. In this work, interest is put on dispersion driven interaction processes. To consider all the above mentioned specific aspects in an interacting manner requires the integration of well tested submodels needed into a numerical tool using a suitable consideration of boundary components and involved interactions. Together with a subsequent validation of the tool, this task is the main objective of this work.

Concentrating on numerical simulations of turbulent disperse multiphase flows, three numerical modeling approaches are generally applied. These are the Eulerian-Lagrangian, the Eulerian-Eulerian and the probability density function (PDF) methods. In both, the need to better account for the effect of turbulent transport of droplets/particles on evolving spray/particles properties is evident [1], [36], [37], [44]. In the following focus is on the Eulerian-Lagrangian approach adopted in this work. This description has the main advantage that micro-processes and their interactions can be well followed and particle size distributions can additionally be taken into account without any special effort.

1.1 State of the art

As pointed out above, interest is put on liquid fired combustion systems, in which the liquid is first atomized than undergoes phase transition, transport and mixing and at the end combustion.

The present work focuses on modeling of dispersion driven microprocesses in dispersed phase including droplet breakup and phase change within a flowing turbulent carrier phase.

1.1.1 Dispersion modeling

In turbulent spray flows, the droplets do not follow the mean trajectories of the carrier phase. They disperse quickly due to interactions with the turbulent velocity fluctuations. In recent years this process has been studied by many researchers who proposed various dispersion models aiming first at including for finite inertia particles the following effects [36], [37], [44], [1].

- The inertia effect to predict that the dispersion of (solid) particles might exceed the dispersion of the fluid particles in the absence of body force.
- The crossing trajectories effect to predict that in the presence of a drift velocity, a finite inertia particle will disperse less than a fluid particle.
- The continuity effect where the dispersion in the direction of the drift velocity exceeds the dispersion in the other two directions.

It has been indicated by several authors [8], [4], [5] that using inappropriate dispersion and turbulence models could yield to completely nonphysical results of flow and disperse properties.

Thereby the instantaneous fluid velocity which is known to influence the particle trajectories, is especially of interest when evaporation takes place and when temperature and chemical composition of the particles depend on their history [22]. In order to quantify the instantaneous fluid velocity seen by the particle, as it appears in the droplet motion equation, and its effect on the droplet distribution one models the Root Mean Square (RMS) values of the fluid parcel velocity at the particle location via dispersion models.

As mentioned before various models have been proposed in the literature. Yuu et al. [113] applied a stochastic dispersion model, which includes empirical correlations of mean and turbulent properties. Gosman and Ioannides [112] improved the Yuu et al. [113] model by suggesting a more comprehensive approach that allows for a relative mean velocity between the eddy and the particle along with a first consideration of the crossing trajectories. This approach that assumes that particles interact with a sequence of turbulent eddies can lead to inconsistent behavior for very low particle inertia. This kind of models are called eddy "life time model", where each fluid velocity fluctuation is kept constant on a time step which is equal to the Lagrangian integral time scale (see in [71], [20]).
Because of its simplicity and robustness, the Gosman and Ioannides dispersion model [112] remains the primary schema for describing particle dispersion in most commercial CFD codes.
Despite recent extensions in [71] or [105] this model does not account for spatial and time correlation of the flow fluctuation along the particle trajectory. Coimbra et al. [46] reproduced the mean and the rms of the fluid velocities in the two-dimensional mixing layer of Hishida et al. [47] well with an eddy life-time model. However, the prediction of the particles velocity fluctuations failed and showed that the eddy-life time approach is insufficient in anisotropic turbulent flows.

To overcome this problem advanced models have been suggested. The most accurate models are based on the Langevin equation [15], [19]. To capture more physics Minier [21] suggested a Langevin equation model for the instantaneous fluid velocity working on particles. He extended the "Simplified Langevin Model“ presented by Pope [11], [12] for the instantaneous fluid velocities in Lagrangian approach following a fluid particle (see in [15], [19]) to inertial particles by

Table 1.1: Main dispersion models used in technical applications

Dispersion model	Advantages	Weakness
Eddy life time (ELM) Gosman & Ioannides (1981) [112]	simplicity and robustness.	constant fluctuation during a time step.
RWM Hall [122], Legg et al. [50], Kohnen [18]	more physical than ELM and less than PLM.	only isotropic homogeneous turbulence.
RWM-Aniso Legg and Raupach (1982) [50], Merci et al.(2011) [22], Chrigui et al. [34], Kohnen [18]	extension of RWM to anisotropic homogeneous turbulence cases.	do not include all the physic of Langevin.
PLM Peirano et al.(2005) [15], Minier et al. [48], Horender et al. [13], Apte et al. [37], Fede et al. [44], Carlier et al. [40]	Integration of most physic in Langevin equation.	expensive to implement.

adding a drift term that takes into account the drift between the inertial particles and the fluid one. This model is called PLM (Particle Langevin Model) throughout the paper. This model found applications in various contributions either in RANS, LES or in PDF framework as reported in [15], [48], [13], [37], [44], [40] among others.

Horender et al. (2005)[13] used the PLM in their investigations as dispersion model and showed that the vortex-structure generated in a particle-laden mixing layer could be captured better than using the Random Walk Model (RWM). The RWM [18] can also be seen as a Langevin model for an Ornstein-Uhlenbeck process, which represents properties of the model in a very special case (isotropic homogeneous turbulence) and manifests therefore only a part of the physics contained in the Particle Langevin Model. An improvement of the RWM, by adding a drift term, which should avoid the drift of the particles from areas with high turbulence has been accomplished and used amongst others in [22]. Table 1.1 summarizes the main dispersion models mostly used in technical applications and outlines their advantages and weakness. Table 1.2 provides some contributions focused on dispersion modeling. It appears from this table 1.2 that many studies

1. investigated the effect of dispersion models mostly in statistically steady flows based on steady coupling between E-L solvers and steady RANS with and without evaporation.
2. applied RWM or RWM-Aniso with or without evaporation
3. applied PLM without evaporation
4. did not account for phase change coupled to full Lagrangian equation. (Note that, when droplets evaporate, the Stokes number changes that leads to the change of droplet relaxation time.)
5. did not include the breakup effect on droplet distribution (the breakup process together with the dispersion determines the droplet trajectory along with the evaporation and subsequently fuel-air mixture preparation and the combustion.)

In this work, it is intended to fill the gap by including the issues 3, 4 and 5 into an E-L method coupled to a full Langevin dispersion model while applying URANS.

Table 1.2: Some of contributions focused on dispersion modeling using E-L method within RANS

Contributer (Author)	**configuration**	**features** (model)	**Coupling**
Eddy life time (ELM) Model Yuu et al. [113] Gosman & Ioannides (1981) [112]	turbulent round jet, dust laden round jet.	easy to implement, no time and spatial correlation of the flow fluctuation along the particle trajectory, no Anisotropy, no crossing trajectories effect no inhomogeneity effect no correlation between the fluid fluctuations.	steady
Eddy life time (ELM) Hishida et al. (1992) [47], Maneshkarimi [61]	two-dimensional mixing layer, evaporating spray.	no time and spatial correlation of the flow fluctuation along the particle trajectory, no Anisotropy, no correlation between the fluid fluctuations.	steady
RWM Hall [122], Legg et al. [50], Kohn et al.[18]	turbulent two phase flow, two phase flow mixing layer.	higher performance of RWM compared to the ELM.	steady
RWM-Aniso Legg and Raupach (1982) [50], Merci et al.(2011) [22], Chregui et al. [34], Kohnen [18]	turbulent two phase flow, channel flow, two phase mixing layer, evaporating spray.	extension of RWM to anisotropic homogeneous turbulence cases.	steady
Particle Langevin Model (PLM) Peirano et al.(2005) [15], Minier et al. [48], Minier (1999) [14], Horender (2005) [13], Carlier et al. [40]	wall jet, recirculating bluff-body flow particle-laden mixing layer, vertical channel flow.	two phase flow (solid particles) in Lagrangian approach, added a drift term to the Langevin equation, good capture of the vortex-structure compared to RWM.	steady and unsteady

1.1.2 Evaporation of droplets

The phase transition (vaporization) is a complex process which has a strong contribution to the phase interaction. Different models have been developed to estimate the rates of heat transfer to droplets and evaporation process in a turbulent ambient. They are generally designed to describe two main processes in and around the droplets:

1. The droplet models describe the mass and heat transfer phenomena inside the droplet.
2. The phase models are formulated to describe the mass and heat transfer processes between the gas phase surrounding the droplet and the droplet itself.

The infinite heat conductivity model by Ranz & Marshall (1952), the so-called 'D^2 Law' classical evaporation model by Godsave (1953) and by Spalding (1953) [107] can be representatives of the first category of evaporation models, where the surface of the droplets reduce linear with the time.

Regarding the second category, the non-equilibrium model by Bellan &Summerfield (1978) [108] and equilibrium model by Sirignano & Abramzon (1989) are mostly used in investigations of reacting and non-reacting spray flows. Recent reviews can be found in [125] and [91]. In this work it is assumed that:

1. One component model is considered, so that one solely deals with the so-called infinite conductivity model.
2. Droplets are assumed to be spherical.
3. Secondary atomization and coalescence of droplets are neglected as one concentrates on the dilute spray region. In other words simple elastic collisions between droplets and wall are assumed without any kind of film formation [12].
4. We neglect the influence of the surface tension and assume a uniform pressure around the droplet.
5. Uniform physical properties of the surrounding fluid and liquid-vapor thermal equilibrium on the droplet surface.
6. The ambient air is not soluble in the droplet fluid.
7. Chemical reactions and radiation are not considered.

We restrict ourselves to the model by Abramzon and Sirignano [109] who revised the infinite conductivity model to incorporate the effects of Stefan flow on heat and mass transfer. In this model, heat transfer is modified through the use of modified forms for the Nusselt and Sherwood numbers.

1.1.3 Spray atomization

The transformation of a liquid jet into droplet sprays can be divided into two separate steps as showed in figure 1.1.

The process of the jet breakup is described by Lefebvre [124] as follows: "When a liquid jet emerges from a nozzle as a continuous body of cylindrical form, the competition set up on the surface of the jet between the cohesive and disruptive forces gives rise to oscillations and perturbations. Under favorable conditions the oscillations are amplified and the liquid body disintegrates

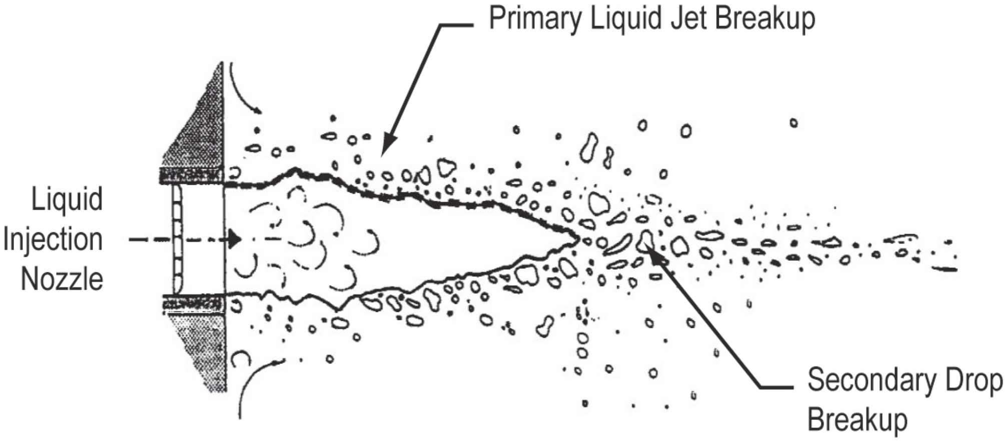

Figure 1.1: Sketch of primary and secondary liquid jet breakup regimes [143].

into drops." This process is sometimes called primary atomization or primary liquid jet breakup. Moving downstream, the liquid further breaks up into smaller drops. This process is known as secondary atomization (secondary droplet breakup).

The injection and atomization of a spray are not well understood even though they are the processes which dominate the entire spray characteristics. Most of the modeling studies in two phase flows start with atomized spray. Thereby the initial droplet distributions are taken from experimental data to define the inlet conditions for the simulation. This is due to the fact that the atomization that occurs in dense spray region is difficult to access both with experimental and numerical models. Laser-optical methods cannot indicate the dense spray properly and thus, characterization of this regime is not easy. Several experimental studies [114] - [53] have demonstrated the difficulty in clearly defining a dominant air-blast atomization mechanism, which is of interest in this work. Each spray region produces droplets with a large spectrum of size, which is often independent of the breakup pre-existing properties.
To integrate the atomization in a numerical calculation requires a model of droplets production. Different models exist that describe both primary and secondary breakup. A recent review is provided by Trinh (2007) [143] and Gorokhovski(2001) [104].

The breakup model of Reitz [111] (wave breakup model) is the most widely used model of droplets production. This breakup model results by assuming a hydrodynamic instability caused by surface tension. The newly formed droplets are characterized by a single Rayleigh mode of atomization. At the same time a Rayleigh's type of breakup takes place when the liquid jet is injected into quiescent environment at a relatively low velocity.

When the liquid jet is injected into the flowing motion of gas at high relative velocity (large Weber number), the influence of interfacial forces becomes less important and the mechanism of breakup becomes more complex. Most of the turbulent eddies may impact on the liquid jet which cause the breakup. This kind of breakup is referred to as the air-blast atomization Liu et al. [114] - [53]. Kolmogorov [55] wrote a stochastic theory for the breakup of solid particles which describes the cascade of uncorrelated breakage events. His theory describes the breakup of solid particles as a random discrete process where the probability of breaking each parent particle into a given number of parts is independent of the size of the parent particle. It is interesting to apply the Kolmogorov's scenario to the breakup of a liquid drop at the large Weber number, in the range from its initial size down to the size of stable droplets once secondary breakup has to be correctly coupled to turbulence. This will be done in this work in order to evaluate the impact of the liquid atomization on the droplet dispersion process. It should be noted that the cascade idea was involved earlier in the statistical description of breakup by Novikov et al. [57] where Novikov's [56] multiplicative intermittency theory was implemented to obtain the stationary droplet size distribution.

1.1.4 Objectives and outlines of the work

As pointed out above, experience shows that LES has mostly difficulty to deal properly with flow behavior near the wall. For configurations in which near wall effects are important as it is the case in wall-bounded multiphase flows, LES will remain too expensive for design and optimization tasks in various industrial applications notwithstanding the remarkable progress of hardware technologies. In this work it is therefore intended to improve the prediction capability of URANS-based models for wall-bounded multiphase flow configurations featuring complex micro-processes affected by turbulent dispersion.

As it emerges from Table 1.2 the coupling between phases including the effect of turbulent dispersion on phase change phenomena and break up process may potentially improve the droplet distribution prediction once appropriate dispersion models are integrated and an unsteady coupling is numerically achieved between involved phases of statically unsteady multiphase flows. For this purpose, the study includes the physical phenomena of

- secondary breakup along with droplet-droplet interactions
- phase change process, especially the droplet evaporation
- full two-way coupling between phases;

all being integrated into an unsteady numerical mode within the URANS context to reliably retrieve the unsteadiness of turbulent two-phase flows.

Chapter 2 first describes the physical basics of turbulent carrier phase flow without combustion. Thereby governing transport equations are outlined along with the turbulence models used. Chapter 3 provides an overview of the essential parameters required for describing the dispersed phase and reviews the main mathematical approaches for numerically studying turbulent two-phase flows. Chapter 4 sets the theoretical basis for the modeling approach relying on the Eulerian-Lagrangian procedure used in this study. Chapter 5 focuses especially on the modeling of specific processes, such as secondary breakup, turbulent dispersion and spray evaporation process. Chapter 6 introduces the numerical procedure applied. Two solvers are used for the description of both the gas phase and the dispersed phase. In particular, the numerical coupling between the two solvers, namely the Eulerian and the Lagrangian solver, is shortly highlighted. While the models setup needs verifications, five different configurations are used for model validation purposes. The ability of the models to capture the essential multiphase properties is especially evaluated and discussed. The first and second configurations deal with comparison of different dispersion models where the dispersed phase is composed by solid particles without any consideration of phase change or particle heating. The third and fourth configurations include phase change phenomena. In particular, the spray evaporation and the impact of dispersion modeling on the distribution and concentration of evaporating droplets are analyzed. The last configuration features an air-blast atomization of interest in modern gas turbine combustors. By forming droplets, a large surface area is produced, that enables to reduce the liquid vaporization time, which results in a better mixing and an increase in the time available for complete combustion [2], [16], [22], [33]. Since experience shows that atomization results depend on the atomizer design and are difficult to be compared to each other, there is a need for directly predicting the outcome of the atomization process. This may dispense with the need to perform empirical studies for each individual atomizer geometry and will help initialize safety the droplet numerical tracking calculations. The main idea behind this task is to ascertain the predictability of a stochastic model together with its impact on the turbulent droplet dispersion. This manuscript is closed by chapter 8 that summarizes the main findings of this study and suggests possible directions for future research

2 Fundamentals of turbulent flows

2.1 The scales of turbulent motion

Turbulent flows are characterized by different flow structure sizes. The large but not the largest eddies contain major part of the turbulent kinetic energy. Due to this fact the large eddies are often called as energy containing eddies. The length and time scales of these eddies are of interest. In particular the size of the energy containing eddies depends on the geometry of a spatial domain as well as the local intensity of turbulence. This size can be related to the integral turbulent length scale that can be determined from the two-point spatial correlation function or coefficient for statistically steady (time independent) turbulence

$$R_{ij}^{L}(x, x+\Delta x) = \frac{\overline{\acute{u}_i(x)\acute{u}_j(x+\Delta x)}}{\sqrt{\overline{\acute{u}_i^{2}(x)}}\sqrt{\overline{\acute{u}_i^{2}(x+\Delta x)}}} \tag{2.1}$$

$$L_{ij} = \frac{1}{2}\int_{-\infty}^{+\infty} R_{ij}^{L}(x, x+\Delta x)d(\Delta x) \tag{2.2}$$

Here L_{ij} is the length scale tensor. For homogeneous isotropic turbulence the integral length scale, which is independent of the direction, is given by

$$l_t = \frac{1}{3}L_{ii} \tag{2.3}$$

The two-point velocity correlation function for homogeneous isotropic turbulence and the corresponding integral turbulent length scale are schematically shown in Figure 2.1.

The corresponding time scale can be determined from the known time correlation function

$$R_{ij}^{T}(x, t+\Delta t) = \frac{\overline{\acute{u}_i(t)\acute{u}_j(t+\Delta t)}}{\sqrt{\overline{\acute{u}_i^{2}(t)}}\sqrt{\overline{\acute{u}_i^{2}(t+\Delta t)}}} \tag{2.4}$$

$$T_{ij} = \frac{1}{2}\int_{-\infty}^{+\infty} R_{ij}^{T}(x, t, t+\Delta t)d(\Delta t) \tag{2.5}$$

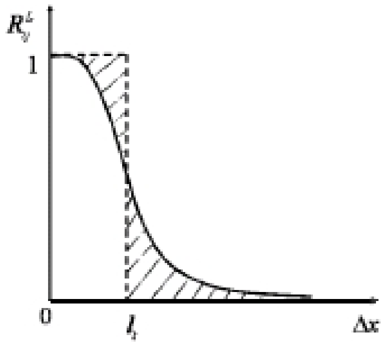

Figure 2.1: Two-point velocity correlation function versus the distance between two point Δx for homogeneous isotropic turbulence

Assuming isotropy and homogeneity leads to

$$T_{ij} = \frac{1}{3} T_{ii} \tag{2.6}$$

The turbulence integral length and time scales can be defined in terms of k (turbulent kinetic energy) and ϵ (energy dissipation rate) as

$$l_t = k^{3/2}/\epsilon \tag{2.7}$$

$$\tau_t = k/\epsilon \tag{2.8}$$

The integral turbulent time scale can be interpreted qualitatively as an averaged inverse rotational frequency of the typical big eddy appearing in the spatial location x.

Though the character of turbulence in practical flows is neither isotropic nor homogeneous, the idealized integral length scale provides at least coarse quantitative information about spatial correlation and sizes of typical energy containing eddies in turbulent flows. The integral turbulent length scale can be qualitatively interpreted as an averaged radius of the typical big eddy appearing in the spatial location x.

The turbulent kinetic energy spectrum which is obtained from the Fourier transformation of the spatial isotropic two-point correlation function R_{ij}^T is schematically plotted in Figure 2.2. $E_\omega(k_\omega)$ is the kinetic energy density per wave number k_ω or the inverse turbulent length scale. The maximal values of $E_\omega(k_\omega)$ correspond to the energy containing scales that are related to the turbulent length scale l_t. Eddies of size smaller than the energy containing eddies build the inertial subrange. Kolmogorov showed that the transfer of energy from large to small scales within the inertial subrange is independent on the scale size and follow the profile ${k_\omega}^{-5/3}$. At the right side of the inertial subrange the wave number corresponding to the Kolmogorov scale η_k is located.

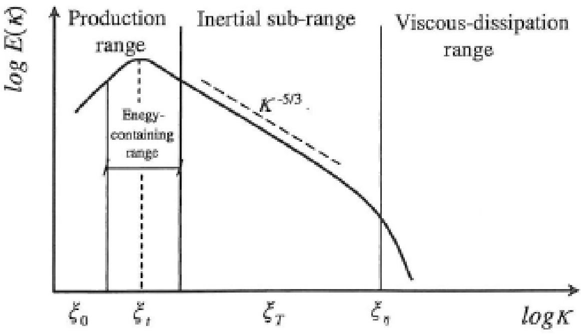

Figure 2.2: Schematic representation of the turbulent kinetic energy spectrum as a function of the wavenumber κ for isotropic homogeneous turbulence. (ξ_0, ξ_l, ξ_T and ξ_η correspond to the very large length scales, the integral length scale, the Taylor length scale and Kolmogorov length scale, respectively.) [61]

Note that the rate at which the turbulent kinetic energy is transferred from bigger eddies to smaller eddies is called the dissipation rate ϵ. The smaller an eddy, the greater the velocity gradient inside the eddy and the greater the viscous stress that counteracts the eddying motion. The cascade of energy cannot be extended infinitely because of the viscous forces. Consequently, there is a statistical lower limit of the smallest eddy size that corresponds to a minimum scale of turbulence and a maximum frequency in the turbulent motion. In this stage the kinetic energy of the fluctuating motion will dissipate completely into the internal energy of the flow. The length scale for the smallest eddies is called as Kolmogorov scale and is related to the dissipation rate by:

$$\eta_k = \nu^{3/4}/\epsilon^{1/4} \tag{2.9}$$

Through the fluid viscosity ν a corresponding Kolmogorov time scale is given as

$$\tau_k = \nu^{1/2}/\epsilon^{1/2} \tag{2.10}$$

In order to gain information of turbulent flow properties, different approaches including experimental measurements and numerical modeling are often used. In this work focus is on the numerical modeling and simulation techniques.

2.2 Numerical simulation and modeling approach

Because most industrial and engineering flows are turbulent, let us outline the main numerical and modeling approaches applied to study these flows, namely DNS, LES and RANS.

2.2.1 Direct numerical simulation (DNS)

The Navier-Stokes equations that describe the motion of any Newtonian fluid can be numerically solved by means of the DNS (direct numerical simulation) approach without any turbulence model. Thereby the whole range of spatial and temporal scales of the turbulence must be resolved.

By doing this the computational cost of DNS becomes very high, especially for the high Reynolds numbers flows in most industrial applications. Nevertheless, direct numerical simulation is often used in fundamental research in turbulence for low and moderate Reynolds number flows. Thereby DNS allows a wide understanding of the physics of turbulence. Therefore, using DNS make it possible to perform variable "numerical experiments", since one can extract from DNS data information which are difficult or impossible to obtain in measurement experiments. Thus, direct numerical simulations are useful in the development of turbulence models for practical applications, such as sub-grid scale models for Large eddy simulation (LES) and turbulence models for methods that solve the Reynolds-averaged Navier-Stokes equations (RANS). This is accomplished by means of "a priori" tests, in which the input data for the model is taken from a DNS simulation, or by "a posteriori" tests, in which the results produced by the model are compared with those obtained by DNS.

2.2.2 Large eddy simulation (LES)

Large eddy simulation consists in a direct computing of large eddies and modeling of small (quasi-universal) eddies so-called subgrid scales (SGS). In this method, not the whole turbulent spectrum has to be resolved. It uses a filtering operation that allows for removing in a proper way the small scales. This operation introduces new unknown terms representing the small-scale information lost by the filtering. Thus, some models for the small scales called as SGS-models are needed in order to close the system of filtered equations. From the modeling point of view this approach simply displaces the problem into the less important part of the energy spectrum. As a subgrid parameterization is still necessary, its influence is expected to be rather small, at least when the most important scales are all resolved on the computational grid.

Because in LES small eddies are modeled, computational grid will be therefore much bigger than the Kolmogorov length scale, and time steps can be chosen much bigger than in DNS. So the computing resources for LES are much lower than DNS. The area of applications of LES has considerably increased with rapid development of computer facilities. However, some problems are inborn to LES. For example, the problem of wall flows is still not satisfactory solved. It is apparent that near the wall all vortices are small so that both space and time steps needed for LES drop down to values which is characteristic for DNS. Existing solutions such as anisotropic models and dynamic procedures, still not give satisfactory results.

For numerical combustion investigations, some optimism has appeared among researchers, who believe to overcome the problems of turbulence modeling by means of LES [130]. However, in addition to difficulties in handling the flow in the vicinity of solid boundaries, LES still requires turbulent combustion models for the SGS part. The development of these models for LES and their application to various reacting flows appears to be the most popular area of modern combustion research, but most models are still based on RANS type concepts. One of the solution for the wall problem for LES appears to be a combination of LES and the Reynolds averaging numerical simulation (here RANS) in the line of the so-called hybrid RANS/LES models. The latter method will be addressed later on.

2.2.3 Reynolds averaged numerical simulation (RANS) method

Previously known as Reynolds averaged Navier-Stokes method, today the Reynolds averaging procedure is extended to quantities in all scalar (passive or reactive) transport equations. The RANS method was thought of most prevalently used statistical solution approach for scientific and engineering calculations and was mostly developed during the last decades. Its economical computational cost and its good performance near walls makes it the basis of numerical investigation in the present study.

In the RANS approach the turbulent flow is modeled over the whole range of small and large scales, and governing equations are solved for mean field quantities. In this Reynolds averaging concept, each instantaneous variable ϕ of the turbulent flow field is therefore considered to be the sum of a mean value $\overline{\phi}$ and its fluctuation $\acute{\phi}$,

$$\phi(x_i, t) = \overline{\phi}(x_i, t) + \acute{\phi}(x_i, t), \tag{2.11}$$

The mean value $\overline{\phi}$ can be obtained from a statistical averaging. It may be, for instance, an ensemble averaging that is taken over a sufficiently large number N of experiments having the same initial and boundary conditions,

$$\overline{\phi}(x_i, t) = \frac{1}{N} \sum_{n=1}^{N} \phi_n(x_i, t). \tag{2.12}$$

Alternatively, simple time-averaging can be used to provide statistical average values. For time depending mean variable in a period ∂t with $t_2 = t_1 + \partial t$, the time-averaged variable is defined as

$$\overline{\phi}(x_i, t) = \frac{1}{\partial t} \sum_{t}^{t+\partial t} \phi(x_i, \acute{t}) d\acute{t}, \tag{2.13}$$

and the mean of fluctuating part is then set to zero,

$$\overline{\acute{\phi}} = 0. \tag{2.14}$$

In Fig. 2.3 the decomposition of a general variable ϕ as a function of time is shown for a stationary and unsteady flow, respectively.

In this time-averaging concept, a separation of the fluctuating time scales of variables, T_1, and the main time scale of the 'slow' variation of mean flow, T_2, is assumed. This means that the time

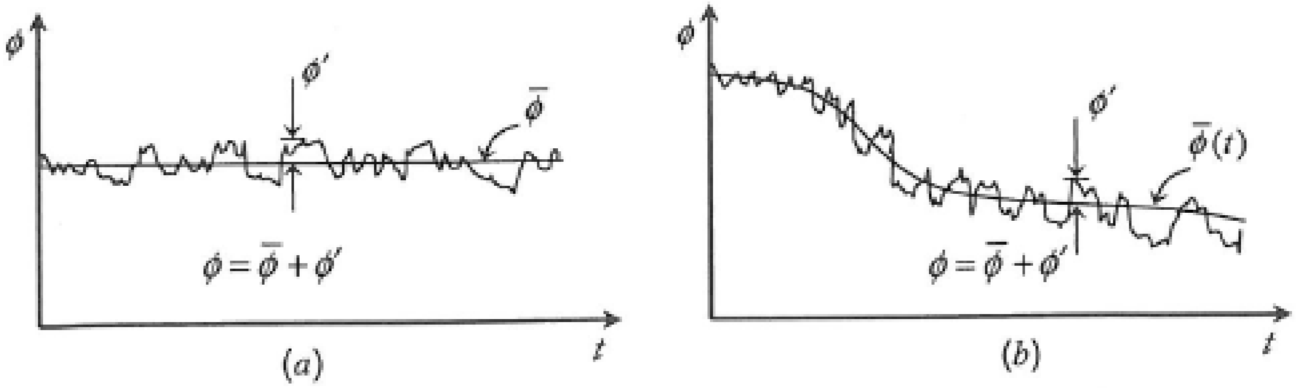

Figure 2.3: Time average for any variable ϕ: a) stationary case, b) unsteady case.

scales T_1 and T_2 exist and differ by several orders of magnitude, $T_1 << T_2$, otherwise the mean and fluctuating components would be correlated.

Applying the Reynolds averaging 2.12 to equations of mass, momentum and scalar [150] yields to

$$\frac{\partial\rho}{\partial t} + \frac{\partial\rho\overline{u_i}}{\partial x_i} = \overline{S}_{1,p,v}, \tag{2.15}$$

$$\frac{\rho\partial\overline{u_i}}{\partial t} + \frac{\rho\partial\overline{u_j u_i}}{\partial x_j} = \rho g_i - \frac{\partial\overline{P}}{\partial x_i} + \frac{\partial}{\partial x_j}\left(\mu\frac{\partial\overline{u_i}}{\partial x_j} - \rho\overline{\grave{u}_i\grave{u}_j}\right) + \overline{S}_{u_i,p,s} + \overline{S}_{u_i,p,v}, \tag{2.16}$$

$$\frac{\rho\partial\overline{Y}}{\partial t} + \frac{\rho\partial\overline{u_j}\overline{Y}}{\partial x_j} = \frac{\partial}{\partial x_j}\left(\rho\Gamma\frac{\partial\overline{Y}}{\partial x_j} - \rho\overline{\grave{u}_i\grave{Y}}\right) + \overline{S}_{Y,p,s} + \overline{S}_{Y,p,v}, \tag{2.17}$$

$$\frac{\rho\partial\overline{T}}{\partial t} + \frac{\rho\partial\overline{u_j}\overline{T}}{\partial x_j} = \frac{\partial}{\partial x_j}\left(\rho\Gamma\frac{\partial\overline{T}}{\partial x_j} - \rho\overline{\grave{u}_i\grave{T}}\right) + \overline{S}_{T,p,s} + \overline{S}_{T,p,v}, \tag{2.18}$$

The equation of mass conservation 2.15 states that the mass of an isolated system remains usually constant independently of all process where this system is involved in.

Equation 2.16 is the Navier Stokes transport equation for a Newtonian fluid, which states that the amount of momentum remains constant within a considered control volume. Momentum is neither created nor destroyed, but only changed through the action of forces as described by Newton's law of motion.

Equation 2.18 is the temperature equation and the equation 2.17 is the equation for the vapor concentration.

In case of large Reynolds number, the molecular viscosity and diffusion coefficient are very small, therefore they can be neglected. In the equations 2.15-2.18 some new terms arise, namely the unclosed Reynolds stress tensor $\overline{\acute{u}_i\acute{u}_j}$ the turbulent transport terms $\overline{\acute{u}_j\acute{Y}}$ and $\overline{\acute{u}_j\acute{T}}$ which have to be modeled. The last type of unclosed quantities, in the right hand side represent the particles/droplets source terms which in turn will be explained in details later.

Although the main advantages of RANS are the relatively low computational costs involved and the wide range of applicability compared to DNS or LES, from an accuracy point of view RANS modeling lies below DNS and LES and the effort required to model the whole energy spectrum including large and small scale structures is higher [128].

2.3 Modeling Reynolds stresses

Focused on the mean flow description2.15 - 2.18 turbulence modeling aims at representing the unclosed terms as realistically as possible. In the following first order turbulence models, as they are used within this work, will be introduced.

2.3.1 First order turbulence modeling and k-ϵ two-equations modeling

For the description of the unknown Reynolds stresses Boussinesq proposed the first assumption (isotropic turbulence) [79] by introducing the correlation 2.19, which gave rise to the first order turbulence modeling.

$$-\overline{u_i'u_j'} = \nu_t \left(\frac{\partial \bar{u}_i}{\partial x_j} + \frac{\partial \bar{u}_j}{\partial x_i} \right) - \frac{2}{3} k \delta_{ij}, \tag{2.19}$$

$k = 1/2\overline{u_i'u_i'}$ the turbulent kinetic energy and ν_t represents the eddy viscosity. The Reynolds stress tensor modeled by means of such velocity gradients-ansatz, can be legitimated for applications with a flow dominant direction like turbulent channel or shear flow.

Representing the turbulent length and time scales, respectively k and ϵ quantities have been used to represent mathematically the eddy viscosity ν_t. In 1974 Launder and Spalding introduced the famous standard $k - \epsilon$ two equation turbulence model [133], where the turbulent eddy viscosity ν_t is related to k and ϵ , through the following semi-empirical expression:

$$\nu_t = C_\mu \frac{k^2}{\epsilon}, \tag{2.20}$$

where C_μ (see Table 2.1) is a model constant and k and ϵ are determined by their respective coordinate-invariant modeled transport equations.

$$\frac{\partial k}{\partial t} + \frac{\partial}{\partial x_i}(\bar{u}_i k) = -\frac{\partial}{\partial x_i} \left(\frac{\nu_t}{\sigma_k} \frac{\partial k}{\partial x_i} \right) - \overline{u_i'u_j'} \frac{\partial \bar{u}_j}{\partial x_j} - \epsilon \tag{2.21}$$

Table 2.1: model coefficients for the standard $k - \epsilon$ model

C_μ	σ_k	σ_ϵ	$C_{\epsilon 1}$	$C_{\epsilon 2}$
0.09	1.0	1.3	1.44	1.92

$$\frac{\partial \epsilon}{\partial t} + \frac{\partial}{\partial x_i}(\bar{u}_i \epsilon) = -\frac{\partial}{\partial x_i}\left(\frac{\nu_t}{\sigma_\epsilon}\frac{\partial \epsilon}{\partial x_i}\right) - C_{\epsilon 1}\frac{\epsilon}{k}\overline{u_i' u_j'}\frac{\partial \bar{u}_j}{\partial x_j} - -C_{\epsilon 2}\frac{\epsilon^2}{k} \tag{2.22}$$

Using the eddy viscosity approach, one can model the production term (second term in the RHS of equation 2.21) for incompressible flow with constant density $\frac{\partial \bar{u}_i}{\partial x_i} = 0$ as

$$-\overline{u_i' u_j'}\frac{\partial \bar{u}_j}{\partial x_i} = \nu_t \left(\frac{\partial \bar{u}_i}{\partial x_j} + \frac{\partial \bar{u}_j}{\partial x_i}\right)\frac{\partial \bar{u}_j}{\partial x_i}, \tag{2.23}$$

The standard model coefficients are all listed in Table 2.1. The k-ϵ turbulence model (or, in general, linear eddy viscosity models) has the disadvantages of being isotropic and unable to account for curvature effects. In order to overcome these weaknesses, non-linear formulations such as the Algebraic Reynolds Stress Model (ASM) [82] or the Explicit Algebraic Reynolds Stress Model (EASM) have been suggested [82]. At a high level of modeling, second order models have been reported in the literature [128], [129]. However the new concept based on Scale Adaptive Simulation (SAS) approach relying on the two-equations modeling seems to be attractive for unsteady simulations as presented in the following.

2.3.2 Mathematical background and basic of the SAS model

Considering that turbulent flow structures can be described by different length scales, Rotta [78] derived a transport equation for quantity kL for a simple turbulent shear flow (homogeneous shear flow), where L and k represent the integral length scale and turbulent kinetic energy, respectively. This quantity can be used to provide information for Reynolds stress tensor to close the Reynolds averaged Navier-Stokes (RANS) equations (2.16), here considered in incompressible case with $\overline{u}_i \equiv \overline{U}_i$:

$$\frac{\partial \bar{U}_i(\vec{x},t)}{\partial t} + \bar{U}_j(\vec{x},t)\frac{\partial \bar{U}_i(\vec{x},t)}{\partial x_j} = \frac{1}{\rho}\frac{\partial \bar{P}(\vec{x},t)}{\partial x_i} + \frac{\partial}{\partial x_j}\left(\nu\frac{\partial \bar{U}_i(\vec{x},t)}{\partial x_j} - \overline{u_i' u_j'}(\vec{x},t)\right) + g_i, \tag{2.24}$$

where $\overline{u_i' u_j'}(\vec{x},t)$ is the Reynolds stress tensor to be closed. The generalizing integral length scale 2.2 in any turbulent field can be defined based on the correlation function at the time t as follows:

$$L_{ij,q}(\vec{x},t) = \frac{1}{2\overline{u_i'(\vec{x},t)u_j'(\vec{x},t)}}\int_{-\infty}^{\infty} R_{ij}(\vec{x},t,r_q)dr_q, \quad i,j,q = \{1,2,3\}, \tag{2.25}$$

where $u_i^{'}$ and R_{ij} are velocity fluctuation and the correlation functions, respectively. $\vec{x}$ and $\vec{r}$ denote position vector in the flow field and displacement vector between two points in the flow field. The overbar denotes the ensemble averaging. R_{ij} is defined as below:

$$R_{ij}(\vec{x},\vec{r},t) = \overline{u_i^{'}(\vec{x},t)u_j^{'}(\vec{x}+\vec{r},t)}. \tag{2.26}$$

Note that its normalized expression leads to the correlation coefficient (here correlation function) in 2.2. In equation 2.25, q denotes the direction of integration, say stream wise (x_1), normal (x_2) or span wise (x_3). Regarding shear flows, Rotta[78] assumed a simplified form for the integral length scale as follows:

$$\Psi = k(\vec{x})L(\vec{x}) = \frac{3}{16}\int_{-\infty}^{\infty} R_{ii}(\vec{x},r_{x_2})dr_{x_2}, \tag{2.27}$$

where x_2 denotes the shear strain direction and $\frac{3}{16}$ is a scaling factor enabling to capture the isotropic limit.

Rotta[78] then derived a transport equation for Ψ regarding homogeneous turbulent shear flows by integrating the simplified transport equation of R_{ij} in r_{x_2} direction. This then then appeared in the following form:

$$\begin{aligned} &\bar{U}_1(\vec{x})\frac{\partial\Psi}{\partial x_1} + \bar{U}_2(\vec{x})\frac{\partial\Psi}{\partial x_2} = \\ - &\overline{u_1^{'}u_2^{'}}(\vec{x})\left(\xi_1 L(\vec{x})\frac{\partial\bar{U}_1(\vec{x})}{\partial x_2} + \xi_2 L^2(\vec{x})\frac{\partial^2\bar{U}_1(\vec{x})}{\partial x_2^2} + \xi_3 L^3(\vec{x})\frac{\partial^3\bar{U}_1(\vec{x})}{\partial x_2^3}\right) \\ - &cc_L k(\vec{x})^{\frac{3}{2}} + \frac{\partial}{\partial x_2}\left\{k_L\sqrt{k(\vec{x})}L\left[L(\vec{x})\frac{\partial k(\vec{x})}{\partial x_2} + \alpha_L k(\vec{x})\frac{\partial L(\vec{x})}{\partial x_2}\right]\right\}. \end{aligned} \tag{2.28}$$

Rotta[78] proposed the value 1.2 for ξ_1 based on measurements for a homogeneous shear flow performed by Rose [137], while the other remaining model constants will be determined later.

Due to the axisymmetric behavior of R_{12} in homogeneous shear flows the Rotta's transport equation does not include the term with second velocity derivative . Therefore, the final transport equation proposed by Rotta[78] for homogeneous shear followed from equation 2.29 as below:

$$\begin{aligned} &\bar{U}_1(\vec{x})\frac{\partial\Psi}{\partial x_1} + \bar{U}_2(\vec{x})\frac{\partial\Psi}{\partial x_2} = \\ - &\overline{u_1^{'}u_2^{'}}(\vec{x})\left(\xi_1 L(\vec{x})\frac{\partial\bar{U}_1(\vec{x})}{\partial x_2} + \xi_3 L^3(\vec{x})\frac{\partial^3\bar{U}_1(\vec{x})}{\partial x_2^3}\right) \\ - &cc_L k(\vec{x})^{\frac{3}{2}} + \frac{\partial}{\partial x_2}\left\{k_L\sqrt{k(\vec{x})}L\left[L(\vec{x})\frac{\partial k(\vec{x})}{\partial x_2} + \alpha_L k(\vec{x})\frac{\partial L(\vec{x})}{\partial x_2}\right]\right\}. \end{aligned} \tag{2.29}$$

Where ξ_1, ξ_3 are model constants. Three observations need to be pointed out. First, symmetry considerations (see [130]) showed that in the case of wall bounded flows with no symmetry breaking condition the third velocity derivative is vanishing and the term with second velocity derivative is remaining. Second, for complex shear flows with symmetry breaking conditions both terms are present. However, in this study following transport equation regarding wall bounded shear flows will be considered.

$$\begin{aligned} &\bar{U}_1(\vec{x})\frac{\partial \Psi}{\partial x_1} + \bar{U}_2(\vec{x})\frac{\partial \Psi}{\partial x_2} = \\ -\ & \overline{u_1^{'}u_2^{'}}(\vec{x})\left(\xi_1 L(\vec{x})\frac{\partial \bar{U}_1(\vec{x})}{\partial x_2} + \xi_2 L^2(\vec{x})\frac{\partial^2 \bar{U}_1(\vec{x})}{\partial x_2^2}\right) \\ -\ & cc_L k(\vec{x})^{\frac{3}{2}} + \frac{\partial}{\partial x_2}\left\{k_L\sqrt{k(\vec{x})}L\left[L(\vec{x})\frac{\partial k(\vec{x})}{\partial x_2} + \alpha_L k(\vec{x})\frac{\partial L(\vec{x})}{\partial x_2}\right]\right\}, \end{aligned} \tag{2.30}$$

where the term including third derivative has not been included due to requirement of particular numerical treatment. Third, as mentioned before, Rotta's transport equation has been derived for homogeneous shear flows based on local isotropy concepts. These concepts are only legitimate for regions away from the wall (very high Reynolds number) where the cascade process occurs. However, information for the Reynolds stress tensor to close the RANS equations is needed for the whole domain. Therefore, a novel combination of modified form of equation 2.31 concerning complex three dimensional shear flows together with an appropriate near wall turbulence model would be a reasonable approach. Menter et al.[141] proposed a seamless hybrid approach using a modified form of equation 2.30 and denoted it as $SST - SAS$ model.
for brevity reasons note that from now on in the rest of this section the variable $(\vec{x})$ is dropped from the quantities.

The $SST - SAS$ **model**: Based solely on the dimensional analysis, Menter et al. [141] modified and simplified equation 2.30 as follows:

$$\bar{U}_1\frac{\partial \Psi}{\partial x_1} + \bar{U}_2\frac{\partial \Psi}{\partial x_2} = \frac{\Psi}{k}P_k\left(\tilde{\xi}_1 + \tilde{\xi}_2\left(\frac{L}{L_{vk}}\right)^2\right) - \tilde{\xi}_3 k^{\frac{3}{2}} + \frac{\partial}{\partial x_2}\left\{\frac{\nu_t}{\sigma_\Psi}\frac{\partial \Psi}{\partial x_2}\right\}, \tag{2.31}$$

where L_{vk} denotes the von-Karman length scale $\left(L = 0.41\left|\frac{\frac{\partial \bar{U}_1}{\partial x_2}}{\frac{\partial^2 \bar{U}_1}{\partial x_2^2}}\right|\right)$ and P_k the production of turbulent kinetic energy $\left(P_k = -\overline{u_1^{'}u_2^{'}}\frac{\partial \bar{U}_1}{x_2}\right)$.
The first term on the right hand side models the production, the second term dissipation and the third term postulates the diffusion using simple gradient approach.
To apply equation 2.31 to complex flows, an evaluation of the first and second derivatives in L is needed. For this purpose, Menter et al.[141] defined following norms for the first and the second derivatives of velocity:

$$\|\bar{U}^{'}\| = S = \sqrt{2S_{ij}S_{ij}}; \quad S_{ij} = \frac{1}{2}\left(\frac{\partial \bar{U}_i}{\partial x_j} + \frac{\partial \bar{U}_j}{\partial x_i}\right).$$

$$\|\bar{U}''\| = \sqrt{\frac{\partial^2 \bar{U}_i}{\partial x_j \partial x_j}\frac{\partial^2 \bar{U}_i}{\partial x_k \partial x_k}}; \quad L_{vk} = 0.41 \left|\frac{U'}{U''}\right|.$$

Instead of equation for kL, Menter et al.[141] transformed the transport equation 2.31 to a one with new variable $\Phi = \sqrt{k}L$ and proposed following two-equations model for complex (3-dimensional) flows called K square-root-KL (KSKL) model :

$$\frac{\partial k}{\partial t} + \bar{U}_j \frac{\partial k}{\partial x_j} = P_k - c_\mu^{0.75}\frac{k^2}{\Phi} + \frac{\partial}{\partial x_j}\left(\frac{\nu_t}{\sigma_k}\frac{\partial k}{\partial x_j}\right) \tag{2.32}$$

$$\frac{\partial \Phi}{\partial t} + \bar{U}_j \frac{\partial \Phi}{\partial x_j} = \frac{\Phi}{k}P_k \left(\zeta_1 - \zeta_2 \left(\frac{L}{L_{vk}}\right)^2\right) - \zeta_3 k + \frac{\partial}{\partial x_j}\left(\frac{\nu_t}{\sigma_\Phi}\frac{\partial \Phi}{\partial x_j}\right) \tag{2.33}$$

$$\nu_t = c_\mu^{\frac{1}{4}}\Phi, \quad \Phi = \sqrt{k}L \quad \zeta_1 = 0.8, \quad \zeta_2 = 1.47, \quad \zeta_3 = 0.028, \quad \sigma_k = \sigma_\Phi = 2/3.$$

The KSKL model was transformed into $K - \omega$ ($\omega = \frac{\epsilon}{k}$) framework resulting in an additional term in the transport equation for ω given as below:

$$Q_{SAS} = max\left[\zeta_2 S^2 \left(\frac{L}{L_{vk}}\right) - C_{SAS}\frac{2k}{\sigma_\Phi} max\left(\frac{1}{k^2}\frac{\partial k}{\partial x_j}\frac{\partial k}{\partial x_j}, \frac{1}{\omega^2}\frac{\partial \omega}{\partial x_j}\frac{\partial \omega}{\partial x_j}\right), 0\right], \tag{2.34}$$

with $C_{SAS} = 2$. This term has been added to the ω transport equation of the $k - \omega - SST$ model [127]. Where the max function and the $k-$derivative term have been empirically introduced to avoid numerical instability of the model regarding attached flows.
With respect to this modeling approach some observations can be pointed out:

1. According to the finding of [128], the $SST - SAS$ model has shortcomings dealing with flows like diffuser, hill flow and channel flow, where the flow instabilities are relatively weak.

2. In the forms of hybride LES/RANS it should be noted that neither $SST - SAS$ nor DDES (delayed detached Eddy simulation) are able to switch from RANS to scale resolving mode without an explicit introduction of synthetic turbulence. This might be due to the used norm for the second derivative of the velocity and the resulting additional source terms, that are responsible for the scale adaptivity of resolution.

Modified SAS approach by Mehdizadeh et al. [144]
The approach is to consider a continuum-mechanics consistent norm and then to introduce a zonal approach in order to accommodate in a consistent way the near wall turbulence treatment and the features of equation 2.30.

The source term of the equation 2.30 includes first and second derivative of velocity which is similar to the Von-Karman relationship. Therefore, the equation constants have to be determined, so that the equation in the limiting case returns the Von-Karman relationship for integral length scale. First of all the value of ξ_2 is determined based on the local turbulence energy equilibrium. This leads to the following expression for L:

$$L = \frac{c_L - \xi_1}{\xi_2} \left| \frac{\frac{\partial \bar{U}_1}{\partial x_2}}{\frac{\partial^2 \bar{U}_1}{\partial x_2^2}} \right| . \tag{2.35}$$

Comparison of the above relation with the von-Karman expression results in $\xi_2 \approx -1.15$.
In order to apply equation 2.35 to complex flows, two mathematically consistent Norms for both first and second velocity derivatives have to be defined. The modified form of Rotta's transport equation (equation 2.30) for complex (3-dimensional) shear flows can then be written as below:

$$\frac{\partial \Psi}{\partial t} + \bar{U}_j \frac{\partial \Psi}{\partial x_j} = \left(\xi_1 L + \xi_2 L^2 \frac{\|\bar{U}''\|}{\|\bar{U}'\|} \right) P_k - c_L c k^{\frac{3}{2}} + \frac{\partial}{\partial x_j} \left\{ k_L \sqrt{k} L \left[L \frac{\partial k}{\partial x_j} + \alpha_L k \frac{\partial L}{\partial x_j} \right] \right\} \tag{2.36}$$

$\xi_1 = 1.2, \quad \xi_2 = -1.15, \quad c = 0.18, \quad c_L = 0.72$

in which 2.36, $\|\bar{U}'\|$, $\|\bar{U}''\|$ denote the norms for the first and second velocity derivative and P_k is the production of turbulent kinetic energy. They are defined as:

$$\|\bar{U}'\| = S = \sqrt{2 S_{ij} S_{ij}}; \quad S_{ij} = \frac{1}{2} \left(\frac{\partial \bar{U}_i}{\partial x_j} + \frac{\partial \bar{U}_j}{\partial x_i} \right)$$

$$\|\bar{U}''\| = \sqrt{\frac{\partial^2 \bar{U}_i}{\partial x_j \partial x_k} \frac{\partial^2 \bar{U}_i}{\partial x_j \partial x_k}}$$

$$P_k = -\overline{u_i' u_j'} \frac{\partial \bar{U}_i}{\partial x_j}.$$

Remaining in the framework of two-equation turbulence model, it is of practical interest to concentrate on $k - \epsilon$ model. Equation 2.36 is then transformed to a transport equation for dissipation rate using $k^{\frac{3}{2}}/\epsilon$ as the integral length scale along with the common transport equation for the turbulent kinetic energy. To determine two remaining model constants (k_L , α_L) within the transformation following assumptions have been made:
1. Common gradient diffusion model for ϵ in the resulting modified transport equation.
2. No explicit appearance of diffusion term of the turbulent kinetic energy in the modified transport equation for ϵ.

The above assumptions result in the following values for model constants:
$\alpha_L = 1, \qquad k_L = 0.09.$
Finally, the resulting modified set of equations for turbulent kinetic energy and dissipation rate is

as follows:

$$\begin{aligned}\frac{\partial \epsilon}{\partial t}+\bar{U}_j\frac{\partial \epsilon}{\partial x_j} &= \underbrace{1.3}_{C_{\epsilon_1}}\frac{\epsilon}{k}P_k-\underbrace{2.36}_{C_{\epsilon_2}}\frac{\epsilon^2}{k}+1.15\sqrt{k}\frac{\|\bar{U}''\|}{\|\bar{U}'\|}P_k+\frac{\partial}{\partial x_j}\left(\nu_t\frac{\partial \epsilon}{\partial x_j}\right) \\ &- 0.33\left(\frac{\partial k}{\partial x_j}\right)^2+5\frac{\nu_t}{k}\left(\frac{\partial k}{\partial x_j}\right)\left(\frac{\partial \epsilon}{\partial x_j}\right)-2\frac{\nu_t}{\epsilon}\left(\frac{\partial \epsilon}{\partial x_j}\right)^2\end{aligned} \tag{2.37}$$

$$\frac{\partial k}{\partial t}+\bar{U}_j\frac{\partial k}{\partial x_j}=P_k-\epsilon+D_k, \tag{2.38}$$

where P_k, D_k and ν_t denote production, diffusion of turbulent kinetic energy and turbulent eddy viscosity respectively. It is worth mentioning that the equations 2.38 and 2.38 are supposed to describe mainly the unsteady cascade process in regions away from the wall, so that a zonal approach would be one reasonable way to incorporate near wall effects in shear flows by means of blending of the dissipation rate using step function.

Zonal SAS approach [144]
As information of k and ϵ is needed for the whole flow region, the equations 2.38 and 2.38 should be coupled through blending of the ϵ-equation to corresponding k and ϵ equations which are mostly able to capture viscous effects at the wall vicinity, (e.g. Chien[142], and Launder-Sharma [80]). This combination of a low Reynolds number model with the modified set of transport equations (Eq. 2.38, 2.38) has been termed zonal Scale-Adaptive hybrid approach. This approach allows for describing both flow regions with the turbulence model of the same representation and therefore with a continuous behavior of the flow quantities.

At this point it is worth noticing that the conceptual development of this approach is in good mind with finding of Spalart [126], regarding the URANS method. He noted that in a URANS approach, the turbulence model itself is mainly responsible for resolving of the turbulence incoherent structures, while the regions with no separation (regions in which the viscous effects cannot be neglected) are within the reach of current steady RANS method. Incoherent structures are mainly existing in regions with very high local Reynolds number (negligible viscous effects) in which the cascade process takes place. Regarding the modification of C_{ϵ_2}, it should be noted that this modification is in a good agreement with the finding of Horton et al.[135] and [144] in shear flows. They have shown that in shear flows, turbulence grows in regions with dominated non-linear effects (negligible viscous effects). This corresponds to the values greater than 2 for $C_{\epsilon 2}$ in $k-\epsilon$ framework, where the model is supposed to describe the non-linear effects (cascade process) away from the wall.

The main advantage of this approach against LES/URANS zonal approach is that, there is no need to define matching conditions at the interface. Therefore, the discontinuities of quantities around the interface existing in common zonal approaches are absent as only quantities k and ϵ are solved. The only remaining issue is to determine the location of the interface. For the first attempt the interface has been located at $x_2^+ = 100$ according to Pope[129]. He showed that in wall bounded flows, from $x_2^+ = 100$ the effects of molecular viscosity are completely negligible. In regions with high Reynolds number, $x_2^+ > 100$, the modified ϵ transport equation is active. The additional source terms existing in this equation allow the model for resolving the turbulent incoherent structures, while the near wall turbulence model returns a steady RANS solution for the near wall region. More details of this model can be found in [144].

3 Multiphase flow properties and description approaches

3.1 Relevant parameter characterizing dispersed phase flows

Let us assume a polydisperse multiphase flow systems characterized by spherical particles.

Volume fraction: It describes the amount of dispersed phase volume within the gas phase. The volume fraction is used to characterize the level of interaction between the different phases. It is defined by:

$$\alpha_p = \frac{\sum_{l=1}^{n} V_{p,l}}{\delta V}, \tag{3.1}$$

where $V_{p,l}$ denotes the volume of particle l within the considered control volume δV. The summation is done over all existent particle n. The continuous phase volume fraction is defined in a similar way:

$$\alpha = \frac{\delta V}{\delta V}, \quad \text{with:} \quad \alpha + \alpha_p = 1 \tag{3.2}$$

Mass loading: It is defined by:

$$Z_l = \frac{\dot{m}_p}{\dot{m}}, \tag{3.3}$$

where $\dot{m}_p$ represents the particles mass flux, while $\dot{m}$ represents the mass flux of the continuous phase.

Particle Reynolds number it was revealed to be an important parameter to characterize the effect of dispersed phase on the turbulence variation of carrier gas. It is defined by:

$$Re_P = \frac{\rho D_p \left| U - u_p \right|}{\mu}, \tag{3.4}$$

where ρ, μ and U represent the density, viscosity and absolute velocity of the continuous phase, respectively, D_p is the particle diameter while u_p denotes the absolute velocity of dispersed phase.

Particle relaxation time: defines the ability of a given particle to react to the carrier gas. The particle relaxation time yields the time taken by a particle to respond on the fluid velocity modification. It is defined by:

$$\tau_p = \frac{\rho_p D_p^2}{18\mu}, \tag{3.5}$$

where ρ_p is the particle density.

Stokes number: measures the inertia of one particle. It is defined as the ratio of the particle relaxation time to the turbulent time scale. The Stokes number is important in order to characterize interaction processes with the particle (such as separation, deposition, modulation, etc.)

$$St = \frac{\tau_p}{T_{ch}}, \tag{3.6}$$

where T_{ch} denotes the turbulent characteristic time scale.

3.2 Main Multi-phase Flow Approaches

The numerical methods used in solving dispersed multi-phase flows are basically classified in three categories:

1. The Eulerian Lagrangian method treats the fluid as a continuum and the particles as discrete entities.
2. The two-fluid method treats the particle phase and carrier phase as interpenetrating and interacting continuum.
3. The Probability Density Function (PDF) method describes the flows by the joint statistical properties of the gas phase properties and the droplet properties.

3.2.1 Eulerian Eulerian approach

The classical two-fluid models have been the subject of many publications either in the mathematics community [115] or in the engineering one [51]. The Eulerian-Eulerian (E-E) approach treats both phases as continua. The behavior of dispersed and gas phase is characterized by using partial differential transport equations which describe the flow of the fluids. This approach is more suitable in case of dense two-phase flow in which the volume fraction of both phases may be greater than 10^{-3}. Such a formulation for both phases lends itself more naturally to parallel computing and transient flow calculations. The reason behind this is that parallel numerical computation is achieved by arranging fluid-blocks to CPU and not particles. The multiple dispersed phases have similar transport equations as the gas phase which makes the implementation not very complex. The coupling between two phases is easily done and the convergence criteria can be clearly defined [51].

The difficulties of Eulerian-Eulerian approach are the modeling of turbulent diffusion of the dispersed phase and the closure of the interface exchange terms. The followings are additional complex problems to solve while using E-E:

- Fluctuations of the dispersed phases [51],
- Particle wall interaction [117],
- Boundary conditions,
- Numerical diffusion [118].

The major drawback of the Eulerian-Eulerian approach is the inability to capture the polydispersion in size of the spray (different diameters, density...). One should therefore treat every class of particles diameter as a separate phase. Recently, alternatives to the Lagrangian or the Multi-Fluid approaches have been developed, which makes it possible to account for population dynamics in an efficient manner. Most of these methods rely upon a formulation involving moments (or some other information) of the particle size distribution function, and are divided into three categories: MOM (Method of Moments), QMOM (Quadrature Method of Moments) and DQMOM (Direct Quadrature Method of Moments) [145] [146] [147] [149] .

3.2.2 PDF approach

In this approach the non-continuous phase is thought of as a cloud of material elements. Its behavior is driven by a probability function depending on the velocity, temperature, mass of droplets and the velocity, temperature and species concentration of the gas phases seen by droplets. Joint-PDF transport equation characterizes the unsteady evolution and convection by the velocity mean field in the physical space, and describes the PDF evolution in the phase space. For this reason some conditional average over the phase space due to dispersion, phase change, heat transfer of droplets, and the momentum, heat, and mass transport of gas particles seen by droplets have to be modeled.

The joint PDF transport equation of turbulent gas-droplet flows is [116]

$$\begin{aligned}
\frac{\partial P}{\partial t} + V_{pi}\frac{\partial P}{\partial t} = & -\frac{\partial}{\partial V_{pi}}\left[P\left\langle S_{up,i}|_{V_{pi},\theta_p,M_p,V_{gi,p},\theta_{g,p},\xi_{g,p}}\right\rangle\right] \\
& -\tfrac{\partial}{\partial M_p}\left[P\left\langle S_{mp,i}|_{V_{pi},\theta_p,M_p,V_{gi,p},\theta_{g,p},\xi_{g,p}}\right\rangle\right] \\
& -\tfrac{\partial}{\partial \theta_p}\left[P\left\langle S_{hp,i}|_{V_{pi},\theta_p,M_p,V_{gi,p},\theta_{g,p},\xi_{g,p}}\right\rangle\right] \\
& -\tfrac{\partial}{\partial V_{gi,p}}\left[P\left\langle S_{ug,i}|_{V_{pi},\theta_p,M_p,V_{gi,p},\theta_{g,p},\xi_{g,p}}\right\rangle\right] \\
& -\tfrac{\partial}{\partial \theta_{g,p}}\left[P\left\langle S_{hg,i}|_{V_{pi},\theta_p,M_p,V_{gi,p},\theta_{g,p},\xi_{g,p}}\right\rangle\right] \\
& -\tfrac{\partial}{\partial \xi_{g,p}}\left[P\left\langle S_{yp,i}|_{V_{pi},\theta_p,M_p,V_{gi,p},\theta_{g,p},\xi_{g,p}}\right\rangle\right]
\end{aligned} \tag{3.7}$$

where $\left\langle S|_{V_{pi},\theta_p,M_p,V_{gi,p},\theta_{g,p},\xi_{g,p}}\right\rangle$ is the conditional average of S over the space, V_{pi},θ_p, M_p,$V_{gi,p}$,$\theta_{g,p}$ and $\xi_{g,p}$ representing the velocity, temperature, mass of droplets and the velocity, temperature, and species concentration of gas phase seen by the droplets in the phase space, respectively.

The RHS of the equation 3.7 describes the shift of the joint-PDF in the phase space because of the dispersion, phase change, heat transfer of droplets, and the momentum, heat, and mass transport of gas phase seen by droplets, respectively. If one combines the gas phase equations with the turbulence modeling, this leads to the Reynolds time-averaged in Eulerian coordinates. They are solved using the Finite Volume method. The PDF model of the dispersed phase is solved using a Lagrangian approach in the phase space. Based on the properties of PDF, the averaged value of a generalized variable, as a function of phase-space, can be obtained by integration in the phase space [116].

The ability of the PDF approach to provide more detailed and accurate droplets statistics at any location of the flow field makes the pdf approach attractiver over the Eulerian-Lagrangian approach (see 3.2.3).

Comparison of the PDF approach and the traditional Eulerian-Eulerian approach shows that the PDF approach can easily treat the droplets with different initial sizes, temperatures, and velocities. The disadvantages of this model is its needs of more computation time compared to the two-fluids or Lagrangian models.

3.2.3 Eulerian-Lagrangian approach

The Eulerian-Lagrangian models (E-L) treat the fluid as a continuum and the particles (dispersed phase) as discrete entities ([18], [68], [39] and [42]).

Eulerian-Lagrangian approaches are divided into two steps [35]. The first step include the computation of the Eulerian part while the second step uses the Lagrangian approach to solve the dispersed phase. During these steps the algorithm alternates repeatedly between the two steps till reaching convergence criteria of the coupling between the phases. The coupling is reached via source terms, which are calculated for each variable at every control volume [18]. Most of the works in E-L approach neglect the volume change of the continuous phase due to the presence of particles/droplets [68], [120]. The transport equations are solved with a constant volume of the cell as well. This hypothesis will become critical in region with high concentration, e.g. nozzle outlet zone. A second assumption often used while solving two-phase flow with E-L approach is that a numerical parcel does not represent only one real particle but it represents a group of real particles [121]. This assumption reduces the computational time. However this can produce very poor numerical results due to poor statistics. The statistical mean values of the dispersed phase need high number of parcels. This leads to high computational costs making it disadvantage of the Eulerian-Lagrangian approach.

The E-L method is suited for dilute and dense multi-phase flows where, the computing time is increasing with the number of tracked parcels. However, the fluid particle interaction to model droplet evaporation, collision, wall interaction etc. is physically concrete and clear and makes it as an evident advantage of E-L approach [19]. Therefore this approach is adopted in this work. Its main features are addressed in detail in the next section.

4 Eulerian-Lagrangian Approach

4.1 Eulerian treatment of the continuous (carrier) phase

The carrier phase is considered as continuum phase and described using the Reynolds averaging method. For this purpose, the governing transport equations are solved for mass, momentum, energy and required turbulent quantities. The volume variation of the carrier phase as consequence of the presence of liquid particles is neglected. The non-stationary, general form of the transport equations applied (see equations 2.15-2.18) [2] emerges as

$$\frac{\partial \rho \overline{\phi}}{\partial t} + \frac{\partial \rho \overline{u_j} \overline{\phi}}{\partial x_j} = \frac{\partial}{\partial x_j} \left(\rho \Gamma \frac{\partial \overline{\phi}}{\partial x_j} - \rho \overline{u_i'' \phi''} \right) + \overline{S}_\phi + \overline{S}_{\phi,p,s} + \overline{S}_{\phi,p,v}, \tag{4.1}$$

in which ϕ may represent the mean value of mass and velocity, the turbulent kinetic energy and turbulent dissipation rate, respectively, while u, v and w are fluid velocity components in the stream wise (x), normal (y) and the span wise(z) direction. Γ represents an effective diffusion coefficient, S_ϕ the well-known turbulence source term as in single phase flow cases ([23], [24], [25]) and $\overline{S}_{\phi,p}$ the source term for the classical two-way coupling in absence of evaporation and combustion. The term, $\overline{S}_{\phi,p,v}$, takes into consideration the transfer caused by the phase transition processes, like evaporation described below. These terms are listed in Table 4.1. Thereby quantities u_p, v_p and w_p represent the velocity components of particles, g_x, g_y, g_z the gravitation acceleration in x, y and z directions, t the time and Δt is the time step. V_{ijk}, $\dot{m}_p$ and N_p denote volume of control volume, particle flux and number of particles in the control volume, respectively. As turbulence closure the standard $k - \epsilon$ turbulence model is used.

4.2 Lagrangian treatment of the dispersed phase

In this work, a spherical, small, non deformable and non-rotating particle is considered. The equation of motion illustrates the second law of Newton which mentions that the sum of forces acting upon a mass provides its acceleration. Following the Basset-Boussinesq-Oseen equations, the particle position x_{pi} and velocity U_{pi} are described by (see e.g. [27], [23], [20]):

$$\frac{dx_{pi}}{dt} = U_{pi} \tag{4.2}$$

Table 4.1: Source terms

ϕ	$\overline{S}_{\phi,p}$	$\overline{S}_{\phi,p,v}$
1	0	$-\sum_p \frac{\dot{m}_p N_{p,v}}{V_{i,j,k}}$
$\overline{u}$	$-\sum_p \frac{\dot{m}_p N_p}{V_{i,j,k}} \left[\left(u_p^{t_n+\Delta t} - u_p^{t_n}\right) - g_x \Delta t\right]$	$\sum_p \frac{\dot{m}_p N_{p,v}}{V_{i,j,k}} u_p$
$\overline{v}$	$-\sum_p \frac{\dot{m}_p N_p}{V_{i,j,k}} \left[\left(v_p^{t_n+\Delta t} - v_p^{t_n}\right) - g_y \Delta t\right]$	$\sum_p \frac{\dot{m}_p N_{p,v}}{V_{i,j,k}} v_p$
$\overline{w}$	$-\sum_p \frac{\dot{m}_p N_p}{V_{i,j,k}} \left[\left(w_p^{t_n+\Delta t} - w_p^{t_n}\right) - g_z \Delta t\right]$	$\sum_p \frac{\dot{m}_p N_{p,v}}{V_{i,j,k}} w_p$
k	$\overline{u_i S_{ui,p}} - \overline{u_i}\,\overline{S_{ui,p}}$	$\overline{u_i S_{ui,m}} - \overline{u_i}\,\overline{S_{ui,m}} + 1/2(\overline{u_i^2}\,\overline{s_{\rho,m}} - \overline{u_i^2 s_{\rho,m}})$
ε	$c_{\varepsilon,3}^{k-\varepsilon} \frac{\varepsilon}{k} S_{k,p}; \quad c_{\varepsilon,3}^{RS} \frac{\varepsilon}{k} S_{k,p}^{RS}$	$c_{\varepsilon,3}^{k-\varepsilon} \frac{\varepsilon}{k} S_{k,p,v}; \quad c_{\varepsilon,3}^{RS} \frac{\varepsilon}{k} S_{k,p,v}^{RS}$

$$\frac{dU_{pi}}{dt} = \frac{3}{4} \frac{C_D}{D_p} \frac{\rho}{\rho_p} |\overrightarrow{U} - \overrightarrow{U_p}|(U_i - U_{pi}) + \frac{\rho_p - \rho}{\rho_p} g_i \tag{4.3}$$

Only the drag and gravity forces are considered in Eq. 4.3 while the other forces, like the Basset history term, the added mass effect and the unsteady drag effect are negligibly small for large density ratios ($\frac{\rho}{\rho_p} << 1$) as it is the case in this study. The drag coefficient used within this work is determined for a spherical and not deformable particle by:

$$C_D = \begin{cases} \frac{24}{Re_p}(1 + 0.15(Re_p)^{0.687}), & Re_p < 1000 \\ 0.44 \qquad\qquad\qquad\qquad , & Re_p > 1000 \end{cases} \tag{4.4}$$

To completely evaluate the drag force, the fluid velocity is needed along with a dispersion model(see 5.2). Because the droplets undergo phase change (evaporation), the mathematical description of this process is provided in 5.3.

4.3 Interaction of phases and two way coupling

Performed simulations within this thesis considers a full two way coupling (see 6.3.3), i.e. taking into account the effect of presence of particles/droplets on the carrier phase. This involves interactions in momentum, turbulence quantities, energy and mass in addition to dispersion effects on droplets. In 6.3.3 the two way coupling (for non-evaporating droplets) with respect to different modulation models will be introduced. Thereafter, the influence of the turbulence of carrier gas on the particles (in terms of dispersion model) will be illustrated (see 6.3.3).

The influence of the dispersed phase on the fluid motion can be treated as an extra force exerted on the carrier gas when the particles/droplets have much larger density than surrounding fluid, as it is the case in the present work (see Table 4.1). Thus, the momentum transfer from the dispersed phase to the carrier phase is included by adding the reaction force against the surface force acting on the particle/droplet to the Navier-Stokes equation 4.1. This model is known as force coupling model or particle-source-in-cell (PSI-Cell) model proposed by Crowe et al. [87]. To read more about two-way coupling, see 6.3.3.

5 Two-phase system and microprocesses under investigation

Turbulent spray systems are especially investigated in this work. The study includes physical phenomena of atomization (secondary breakup) along with droplet-droplet interactions, phase change process, especially the droplet evaporation and the full two-way coupling between phases (dispersion, modulation, etc.)

5.1 Atomization

In the sense of a broader definition, breakup includes the process when bulk liquid disintegrates into droplets under the effect of the acting internal and external forces and also the process when an existing droplet disintegrates into at least two, smaller droplets, or emits a larger number of significantly smaller droplets. Based on this distinction, the entire breakup process can be split up into two basic parts: the primary and secondary breakup, as discussed below.

5.1.1 Primary breakup

When a liquid emerges from a plain-orifice atomizer, such as a diesel injector nozzle, and the injection velocity and the level of cavitation does not exceed a certain level, it has a continuum body of cylindrical form. The various internal and external forces competing on the surface of this liquid column create oscillations and perturbations of the surface [124]. If these oscillations and perturbations are amplified to a critical extent, the liquid body disintegrates into droplets. This process is referred to as primary breakup, and is very important because with initiating the atomization process and determining the extent of the liquid core, it provides the initial conditions for the dispersed flow region.

Depending on the physical conditions, this process can be diverse in nature, exhibiting substantially different characteristics. The categorization of these breakup types can be based on various considerations. However, a fundamental platform is provided by the three most important physical parameters related to spray breakup:

1. The Reynolds number as representing ratio of inertial forces to viscous forces, it is defined as displayed in 5.1 [124] [111]:

$$Re = \frac{u\rho_l D}{\mu_l} \tag{5.1}$$

2. The Weber number represents the ratio of aerodynamic force to the force of surface tension, and can be defined in two ways, depending on the physical mechanisms that are aimed to be described [111]

$$We_g = \frac{u^2 \rho_g D}{\sigma} \tag{5.2}$$

$$We_l = \frac{u^2 \rho_l D}{\sigma} \tag{5.3}$$

   In experimental analysis there is some degree of freedom in choosing the Weber number, since experimental researchers use it to describe their results with minimum number of parameters. The choice might depend on type of the experiment, but e.g. for experiments without density variation liquid as well as gas Weber number could be chosen. The occurrence and type of breakup can be very well related to the gas Weber number valid for the droplet in consideration. Hence a lot of numerical models use this characteristic to switch from one model mechanism to another.

3. The third relevant number is the Ohnesorge number, also often referred to as the Laplace number, the viscosity number or the Z number, representing the ratio of liquid viscous forces to surface tension forces. It is defined as [59]:

$$Oh = \frac{\sqrt{We_l}}{Re} = \frac{\mu_l}{\sqrt{\sigma D \rho_l}} \tag{5.4}$$

   If the Ohnesorge number is used to account for the viscous forces during breakup in general, the assumption has to be made that the viscosity of surrounding gas is small compared to that of the liquid, since the Ohnesorge number involves droplet properties only.

5.1.2 Secondary breakup

In the traditional approach for spray computation, the Eulerian equations for gaseous phase are solved along with a Lagrangian model for droplet transport with two-way coupling of mass, momentum, and energy exchange between the two phases [88]. The standard approach is to first perform spray patternation studies for the injector used in combustion chambers and measure the size distributions at various cross-sections from the injector. These distributions at the nearest position to the nozzle are then used as an input to a numerical simulation which then computes the secondary atomization of the injected droplets. The secondary atomization is typically modeled by standard deterministic breakup models based on Taylor Analogy Breakup (TAB) [89], or wave [90] models. However, this requires performance of experimental tests for any new injector design which can be very costly.

Liquid ’blobs’ with the size of the injector diameter are introduced and undergo atomization based on the balance between aerodynamic and surface tension forces acting on the liquid phase.

In the TAB model [89], oscillations of the parent droplet are modeled in the framework of a spring mass system and breakup occurs when the oscillations exceed a critical value. In the wave model, new droplets are formed based on the growth rate of the fastest wave instability on the surface of the parent blob [90]. Both models are deterministic with 'single-scale' production of new droplets.

In many combustion applications, however, injection of liquid jet takes place at high relative velocity between the two phases (high initial Weber number). Under these conditions, intriguing processes such as turbulence-induced breakup [52], multiple droplet collision in the dense spray region [92], fluctuations due to cavitating flow inside the injector [93], etc., contribute to the process of atomization. At each spray location, this may result in droplet formation over a large spectrum of droplet-sizes and is not captured by the above models. In order to improve the TAB model, an enhanced TAB model (ETAB), where the product droplet size was obtained via a breakup cascade modeled by an exponential law, was proposed [94]. The parameters of this distribution function were derived from experimental data to achieve better performance of the model.

To predict the essential global features of these complex phenomena, a stochastic approach for droplet breakup taking into account a range of product-droplet sizes is imperative (Gorokhovski, 2001 [104]). The process of air-blast breakup can be considered in the framework of cascade of a uncorrelated breakage events in series, independently from the initial distribution of sizes. Such a stochastic modeling of droplets production under these hypotheses down to the critical (or maximum stable) size is followed in this work.

The cascade idea of breakup comes from the early work of Kolmogorov written in 1941 [55]. in his work, Kolmogorov described the breakup of solid particles as a discrete random process, where the probability to break each parent particle on a given number of parts is independent of the parent particle size. From Lyapunov's theorem, Kolmogorov has pointed out that such a general assumption leads to the log-normal distribution of particle size in the long-time limit. In this paper, the Kolmogorov's discrete model has been reproduced in the form of evolution equation for distribution function. The asymptotic solution of this equation has been applied to simulate the drop breakup alongside with Lagrangian model of spray dynamics.

5.1.2.1 Kolmogorov's (1941) Theory of the Particle Breakup

Following Kolmogorov [55] let us consider an ensemble of breaking solid particles at discrete time moments $t = 0, 1, 2, ...$ These time moments are scaled by the breakup frequency ν ($t = \nu t$). According to Komogorov [95], the number of particles $N(r, t)$ of size $\rho \leq r$ was selected amongst all particles $N(t)$ at a given moment t. The expectations of total number of particles and of particles of size $\rho \leq r$ were denoted as $\bar{N}(t)$ and $N(r, t)$ correspondingly. Considering an outcome of breakup per unit time $[t, t + 1]$ of a given parent particle of size r, the mean number $Q(\alpha)$ of secondary particles of size $\rho \leq \alpha r (0 \leq \alpha 1)$ was introduced. According to hypotheses of Kolmogorov, the probability to break each parent particle on a given number of parts is independent of the parent particle size. In other words, $Q(\alpha)$ does not depend of prehistory of breakup and is not influenced by others parent particles. By this assumption, Kolmogorov writes:

$$\bar{N}(r, t + 1) = \int_0^1 \left(\bar{N}(\frac{r}{\alpha}, t) \right) dQ(\alpha) \tag{5.5}$$

Introducing the logarithm of particle-size $x = Inr$, Kolmogorov pointed out that

$$T(x,t) = \frac{\bar{N}(e^x,t)}{\bar{N}(t)} = \frac{N(e^x,t)}{N(t)} \tag{5.6}$$

Further, denoting $\xi = In\alpha$ and $Q(\alpha) = Q(1)S(\xi)$, equation 5.5 is rewritten by Kolmogorov in the following form:

$$T(x,t+1) = \int_{\infty}^{0} T(x-\xi,t)dS(\xi) \tag{5.7}$$

By Lyapunov's theorem, Kolmogorov stated that from discrete model 5.7, the long-time limit form of $T(x,t)$ tends to Gaussian function. Then the main result of Kolmogorov's work is that $N(r,t)$ is asymptotically governed by log-normal law.

The Asymptotic Differential Form of the Discrete Kolmogorov's Model

Here the discrete model 5.7 is represented by its differential approximation in the long time limit. Using parabolic scaling of variables $\tau = \epsilon^2 t$, $y = \epsilon x$, where ϵ is a scaling parameter and t is scaled by breakup frequency, the equation 5.7 can be written as

$$T(y,\tau+\epsilon^2) = \int_{-\infty}^{0} T(y-\epsilon\xi,\tau)s(\xi)d\xi \tag{5.8}$$

Expanding both the left-hand side and the expression under integral in 5.8, one gets

$$T(y,\tau+\epsilon^2) = T(y,\tau) + \epsilon^2 \frac{\partial T(y,\tau)}{\partial \tau} + O(\epsilon^4) \tag{5.9}$$

$$T(y-\epsilon^2\xi,\tau) = T(y,\tau) - \epsilon\frac{\partial T(y,\tau)}{\partial y} + \frac{1}{2!}(\epsilon\xi)^2\frac{\partial^2 T(y,\tau)}{\partial y^2} + \frac{1}{3!}(\epsilon\xi)^3\frac{\partial^3 T(y,\tau)}{\partial y^3} + O(\epsilon^4) \tag{5.10}$$

Substituting these expansions in 5.8 and coming back to variables t and x, one yields:

$$\frac{\partial T(x,t)}{\partial t} + O(\epsilon^4) = -\langle\xi\rangle\frac{\partial T(x,t)}{\partial x} + \frac{1}{2!}\langle\xi^2\rangle\frac{\partial^2 T(x,t)}{\partial x^2} + \frac{1}{3!}\frac{\partial^3 T(x,t)}{\partial x^3}\epsilon^2\int_{-\infty}^{0}\xi^3 s(\xi)d\xi + O(\epsilon^4) \tag{5.11}$$

where $\langle\xi\rangle = \int_0^{-\infty} \xi s(\xi) d\xi$ and $\langle\xi^2\rangle = \int_0^{-\infty} \xi^2 s(\xi) d\xi$ are two first moments of ξ. Assuming that the integral $\int_0^{-\infty} |ln\alpha|^2 \, dQ(\alpha)$ is limited, the equation 5.11 can be written in the long-time limit $\epsilon \to 0 (t \to \infty)$, as

$$\frac{\partial T(x,t)}{\partial t} + \nu \langle\xi\rangle \frac{\partial T(x,t)}{\partial x} = \frac{1}{2!} \nu \left\langle\xi^2\right\rangle \frac{\partial^2 T(x,t)}{\partial x^2} \tag{5.12}$$

The dimensional time has been used in 5.12. The solution of 5.12 is Gaussian function. This repeats the main result of Kolmogorov [95]. At the same time, an influence of the initial distribution before breakup starts can be taken into account by using 5.12. The solution of 5.12 verifies to be:

$$T(x,t) = \int_{-\infty}^{0} \frac{1}{\sqrt{2\pi \langle\xi^2\rangle \nu t}} exp\left[-\frac{(x-x_0)^2}{2\langle\xi^2\rangle \nu t}\right] T_0(x_0 - \langle\xi\rangle \nu t) dx_0 \tag{5.13}$$

where $T_0(x_0)$ is the initial distribution of the logarithm of droplet radius and x_0 is logarithm of radius of the parent drop. One can rewrite equation 5.12 for the normalized distribution of radius $f(r)$:

$$\frac{\partial f(r)}{\partial t} = -\nu \langle\xi\rangle \frac{\partial}{\partial r}(rf(r)) + \frac{1}{2}\nu \left\langle\xi^2\right\rangle \frac{\partial}{\partial r}\left(r\frac{\partial}{\partial r}(rf(r))\right) \tag{5.14}$$

The solution of this equation has the following form:

$$f(r,t) = \frac{1}{r}\int_0^{\infty} \frac{1}{\sqrt{2\pi \langle\xi^2\rangle \nu t}} exp\left[-\frac{\left(ln\frac{r_0}{r} + \langle\xi\rangle \nu t\right)^2}{2\langle\xi^2\rangle \nu t}\right] f_0(r_0) dr_0 \tag{5.15}$$

where $f_0(r_0)$ is the initial distribution of droplet radius before breakup starts.

5.1.2.2 Implementation into Computational Code

The modeling of the spray equation is often based on Lagrangian formulation [97]. The spray is considered to be composed of discrete parcels of particles, each of which represents a group of droplets of similar size, velocity and position. These groups of droplets are followed as they interact and exchange momentum and energy with surrounding gas. The basic ideas of this method, including the modeling of turbulent dispersion of particles, are presented in [98].

Here, the Lagrangian tracking is coupled with a stochastic computing of breakup as outlined in the following. The product droplet velocity has been modeled and the breakup has been considered down to the local magnitude of the critical (or maximum stable) radius, r_{cr}. The liquid fuel was injected in the axial nozzle direction in form of discrete parcels of drops with characteristic size equal to the exit nozzle radius. The injection velocity was determined from the known liquid injection rate.

Let us consider the motion of a given $j-th$ primary parcel that undergoes breakup. Before breakup starts, the distribution function associated with this parcel is Dirac function at radius of the parent drop. After passage of time, which is inversely the breakup frequency, the new droplets arise due to breakup. In sequel, the droplet-radius distribution function changes. We suppose that the new distribution may be described according to solution 5.15 taken at $\nu t = 1$ with $\langle \xi \rangle$ and $\langle \xi^2 \rangle$ as parameters of the model.

In order to alleviate computations, we can proceed in the following way. Let us assume that once every breakup time scale, all outcomes of breakup in the given parent parcel are in mean (over many computations), recovered by one new parcel that replaces the parent one. The radius of droplet associated with produced parcel is sampled from 5.15. The new number of droplets is computed by mass conservation from the primary parcel to the secondary one. After the sampling procedure, the current time, t, prescribed for produced parcel is counted from zero and Lagrangian tracking is continued up to the moment $(\nu t = 1)$ of the further breakup. In computations, we used expressions obtained for the distribution of the logarithm of radius. The starting distribution for the logarithm of droplet radius in $j - th$ primary parcel is

$$T_{0j}(x_0) = \delta(x_0 - x_j) \tag{5.16}$$

Using this distribution function in 5.13 at $\nu t = 1$, one can express the solution by the error function erf:

$$T_j(x,t) = \frac{1}{2}\left[1 + erf\left(\frac{x - x_j - \langle \xi \rangle}{\sqrt{2\langle \xi^2 \rangle}}\right)\right] \tag{5.17}$$

The product droplet velocity is computed by adding to the primary parcel velocity a velocity w_{bu}, which is randomly distributed in a plane normal to the relative velocity vector between the parent droplet and gas. The quantity of w_{bu} is determined by the mean local Sauter radius of parent drops, r_{32}, and the breakup frequency, ν:

$$w_{bu} = r_{32}\nu \tag{5.18}$$

How to determine ν will be shown in eq. 5.26.

5.1.2.3 Critical radius, breakup frequency

The critical (or maximum stable) radius is determined when disruptive hydrodynamic forces are balanced by capillary forces:

$$r_{cr} = We_{cr}\delta/\rho_g u_r^2 \tag{5.19}$$

where u_r is the relative between liquid and gas velocity, δ is the surface tension coefficient, We_{cr} is the critical Weber number, which can be taken of order one over a large interval of Ohnesorge numbers [99], [59]. In the paper, written in 1949 [100], Kolmogorov considered the stretched drop of insoluble liquid that was submerged in a turbulent flow. Using the Obuchov- Kolmogorov's scaling law for the velocity difference across a size when the surface tension force becomes significant, Kolmogorov introduced a critical size of produced droplets as:

$$r_{cr} = \frac{1}{2}\left(\frac{We_{cr}\delta}{\epsilon^{2/3}\rho_g}\right)^{3/5} \quad \texttt{if} \quad 2r >> \eta \tag{5.20}$$

$$r_{cr} = \frac{1}{2}\left(\frac{We_{cr}\delta\nu}{\epsilon\rho_g}\right)^{1/3} \quad \texttt{if} \quad 2r >> \eta \tag{5.21}$$

where ϵ is the mean viscous dissipation rate and ρ_g is density in the gas. An estimation of r_{cr} by using experimental data from [101] gives an enhanced magnitude of r_{cr} comparing to the measurements. In order to account for the inertia of liquid, namely for the density of the liquid ρ_l the expression 5.20 can be modified. Estimating the mean square of relative droplet-to-gas velocity by mean viscous dissipation and Stokes time scale [102],

$$\left\langle u_r^2 \right\rangle = \epsilon\tau_{st} \tag{5.22}$$

one yields a new expression for critical radius:

$$r_{cr} = \frac{36^{1/3}}{2}\left(\frac{We_{cr}\delta\nu}{\epsilon\rho_l}\right)^{1/3} \tag{5.23}$$

Using the experimental data from [101] water density, $1000kg/m^3$; gas viscosity, $1.5x10^{-5}m^2/s$; gas orifice size, $2.1mm$; surface tension, $0.07kg/s^2$; gas injection velocity, 140 m/s and by setting the turbulent gas velocity at one tenth of the gas injection velocity, one gives for critical radius $3x10^{-5}$ m, which is of the same order that was measured in [101]. At the same time, expressions 5.23 requires a reliable knowledge of viscous dissipation rate, which is a problem in the turbulence computation. For these reasons, the critical radius is calculated in this work by the standard expression 5.19, where $u_r = V_g - v_p$ is calculated by the mean relative velocity between gas and liquid particle, computed by the model of turbulent of particles. Note that introducing the turbulent Weber number, $We_{tur} = \rho_g l_{tur} u_{tur}^2/\delta$, and using 5.22, one may write for the critical Weber number:

$$We_{cr} = \frac{1}{36}\frac{\rho_l}{\rho_g} Re_{tur} We_{tur}\left(\frac{2r_{cr}}{l_{tur}}\right)^3 \tag{5.24}$$

Assuming that at scales where breakup takes place Re_{tur} (turbulent reynold's number) is of order of unity and the turbulent length scale $l_{tur} \approx \eta$, one may propose:

$$\frac{2r_{cr}}{\eta} = 3.3 \left(\frac{We_{\eta}}{We_{cr}}\right)^{-1/3} \left(\frac{\rho_g}{\rho_l}\right)^{1/3} \tag{5.25}$$

The choice of the breakup frequency has to be stated from the physics of atomization. In this work, the breakup time scale is

$$\nu = B\frac{|v_g - v_p|}{r_{32}}\sqrt{\frac{\rho_g}{\rho_l}} \tag{5.26}$$

where r_{32} is the local Sauter mean radius of parent drops and $B = 1/\sqrt{3}$ is taken from the TAB model [89].

5.1.2.4 Choice of parameters

Multiplying 5.14 by r and integrating over the entire r - range leads to an expression for the first moment

$$\langle r \rangle = \langle r \rangle_{t=0}\, exp \left\lfloor \nu(\langle \xi \rangle + 0.5 \langle \xi^2 \rangle)t \right\rfloor \tag{5.27}$$

The condition

$$\langle \xi \rangle < -\frac{1}{2}\langle \xi^2 \rangle \tag{5.28}$$

is provided for $\frac{\langle r \rangle}{\langle r \rangle_{t=0}}$. In this work, the magnitude for $\langle \xi^2 \rangle$ is supposed to be proportional to the maximal dispersion of radius $\langle \xi^2 \rangle \propto ln1 - ln\frac{r_{cr}}{r_{32}}$ Replacing in 5.25 η by the local Sauter mean diameter of parent drops, one may assume that

$$\langle \xi^2 \rangle \approx -ln\frac{r_{cr}}{r_{32}} \approx \text{const}ln\left(\frac{We_{r_{32}}}{We_{cr}}\right) \tag{5.29}$$

and $\langle \xi \rangle$ is an arbitrary parameter to be taken according to 5.28 and 5.29.

5.2 Turbulent Dispersion

The Eulerian approach for the fluid flow gives the mean values of the fluid velocity components and the turbulent quantities. However, the particle experiences at its position the instantaneous fluid velocity $\overrightarrow{u}$, which is stochastic. To account for the effect of this stochastic behavior of fluid flow on the particle, so called turbulent dispersion, a dispersion model is needed. Three dispersion models are used in this work to evaluate the instantaneous fluid velocity at the position of particle. They are (a) the particle Langevin model (PLM), (b) the isotropic Random Walk model (RWM-Iso) and (c) the anisotropic Random Walk model (RWM-Aniso).

5.2.1 Particle Langevin Model (PLM)

As pointed out above, this approach consists of generating directly the fluid velocities following the particle path by modeling the de-correlation induced by the mean and turbulent fluid-particle relative motion. An elaborated presentation of PLM is introduced by Minier et al. (2001). The fluid velocity fluctuation seen by particles emerges as follows:

$$du_i = -u_j \frac{\partial \overline{U}_i}{\partial x_j} dt + \frac{\partial \overline{u_i u_j}}{\partial x_j} dt + (\overline{U}_{pj} - \overline{U}_j) \frac{\partial \overline{U}_i}{\partial x_j} dt + \frac{1}{T_{Li}} H_{ij} u_i dt + B_{ij} \xi_i, \tag{5.30}$$

where $\bar{U}_i$ and $\overline{u_i u_j}$ are the mean velocity and the Reynolds stress tensor. Furthermore, H_{ij} is a generalization of the drift matrix for arbitrary mean slip between the flow phases, B_{ij} the diffusion matrix and ξ_i a Gaussian random process. T_{Li} represents the Lagrangian time scale and is defined as follows:

$$T_{Li} = \frac{1}{\left(\frac{1}{2} + \frac{3}{4} C_0\right) \frac{\epsilon}{k} b_i}. \tag{5.31}$$

In equation 5.31 ,$C_0 = 2.1$ and b_i are Csanady factors which are mostly used to estimate the difference between the stream wise and the transversal time scales. b_i is defined as below:

$$b_i = b_{|} + (b_{|} - b_{\perp}) \frac{(U_{pi} - U_i)^2}{\left| \overrightarrow{U_p} - \overrightarrow{U} \right|^2} \tag{5.32}$$

$$b_{|} = \left(1 + \beta^2 \frac{|\overrightarrow{U_p} - \overrightarrow{U}|^2}{2k/3} \right)^{0.5}, \qquad b_{\perp} = \left(1 + 4\beta^2 \frac{|\overrightarrow{U_p} - \overrightarrow{U}|^2}{2k/3} \right)^{0.5} \tag{5.33}$$

$\beta = \frac{T_L}{T_E} = \frac{1}{C_L}$ is the ratio between the Lagrangian time and Eulerian time scales. In this work the common value of $C_L = 1.1.$ is used (see Horender).
The matrix H_{ij} is defined in the following form:

$$H_{ij} = b_{\perp}\delta_{ij} + b_{|} r_i r_j, \tag{5.34}$$

where r_i is the unit vector in direction of the mean slip between fluid and particle.
The diffusion term (B_{ij}) is defined as:

$$(BB^T)_{ij} = D_{ij}, \tag{5.35}$$

where D_{ij} has the following form:

$$D_{ij} = \epsilon\left(C_0\lambda H_{ij} + \frac{2}{3}(\lambda H_{ij} - \delta_{ij})\right). \tag{5.36}$$

Further, λ is given by:

$$\lambda = \frac{3tr(H_{ij}R_{ij})}{2ktr(H_{ij})}, \tag{5.37}$$

where $tr(.)$ and R_{ij} denote the trace and the Reynolds stress tensor, respectively. Peirano et al. 2005 suggested a Simplified Langevin Model which takes into account the drift between the inertial particles and the fluid particles. The resulting equation for fluctuating velocity u_i is as follows:

$$du_i = \underbrace{-u_j\frac{\partial\overline{U}_i}{\partial x_j}dt + \frac{\partial\overline{u_iu_j}}{\partial x_j}dt}_{1} + \underbrace{(\overline{U}_{pj} - \overline{U}_i)\frac{\partial\overline{U}_i}{\partial x_j}}_{2} \tag{5.38}$$

$$\underbrace{-\frac{1}{T_{L,i}}u_idt}_{3} + \underbrace{\sqrt{\epsilon\left(\left(C_0 + \frac{2}{3}\right)b_i\frac{\widetilde{k}}{k} - \frac{2}{3}\right)}dW_i(t)}_{4}. \tag{5.39}$$

The first term is a fluid drift term. It accounts for the change of the fluctuation due to the changes of the fluid flow. Note that the Reynolds stresses are calculated following the standard $K - \epsilon$ model as follows:

$$R_{ij} = -\overline{u_iu_j} = \nu_t\left(\frac{\partial\overline{U}_i}{\partial x_j} + \frac{\partial\overline{U}_j}{\partial x_i}\right) - \frac{2}{3}k\delta_{ij} \tag{5.40}$$

The second term accounts for the drift between the particle and the mean fluid velocity field. The third term considers the memory effects. It relates the new fluctuating fluid velocity to the previous by the Lagrangian time scale $T_{L,i}$. The fourth term expresses the diffusion process by including randomness through the Wiener process $dW_i(t)$. The diffusion in different directions is assumed independent, but anisotropic Minier et al. 2001. $\widetilde{k}$ is a dimensionless turbulent kinetic energy defined by:

$$\widetilde{k} = \frac{3}{2} \frac{\sum_{i=1}^{3} b_i \overline{u_i^2}}{\sum_{i=1}^{3} b_i} \tag{5.41}$$

Note that henceforth the simplified version of Langevin equation will be referred as PLM and is used in the numerical simulations presented in this work.

5.2.2 Isotropic Random Walk Model (RWM-Iso)

In order to evaluate the capability of PLM, two simple models are considered for comparison. The first is the Lagrangian stochastic approach using the fluid turbulent variables (Sommerfeld et. al. [25]) (2003), [39] (1996), Sadiki et al. (2005), Chrigui et al. (2004), Melheim et al. (2005), Walklate (1995)). It is obtained from the discretized equations for a Markov-chain random-walk of fluid particle velocity fluctuations for homogeneous isotropic turbulence as:

$$u_{n+1,i} = R_{P,i}(\Delta t, \Delta r) u_{n,i} + \sigma_i \sqrt{1 - R_{P,i}^2(\Delta t, \Delta r) \xi_i(t_n)}. \tag{5.42}$$

Its solution for given initial conditions represents a Markov sequence of successive fluid particle velocity at time interval of Δt. Hence, this model can be seen as a Langevin model for an Orstein-Uhlenbeck process written in finite difference form. Hereafter it will be referred as isotropic Random Walk dispersion model (RWM-Iso).
In Eq. 5.42, $\xi_i(t_n)$ denotes a Gaussian random variable at time step t_n. Δr represents the spatial displacements during the time interval Δt and

$$R_{P,i}(\Delta t, \Delta r) = R_{L,i}(\Delta t) * R_{E,i}(\Delta r) \tag{5.43}$$

is a typical correlation used to compute the fluctuation of the fluid element u_i at the particle location. Thereby, the evolution of the fluid element velocity fluctuation along the stream line is determined using the Lagrangian correlation factor $R_{L,i}(\Delta t)$, while the fluid element velocity fluctuation located at the particle position is correlated with the fluid element location using the Eulerian correlation factor $R_{E,i}(\Delta r)$. They are expressed in Sommerfeld et. al. [25]) (2003), [39] (1996), Chrigui et al. (2004), Chrigui et al. (2010), Sadiki et al. (2005), Melheim et al. (2005) as:

$$R_{L,i}(\Delta t) = exp(-\frac{dt}{T_{Li}}) \tag{5.44}$$

$$R_{E,i}(\Delta t) = (f(\Delta r) - g(\Delta r)) \frac{\Delta r_i \Delta r_j}{\Delta r^2} + (\Delta r) g \delta_{ij}, \tag{5.45}$$

respectively. The quantity $T_{L,i}$ represents the Lagrangian integral time scale (see Eq. 5.32) calculated in the framework of $k-\epsilon$ turbulence model according to $T_{L,i}=c_T k/\epsilon=c_T\sigma^2/\epsilon$ with $c_T=0.3$ and $\sigma^2=k$. The longitudinal and transversal correlation functions $f(\Delta r)$ and $g(\Delta r)$ in Eq. 5.45 are computed using the following expressions:

$$f(\Delta r)=exp(-\frac{\Delta r}{L_E}); \qquad g(\Delta r)=(1-\frac{\Delta r}{2L_E})exp(-\frac{\Delta r}{L_E}) \tag{5.46}$$

where $L_E=c_L^{'}T_L\sigma$ (with $c_L^{'}=0.3$) represents the turbulent length scale.

5.2.3 Anisotropic Random Walk Model (RWM-Aniso)

To account for flow anisotropy and drift correction Legg & Raupach [50] extended the isotropic formulation of RWM-Iso by including an additional term, which is derived from the momentum equation (see Eq. 5.47). This term should consider the anisotropy of the flow and avoid non-physical behavior, such as the accumulation of particles in regions of low velocity variance. Eq. 5.42 then reads:

$$\begin{aligned}u_{n+1,i}=&R_{P,i}(\Delta t,\Delta r)u_{n,i}+\sigma_i\sqrt{1-R^2_{P,i}(\Delta t,\Delta r)\xi_i(t_n)}\\&+(1-R_{P,i}(\Delta t,\Delta r))T_{L,i}\frac{\partial\overline{u_iu_i}}{\partial x_i}\end{aligned} \tag{5.47}$$

It should here be noted that this model has been derived for a stationary, horizontally homogeneous flow over a flat plate. Therefore, it does not have the capability to deal properly with the three dimensionality nature of turbulence in complex flows.

5.3 Evaporation

In many devices, as it is in cases investigated in this work, fuels are sprayed as fine droplets into a combustion chamber. The droplets undergo evaporation, so that the evaporation represents a decisive process of the fuel preparation in such devices. Numerous theoretical studies literature have been carried out for the description of droplet evaporation. In the most general case the droplet evaporation process includes two main phases: (1) detachment of fuel molecules from the surface of the droplet into gas in the immediate vicinity of droplets (evaporation proper) and (2) diffusion of fuel vapor from the surface of the droplet into the ambient gas. The mathematical modeling of the first process is far more complicated than the modeling of the second process. Hence, in most practical application, the researchers tried to focus just on the second process, ignoring the details of the first. The models, which they used were based on the assumption that fuel vapor in the vicinity of the droplet surface is always saturated. Hence, the rate of fuel evaporation is equal to the rate of fuel diffusion from the droplet surface to ambient gas. These are known as the hydrodynamic models of droplet evaporation. In contrast to these, models taking into account the details of detachment of fuel molecules are known as kinetic models (if they are based on modeling

of the dynamics of individual molecules).
Empirical correlations also exist, which are not directly linked with any physical evaporation model In this section the evaporation model, the so-called uniform temperature model by Abramson and Sirignano [109] used in the frame of this thesis, will be introduced.

5.3.1 Abramzon and Sirignano model: Uniform temperature model

This model represents an equilibrium evaporation model based on the film thickness theory. Accordingly, two time scales characterizing the turbulence and the thermodynamics of the vaporization will be introduced along with a new dimensionless number to characterize the turbulence droplet vaporization interaction regimes. In order to ensure a mathematical description, one should reduce the complexity of the theoretical description. Thus the following basic assumptions and simplifications are made according to [42]:

1. One component model is considered, so that one solely deals with the so-called infinite conductivity model.
2. Droplets are assumed to be spherical.
3. Secondary atomization and coalescence of droplets are neglected as the evaporation process is only accounted for in the we concentrate on the dilute spray region. In other words simple elastic collisions between droplets and wall are assumed without any kind of film formation [148].
4. The influence of the surface tension is neglected and assume a uniform pressure around the droplet is assumed.
5. Uniform physical properties of the surrounding fluid and liquid-vapor thermal equilibrium on the droplet surface are assumed.
6. The ambient air is not soluble in the droplet fluid.
7. Chemical reactions and radiation are not considered.

In order to further simplify the modeling of the evaporation process, the evaporation process is subdivided into three spatial zones (Figure 5.1):

1. The ambient gas phase, which represents the region infinitely far from the droplet. The temperature and vapor concentration are those of the carrier phase.
2. The droplet interior
3. The liquid/gas interface, which represents the region governing transport processes. In this region one observes radial mass diffusion, heat convection and conduction as well as forced convection.

The transport processes linked to the forced convection from the gas flow around the droplet, (located at the liquid/gas interface as presented above), is the fundamental difficulty in the development of practical evaporation models. For solving this problem, one has to start from an isolated droplet in a stagnant gas atmosphere with spherical symmetric transport of mass and energy. The effect of forced convection is then taken into account by means of empirical correlation factors (modified Nusselt and Sherwood numbers), as they will be introduced later on.

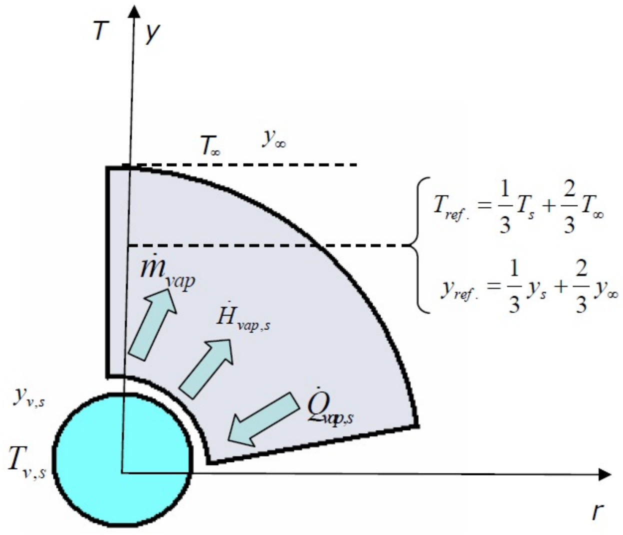

Figure 5.1: schematic description of evaporation [23]

The Uniform Temperature model (UT model) as it is used in the frame of this work (UT model) does not consider any temperature variation in the interior of the droplet (homogenous temperature). However, the temperature variation has an unsteady behavior and is accompanied with mass transfer [69]. As this model does not account for the gradient at the interior of the droplet, droplets are not discretized. Therefore this model does not require high computing time. The UT model describes the evolution of the droplet temperature and diameter, i.e. evaporation rate and energy flux through the liquid/gas interface in figure 5.1. The vaporization rate is calculated by considering the mass transfer around the droplet following [70]:

$$\dot{m}_{p,v} = 2\pi r_p \bar{\rho_m} \bar{D_m} Sh^* \frac{ln(1+B_M)}{B_M} \tag{5.48}$$

where r_p is the droplet radius, $\bar{\rho_m}$ and $\bar{D_m}$ are the averaged values of the mixture density and binary diffusion coefficient throughout the film, respectively. B_m represents the Spalding's mass transfer number defined by

$$B_M = \frac{y_s - y_\infty}{1 - y_s} \tag{5.49}$$

in which y_s is the surface vapor mass fraction and y_∞ is the vapor mass fraction far from the droplet. In particular y_s depends on the vapor relative pressure which itself depends on the droplet surface temperature.

$$y_s = \frac{\nu_{s,eq}}{\nu_{s,eq} - (1 - \nu_{s,eq})\theta_2} \tag{5.50}$$

where θ_2 is the ratio of molecular weights. The molar mass fraction $\nu_{s,eq}$ is related to the saturation pressure through the Clausius-Clapeyron equation. Therefore it is referred to as an equilibrium based model. The accuracy of the evaporation rate depends strongly on the determination of the values of ,$\bar{\rho_m}$ and $\bar{D_m}$. Physical properties of the air vapor mixture (in the gaseous film around the droplet) are determined using the reference temperature and mass fraction. They are calculated using the Simpson or Sparrow & Gregg '1/3' rule [71], from which the best accuracy of these quantities have been obtained (see 5.1). The droplet radius is obtained from the equation of the diameter evolution for each droplet by:

$$\frac{dD_p}{dt} = -\frac{2\dot{m}_{p,v}}{\pi\rho_L D_p^2} - \frac{D_p}{3\rho_L}\frac{\partial\rho_L}{\partial T_p}\frac{dT_p}{dt}, \tag{5.51}$$

where ρ_L is the liquid density, D_p the droplet diameter and T_p the droplet temperature. Effects of convection on the vaporization and the heat flux rate are taken into account by means of semi-empirical correlations such as those for the drag coefficient, the Sherwood number and the Nusselt number. The quantity Sh^* denotes the modified Sherwood number which includes the effects of the Stefan flow. It is defined by

$$Sh^* = 2 + \frac{Sh_o - 2}{F_M} \tag{5.52}$$

where

$$Sh_0 = 1 + (1 + Re_p Sc_p)^{1/3} f(Re_p) \tag{5.53}$$

Sh_0 accounts for the bulk convection of a non-evaporating spherical droplet. Re_p is the droplet Reynolds number and Sc_p is the Schmidt number while $f(Re_p)$ is an empirical function defined as $f(Re_p) = Re_p^{0.77}$ and F_M is a correction factor, which takes into consideration the relative change of the mass film thickness due to the droplet evaporation process:

$$F_M = F_M(B_M) = (1 + B_M)^{0.7} ln\frac{(1 + B_M)}{B_M} \tag{5.54}$$

The evaporation is coupled with the droplet energy/heating in 5.51 where the droplet temperature variation is described by

$$\frac{dT_p}{dt} = -\frac{6\dot{Q}_l}{\rho\pi c_{pL} D_p^3}, \tag{5.55}$$

where c_{pL} denotes the heat capacity coefficient of the liquid and $\dot{Q}_l$ the heat flux rate penetrating into the droplet. The latter is calculated similarly to the evaporation rate and related to it by:

$$\dot{Q}_l = \dot{m}_{p,v} \left[\frac{c_{pm}(T_\infty - T_p)}{B_T} - h_v(T_p) \right], \tag{5.56}$$

where $h_v(T_p) = r(T_p) + \dot{Q}_l/\dot{m}_{p,v}$ expresses the effective latent heat of vaporization. It is a function of temperature and varies with the considered liquid. $r(T_p)$ is the true latent heat of vaporization and B_T is the Spalding heat transfer number expressed by

$$B_T = \frac{c_{p,v}(T_\infty^{-} - T_p)}{r(T_p) + \dot{Q}_l/\dot{m}_{p,v}}, \tag{5.57}$$

It is related to the mass transfer number B_M by

$$B_M = (1 + B_M)^{\phi} - 1, \tag{5.58}$$

where

$$\phi = \frac{c_{p,v}}{c_{p,m}} \frac{Sh^*}{Nu^*} \frac{1}{Le}. \tag{5.59}$$

The variable ϕ depends on the thermo-physical properties, the Lewis number Le and the modified Sherwood and Nusselt numbers (Sh^* and Nu^*). The modified Nusselt number in 5.59 is defined by:

$$Nu^* = 2 + \frac{Nu_0 - 2}{F_T}, \tag{5.60}$$

where

$$Nu_0 = 1 + (1 + Re_p Pr)^{1/3} f(Re_p). \tag{5.61}$$

Nu_0 expresses the Nusselt number for a non-evaporating spherical droplet with $f(Re_p)$ as defined above. Pr is the Prandtl number and F_T is a correction factor which accounts for the change of the temperature within the film thickness due to the droplet evaporation process:

$$F_T = F_T(B_T) = (1 + B_T)^{0.7} ln \frac{(1 + B_T)}{B_T}. \tag{5.62}$$

In 5.59 c_{pv} and c_{pm} are the heat capacity coefficients of vapor and mixture, respectively. Between Nu_0 and the modified Nusselt numbers Nu^* the relationship 5.61 is considered. No correction to the drag coefficient due to the evaporation process has been taken into consideration. The gas viscosity in the droplet Reynolds number near the droplet has been estimated at a well-defined reference state of temperature and vapor mass fraction according to the averaging '1/3 rule' [107].

6 Numerical procedure

The development and analysis of discretization methods for systems of ordinary and partial differential equations and the implementation of the respective algorithms in computer codes are the only way to transform the theoretical work into practical one which can provide useable results. The challenge is then shifted from the continuous mathematics to discrete mathematics. This section deals with the used numerical procedure to discretize the governing equations for the carrier phase, the dispersed phase and the coupling method between both phases. The statistical method for properties sampling and the convergence criteria will be also introduced later.

6.1 Solution procedure of the transport equations for the continuous phase

Following Ferziger and Peri [72], a numerical solution method includes a mathematical model, a discretization method, a coordinate and basis vector system, a numerical grid, a finite approximation and a solution method. In this work the CFD package FASTEST-3D (Flow Analysis Solving Transport Equations Simulating Turbulence 3 Dimensional) is used. The program was originally developed by INVENT Computing GmbH (Erlangen, Germany) and obtained as a source code in the framework of the Collaborative Research Project SFB-568. Consequently, the parts of numerical solution method mentioned above and applied in the present work are those based on the features of FASTEST-3D:

1. Finite volume discretization method (FVM) based on hexahedral control volumes;
2. Cartesian coordinate and basis vector system;
3. Boundary-fitted non-orthogonal block-structured grid with matching interfaces and collocated variable arrangement;
4. Implicit and semi-implicit temporal and first and second order spatial discretization schemes;
5. Strongly implicit procedure for the solution (iterative) of the linearised equation system;
6. Full geometrical multigrid solver for the acceleration of convergence;
7. Parallelization based on domain decomposition in space using the MPI message passing library.

Important details as well as implementation of the boundary conditions will be presented and discussed in the following sections.

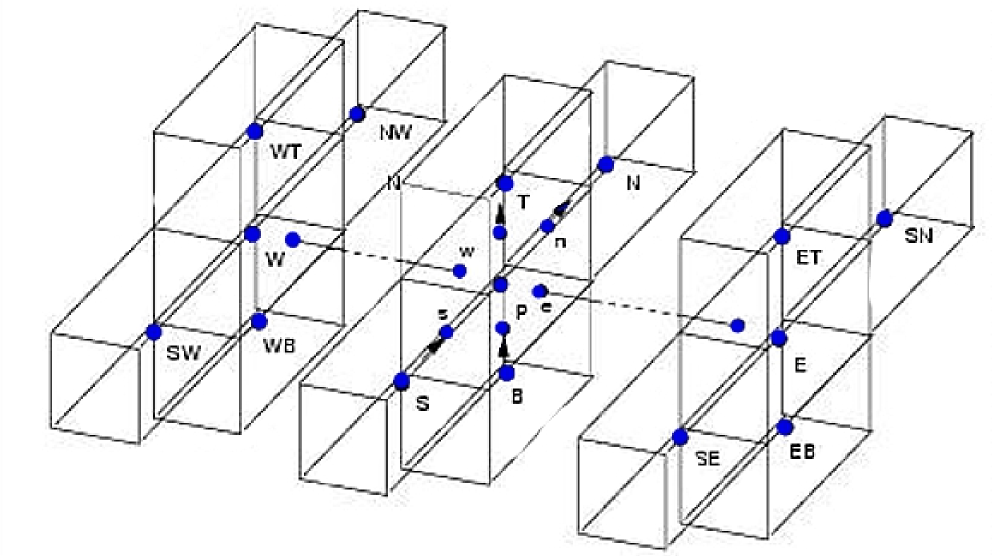

Figure 6.1: Topology and control volume notification

6.1.1 Finite volume method

The finite volume method is used in the frame of this work to describe the continuous phase. This method is based on the resolution of governing equations in the integral form given by the equation 6.1:

$$\int_V \frac{\partial}{\partial t}(\rho\psi)dV + \int_V \frac{\partial}{\partial x_i}(\rho u_i \psi)dV = \int_V \frac{\partial}{\partial x_i}\left(\Gamma_\psi \frac{\partial \psi}{\partial x_i}\right) dV + \int_V S_\psi dV \tag{6.1}$$

The quantity ψ is a conserved variable (velocity component, scalar, etc.), Γ_ψ notes the diffusivity coefficient, S_ψ the sum of all source terms and V the volume of the considered cell. The volume integrals are transformed to area integrals using Gauss' Law:

$$\int_V \frac{\partial}{\partial t}(\rho\psi)dV + \int_\sigma \left(\rho u_i \psi - \Gamma_\psi \frac{\partial \psi}{\partial x_i}\right) n_i d\sigma = \int_V S_\psi dV, \tag{6.2}$$

where σ represents the surface confining the volume V (of the cell) and n_i the unit vector normal to the surface σ. Equation 6.8 is applied for every control volume (CV) of the numerical grid which defines the computational domain where the discrete locations at which the variables are to be calculated (Figure 6.1). The storage of the flow information which are related to every CV divides the discretization problem into two different arrangements, namely: collocated grid and staggered grid.

Collocated grid, as used in this work, is one in which the pressure and velocity variables share the same grid (Figure 6.2). Thus all variables are stored on the same grid point and the same control volume is used for all variables. It is the preferred method for non-orthogonal coordinates. The

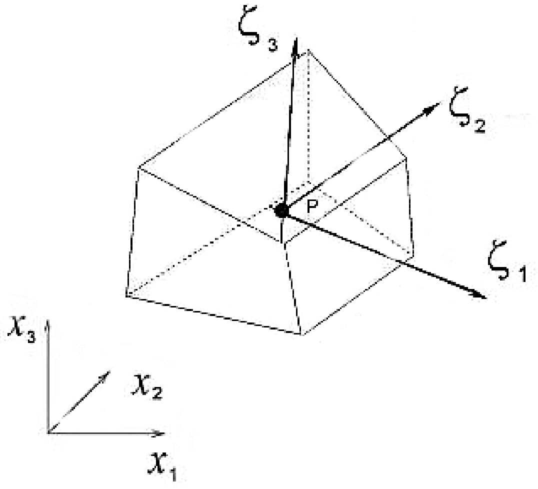

Figure 6.2: Collocated grid

implementations of collocated grids on non-orthogonal coordinates need regularization to avoide the formation of oscillations because of pressure velocity decoupling [72].

Staggered grid: The scalar variables (pressure, density, total enthalpy, scalar, etc.) are stored in the center of the grid, whereas the normal components of the momentum (velocity) are located at the midpoints of the cell faces (Figure 6.2). Using a staggered grid is the most common way to avoid the pressure-velocity decoupling and thus avoid pressure oscillations [72].

Let us now consider a hexahedral control volume with central point denoted as P, having six neighbors CVs: E (east), W (west), N (north), S (south), T (top) and B (bottom) (see Figure 6.1) which are sharing common faces with neighbors: e, w, n, s, t and b, respectively. The final objective within finite volume method is to transform the integral differential equation (6.8) into an algebraic equation of the following form:

$$\underbrace{A_p \psi_p - \sum_{Nb} A_{Nb} \psi_{Nb}}_{implicitpart} = \underbrace{S_p}_{explicitpart} \tag{6.3}$$

Here, the subscript Nb conforms to the 6 neighbors CVs: W, E, S, N, B, T and A_p , A_{Nb} denote the coefficients which belong to the dependent variable values ψ_p, ψ_{Nb} in the point P, Nb derived from the discretization. All the remaining terms resulting from the discretization that cannot be included into the implicit part of 6.3 are treated explicitly and put into the source term S_p on the RHS.

6.1.2 Coordinate transformation

If we take into account the non-orthogonality of the grid used, it will be plausible to use in each CV and on each CV face a local coordinate system and then transform the operators from local into

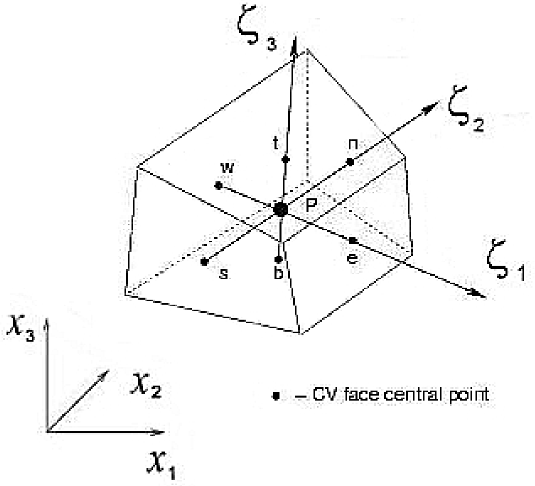

Figure 6.3: Variables arrangement on staggered grid

the global (Cartesian) coordinate system. In Figure 6.4 a local coordinate system located in the CV central point is shown. The basis vectors of the local coordinate system are obtained connecting the CV central point with the central points of the CV's faces.

The local coordinates are in the following indicated as (ξ_1, ξ_2, ξ_3) while global (Cartesian) coordinates are denoted as (x_1, x_2, x_3). The transformation matrix (for transformation from the global into the local coordinate system) is

$$A = \begin{vmatrix} \frac{\partial x_1}{\partial \xi_1} & \frac{\partial x_1}{\partial \xi_2} & \frac{\partial x_1}{\partial \xi_3} \\ \frac{\partial x_2}{\partial \xi_1} & \frac{\partial x_2}{\partial \xi_2} & \frac{\partial x_3}{\partial \xi_3} \\ \frac{\partial x_3}{\partial \xi_1} & \frac{\partial x_3}{\partial \xi_2} & \frac{\partial x_3}{\partial \xi_3} \end{vmatrix}.$$

The derivative of some field variable ψ with respect to Cartesian coordinates can be expressed in terms of the local coordinates according to

$$\frac{\partial \psi}{\partial x_i} = \frac{\partial \psi}{\partial \xi_i}\frac{\partial \xi_i}{\partial x_i}. \tag{6.4}$$

The elements of the inverse transformation matrix, A^{-1}, (local to global),

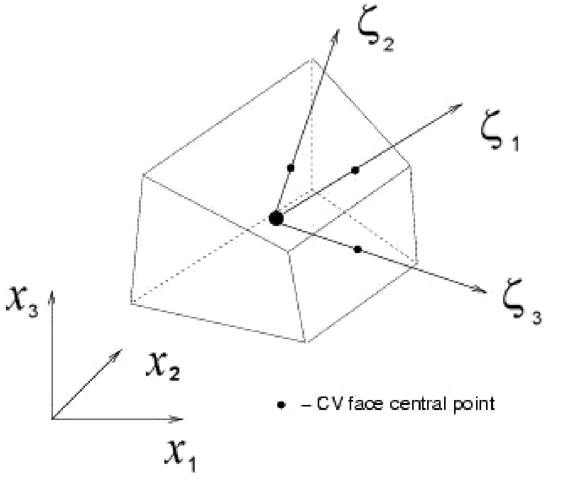

Figure 6.4: Local coordinate system arranged in the CV central

$$A^{-1} = \begin{vmatrix} \frac{\partial \xi_1}{\partial x_1} & \frac{\partial \xi_1}{\partial x_2} & \frac{\partial \xi_1}{\partial x_3} \\ \frac{\partial \xi_2}{\partial x_1} & \frac{\partial \xi_2}{\partial x_2} & \frac{\partial \xi_2}{\partial x_3} \\ \frac{\partial \xi_3}{\partial x_1} & \frac{\partial \xi_3}{\partial x_2} & \frac{\partial \xi_3}{\partial x_3} \end{vmatrix}.$$

are obtained from the well-known linear algebraic relation:

$$A^{-1} = \frac{1}{J}(A_{adj})^T, \tag{6.5}$$

where $J = det(A)$ is the Jacobean and $(adjA)$ is the transpose adjoint matrix obtained from matrix A . I.e.

$$\frac{\partial \xi_j}{\partial x_j} = \frac{1}{J}\left[adj\left(\frac{\partial x_j}{\partial}\xi_j\right)\right]^T = \frac{1}{J}B_{ij} \tag{6.6}$$

where B_{ij} is the element of matrix B given by

$$A = \begin{vmatrix} \frac{\partial x_2}{\partial \xi_2}\frac{\partial x_3}{\partial \xi_3} - \frac{\partial x_2}{\partial \xi_3}\frac{\partial x_3}{\partial \xi_2} & \frac{\partial x_1}{\partial \xi_3}\frac{\partial x_3}{\partial \xi_2} - \frac{\partial x_1}{\partial \xi_2}\frac{\partial x_3}{\partial \xi_3} & \frac{\partial x_1}{\partial \xi_2}\frac{\partial x_2}{\partial \xi_3} - \frac{\partial x_1}{\partial \xi_3}\frac{\partial x_2}{\partial \xi_2} \\ \frac{\partial x_2}{\partial \xi_3}\frac{\partial x_3}{\partial \xi_1} - \frac{\partial x_2}{\partial \xi_1}\frac{\partial x_3}{\partial \xi_3} & \frac{\partial x_1}{\partial \xi_1}\frac{\partial x_3}{\partial \xi_3} - \frac{\partial x_1}{\partial \xi_3}\frac{\partial x_3}{\partial \xi_1} & \frac{\partial x_1}{\partial \xi_3}\frac{\partial x_2}{\partial \xi_1} - \frac{\partial x_1}{\partial \xi_1}\frac{\partial x_2}{\partial \xi_3} \\ \frac{\partial x_2}{\partial \xi_1}\frac{\partial x_3}{\partial \xi_2} - \frac{\partial x_2}{\partial \xi_2}\frac{\partial x_3}{\partial \xi_1} & \frac{\partial x_1}{\partial \xi_2}\frac{\partial x_3}{\partial \xi_1} - \frac{\partial x_1}{\partial \xi_1}\frac{\partial x_3}{\partial \xi_2} & \frac{\partial x_1}{\partial \xi_1}\frac{\partial x_2}{\partial \xi_2} - \frac{\partial x_1}{\partial \xi_2}\frac{\partial x_2}{\partial \xi_1} \end{vmatrix}.$$

Substitution of the expression for the differential operator 6.6 into equation 6.8 gives

$$\int_V \frac{\partial}{\partial t}(\rho\psi)dV + \int_\sigma \left(\rho u_i \psi - \Gamma_\psi \frac{\partial \psi}{\partial x_i}\right) n_i d\sigma = \int_V S_\psi dV, \tag{6.7}$$

6.1.3 Discretization of the convective and diffusion terms

The discretization of the convective terms is given by:

$$\int_\sigma \rho u_i \psi n_i d\sigma = \sum_{k=e,w,n,x} a_k \sigma_k = (\rho u\psi)_e \sigma_e - (\rho u\psi)_w \sigma_w + (\rho u\psi)_n \sigma_n \tag{6.8}$$

$$-(\rho u\psi)_s \sigma_s + (\rho u\psi)_t \sigma_t - (\rho u\psi)_b \sigma_b$$

The problem now is how to approximate the value ψ at the faces e, w, n s, t and b. There are three basic discretization schemes.

The first common way is to use linear interpolation **Central Differencing Scheme (CDS)**. The value of ψ (e.g. at the east face) is estimated using the neighbor's nodes P and E (Figure 6.1).

$$\psi_e = f_x \psi_E + (1 + f_x)\psi_P, \tag{6.9}$$

where f_x is the interpolation function, and for a constant mesh spacing $f_x = 0.5$. The central differencing scheme has a second order accuracy. One can prove this by applying the Taylor series expansion on the point P. The accuracy is proportional to the square of grid width. I.e. if the number of cells within one direction is doubled, the error will be divided by a factor of 4.

The Upwind Differencing Scheme (UDS) assumes that the neighboring cell value for ψ will be convicted across the boundary:

$$\psi_e = \begin{cases} \psi_p & \text{if} \quad u_e \geq 0 \\ \psi_E & \text{if} \quad u_e < 0 \end{cases} \tag{6.10}$$

The main drawback of the upwind scheme is that it is inaccurate and very diffusive because of its first order.

The Flux Blending switches between the two, according to the relative size of the convective and diffusive fluxes across the cell face. By resulting in oscillation, one can combine UDC and CDS to calculate the value at the faces e:

$$\psi_e = \underbrace{\psi_e^{UDS}}_{I} + \underbrace{\gamma(\psi_e^{CDS} - \psi_e^{CDS})}_{II}, \tag{6.11}$$

where $0 \leq \gamma \leq 1$ is a factor which scales the manner of flux blending. For $\gamma = 1$, the interpolation is pure CDS whereas for $\gamma = 1$, the interpolation is pure Upwind. Part I of 6.11 is treated implicitly whereas part II is treated explicitly. The flux blending scheme is a good control tool to achieve an optimum between stability and accuracy. For the diffusive part, a centered difference for the discretization of the normal gradient of the flux on the control volumes faces is used. Thus the diffusive part is discretized by:

$$\left(\frac{\partial\psi}{\partial x}\right)_e = \frac{\psi_E - \psi_P}{x_E - x_P} \tag{6.12}$$

In the frame of this work, all above mentioned schemes for the interpolation of scalar (e.g. ψ_E) at the control volume faces have been applied on different configurations. These numerical schemes reflect the way how information is transported through the faces. It is dependent on the ratio between convection and diffusion, i.e. the Peclet number, which is defined by:

$$Pe = \frac{\rho u_i \partial x_i}{\Gamma} \tag{6.13}$$

If the Peclet number is small, the transport is dominated by diffusion, which transports information equally in all directions. Contrarily if the Peclet number is large, information is transported in the direction of the velocity field. Having a large Pe is undesired, since it influences the solution convergence very much. The numerical results may contain oscillations due to the fact that while computing the convective term at the note P only the values at E (east) and W (west) nodes are used, but not at the P node. Thus, ψ_P can take any value, i.e. oscillations are allowed.

Other than CDS, UDS, and the flux blending schemes there is a large number of interpolation methods, e.g. Quadratic Upwind Interpolation for Convective Kinematics ”QUICK”, which is third accurate order. Unfortunately it was not used within this work. A recent review on numerical schemes and their performance can be found in [73] and [72].

6.1.4 Time dependent discretization

Unsteady flows have a fourth coordinate direction as time, which must be discretized. The implemented time discretizations within the used code are: First Order Forward Implicit (FOFI), Second Order Forward Implicit (SOFI), Crank Nicolson (CN), and Runge Kutta (RK) [72] methods. The last one (RK) is an explicit method, i.e. there is only one unknown in the discretized equation time level (equation (4.18) for one dimensional convective diffusive problem).

$$\frac{\psi_P^{n+1} - \psi_P^n}{\partial t} + u\frac{\psi_P^n - \psi_W^n}{2\partial x} - \Gamma\frac{\psi_P^n - \psi_W^n - 2{\psi_P^n}^2}{\partial x} = 0. \tag{6.14}$$

From this equation, one can define the CFL number. Thus one can also make an instruction for the explicit time discretization method which is valid for RK-method:

$$CFL = \left| u\frac{\partial t}{\partial x} \right| \leq 1, \tag{6.15}$$

this requires:

$$\partial t \leq \frac{\partial x}{u}. \tag{6.16}$$

The FOFI method (also known as implicit Euler method) is applied by discretizing the variable in the time level n+1 as follows:

$$\frac{\partial \psi(t_{n+1})}{\partial t} \approx \frac{\psi^{n+1} - \psi^n}{\partial t_n} = f(\psi^{n+1}) \tag{6.17}$$

For the computed time dependent configuration in this thesis, the FOFI method was chosen. The advantage of using this scheme (fully-implicit technique) is that there is no restriction on time-steps (the implicit Euler method allows arbitrarily large time steps to be taken). However the first order implicit method is no more accurate than the explicit Euler method [72]. The disadvantage is the first order truncation error in time.

The Crank-Nicolson method solves both the accuracy and the stability problem. It is based on central differencing and hence it is second-order accurate in time. The approximation of the time derivative is done on the time point $t_{n+1/2}$ as follows:

$$\frac{\partial \psi(t_{n+1})}{\partial t} \approx \frac{\psi^{n+1} - \psi^n}{\partial t_n} = \left[f(\psi^{n+1}) + f(\psi^n) \right] \tag{6.18}$$

6.1.5 Pressure velocity coupling

The 3D-incompressible flow is described numerically by three equations of momentum and the continuity. Thus we have four unknowns (u, v, w, and P) and four equations (3 for momentum + 1 for continuity). One should mention here, that the density ρ is not considered as variable, because the flow is incompressible. In other words, the density may change due to variations in temperature and concentration of species, but not due to pressure variations $(\partial\rho/\partial p = 0)$. The problem is that we do not have any equation for pressure P. In case of compressible flow, i.e. Mach number > 0.3, the pressure is deduced by the equation of state. Unfortunately, the flows under investigation are incompressible. Therefore we can use the continuity equation as an indirect equation for the pressure. This method is called the SIMPLE (Semi Implicit Method for Pressure Linked Equation) algorithm.

The SIMPLE algorithm is preceded as follows: first the momentum equations are solved, using an ”old” pressure to give u^* , v^* , and w^*. In the following we are going to consider only the x-direction with the velocity component u^* , the other two directions can be treated in the same way. The discretized governing equation (4.3) for the u^* velocity component is given by:

$$a_e u_e^* = \sum_{nb} a_{nb} u_{nb}^* + S_{\tilde{u}} + (P_W^* P_P^*)\sigma_e, \tag{6.19}$$

where $S_{\tilde{u}}$ represents a source term, σ_e the control volume surface in the east face and a_{nb} are the discretization coefficients related to all faces. Now we introduce:

$$u_i^{n+1} = u_i^* + u_i^{cor} \tag{6.20}$$

$$P^{n+1} = P^* + P^{cor} \tag{6.21}$$

where u_i^* have been obtained from the momentum equations, and p^* was obtained from the previous iteration. u_i^{cor} and P^{cor} are the velocity and pressure correction respectively. Now, velocities u_i^{n+1} are used (corrected) to solve the continuity equation

$$\sum_i (\rho u^{n+1} \sigma)_i = 0 \tag{6.22}$$

Then we use the momentum equations to obtain a relation between u_i^{n+1} and P^{cor} .

$$a_e u_e^{n+1} = \sum_{nb} a_{nb} u_{nb}^{n+1} + S_u + (P_W^{n+1} - P_P^{n+1})\sigma_e, \tag{6.23}$$

where nb denotes the neighboring faces. The equation 6.23 provides a relation between u_i^{cor} and P^cor as follows:

$$a_P u_P^{cor} = \sum_{nb} a_{nb} u_{nb}^{cor} + (P_W^{cor} - P_P^{cor})\sigma_e, \tag{6.24}$$

Equation 6.24 necessitates the determination of pcor to calculate the corrected velocities. So we use equation 6.22 and deduce the following expression:

$$a_P P_P^{cor} = \sum_{nb} a_{nb} P_{nb}^{cor} - \underbrace{\sum_{nb} (\rho u_i^* \sigma_i)}_{\acute{b}} \tag{6.25}$$

The object of the pressure correction equation is to satisfy the continuity equation, i.e. to make the term $\acute{b}$ in equation6.25 vanish and thus determine $P^c or$. Once $(P_W^{cor} - P_P^{cor})$ is calculated, we can compute the new velocities as follows:

$$u_e^{n+1} = u_e^* - \frac{\sigma_e}{a_e - \sum_{nb} a_{nb}} P_W^{cor} - P_P^{cor} \tag{6.26}$$

The equation 6.26 includes the term $\sum_{nb} a_{nb}$, which is unknown and therefore it will be set to zero in the frame of the SIMPLE method [73]. Other pressure correction method (SIMPLEC) assumes that $\sum_{nb} a_{nb} u_{nb}^{cor} = \sum_{nb} a_{nb} u_e^{cor}$ in 6.24 to get the equation 6.26.

The solution procedure using the SIMPLE method can be summarized as follows:

- Guess the pressure p^* (or take it from previous step)
- Solve the Navier-Stokes equations and get u_i^*
- Solve the pressure correction p^{cor} (equation 6.25)
- Correct the velocities and pressure (equations 6.20 and 6.26)
- Repeat Steps 2-4 till convergence.

6.1.6 Boundary conditions

In view of a good representation of a physical system beside the mathematical model and the numerical scheme, properly chosen boundary conditions are of great importance. The imposition of exact boundary and initial conditions is necessary for a unique solution of the underlying partial differential equations [72]. The boundary conditions are those which are imposed by nature and must be satisfied by every Navier-Stokes fluid. They are at the inlet, outlet, wall, symmetry and periodicity limit. For transient problems, the initial conditions are also to be defined at the time point $t_0 = 0s$.

6.1.7 Inlet boundary conditions

The inlet boundary conditions for the velocity components (momentum) as well as other scalar variables like temperature and concentration are set by means of Dirichlet. Turbulent quantities, such as k, Reynolds stress components and ϵ are normally not known. But they must be estimated or they are measured experimentally. The dissipation is set from the equation [72]:

$$\tilde{\epsilon} = C_{\mu}^{3/4} \frac{\tilde{k}^{3/2}}{L}. \tag{6.27}$$

Based on isotropic turbulence, L represents a characteristic length scale, often set to 10% of the inlet dimension.

6.1.8 Wall boundary conditions

Mean velocity components

The solid boundary conditions used in the code are the von Neumann zero gradient scalars (mixture fraction, variance of mixture fraction, mass fraction). The velocities in grid nodes conjoined with the wall are set equal to the wall movement. In the frame of this work they are set to zero in the tangential as well as in the normal direction, because the wall is fixed (equation 6.28). This condition is also valid for all turbulent quantities.

$$\tilde{u_i}|_{wall} n_i = 0 \tag{6.28}$$

$$\tilde{u_i}|_{wall} t_i = 0 \tag{6.29}$$

In the near wall region a boundary layer is formed and the velocity profile slowly increases until it reaches the outer flow velocity. In order to capture this damping effect, wall functions are applied for the velocity components, the turbulent kinetic energy, Reynolds stress components, and the dissipation rate. For finer grids, the cell height in the region near the wall is sufficiently small that wall functions are not necessary to represent the distributions of velocity, turbulence, energy etc. within the boundary layer that forms adjacent to the hull surface. However, due to large grids and long computing times necessary, it is not practical to use the mesh refining method. The wall function, therefore, prescribes a logarithmic velocity profile within the boundary layer as:

$$U^{+} = \frac{1}{\kappa} ln \underbrace{\frac{u_{\tau} y_w}{\nu}}_{y^{+}} + B, \tag{6.30}$$

where U^{+} represents a dimensionless velocity defined as function of velocity tangential to the wall u_{τ} and the so called dynamic or friction velocity u_{τ} which is calculated as:

$$U^{+} = \frac{\tilde{u}_t}{u_{\tau}} \tag{6.31}$$

$$u_\tau = \sqrt{\frac{\tau_w}{\bar{\rho}}} = C_\mu^{1/4}\sqrt{\tilde{k}} \tag{6.32}$$

The variable y^+ in equation 6.30 values provide information whether wall functions should be used or not. Generally a limit for $y^+ < 11.63$ is considered for which the wall function method is not applied, otherwise wall functions are used for resolving the boundary layer. ê in equation 6.30 represents the Karman constant and is equal to 0.41, whereas B notes an empirical constant set to 5.2. In the viscous sublayer ($y^+ < 11.63$) the velocity $U^+ = y^+$.

Turbulent kinetic energy

In a turbulent boundary layer the turbulent production and dissipation are presumed to be in local equilibrium:

$$\underbrace{P_k}_{production} = \underbrace{\bar{\rho}\epsilon}_{dissipation} , \tag{6.33}$$

where the production term in the k -transport equation in a fully developed boundary layer is given by:

$$P_k = -\bar{\rho}\tau_{12}^L \frac{\partial \tilde{u}_t}{\partial \xi_2} \tag{6.34}$$

The variable τ_{12}^L denotes the local tangential Reynolds stress component in a fully developed turbulent boundary layer. In the viscous sublayer the flow is actually laminar and no turbulent production is present. Strictly speaking the turbulent kinetic energy must be set to zero in this region. On the other hand this can cause problems in the numerical solution resulting in discontinuous distributions of k in the near-wall cells. There is, however, another term, that dominates in the viscous sublayer and be taken instead of turbulent production, namely

$$\frac{\partial}{\partial \xi_2}\left(\mu \frac{\partial k}{\partial \xi_2}\right). \tag{6.35}$$

The fact that k itself is zero in the viscous sublayer does not force the spatial derivative of k in the wall normal direction to be zero, too. Thus the turbulent production can be replaced by the molecular diffusion of k and the general form of the production term can be rewritten:

$$P_k = \tau_w \frac{\partial \tilde{u}_t}{\partial \xi_2}, \tag{6.36}$$

Two different formulations of the wall shear stress τ_w and mean velocity gradient (one for viscous sublayer and the other for the fully developed turbulent layer) are necessary. Following formulations can be derived:

1. Viscous sublayer: The wall shear stress is given by

$$\tau_w = \bar{\rho} u_\tau^2 = -\mu \frac{\partial \tilde{u}_t}{\partial \xi_2}, \tag{6.37}$$

Since for the viscous sublayer $U^+ = y^+$

$$u_\tau^2 = \frac{-\mu}{\bar{\rho}} \frac{\tilde{u}_t}{n_p}, \tag{6.38}$$

and, consequently,

$$\tau_w == \mu \frac{\tilde{u}_t}{n_p}. \tag{6.39}$$

The mean velocity gradient that must again satisfy $U^+ = y^+$ is given by

$$\left(\frac{\partial \tilde{u}_t}{\partial \xi_2}\right) = \left[\left(\frac{\partial}{\partial \xi_2}(u_\tau y^+)\right)\right]_p = \left[\left(\frac{\partial}{\partial \xi_2}\left(\frac{\bar{\rho} u_\tau \xi_2}{\mu}\right)\right)\right]_p = \frac{\bar{\rho} u_{\tau p}^2 \xi_2}{\mu} = \frac{\tilde{u}_t}{n_p} \tag{6.40}$$

The production term is then deduced to:

$$(P_k)_p = \mu \left(\frac{\tilde{u}_t}{n_p}\right)^2. \tag{6.41}$$

2. Turbulent layer: The wall shear stress is given by

$$\tau_w = \bar{\rho} u_\tau^2 \tag{6.42}$$

For the determination of u_τ on the one hand the logarithmic law of the wall

$$U^+ = \frac{1}{\kappa} ln(y^+ e^{\kappa B}) \tag{6.43}$$

on the other hand the experimental results of fully developed boundary layer

$$U^+ = \frac{\kappa \tilde{u}_t}{ln(y^+ e^{\kappa B})} \tag{6.44}$$

on the other hand the experimental results of fully developed boundary layer

$$U^+ = C_\mu^{1/4}\sqrt{\tilde{k}} \tag{6.45}$$

are used. Combining and in one expression for u_τ^2 the wall shear stress becomes

$$\tau_w = \bar{\rho}C_\mu^{1/4}\sqrt{\tilde{k}}\frac{\kappa\tilde{u}_t}{ln(y^+e^{\kappa B})} \tag{6.46}$$

The mean velocity gradient can be expressed in terms of uô using the same logarithmic law of the wall [73]:

$$\left(\frac{\partial\tilde{u}_t}{\partial n}\right)_p = \frac{u_{\tau,p}}{\kappa n_p} = \frac{C_\mu^{1/4}\sqrt{\tilde{k}_p}}{\kappa n_p} \tag{6.47}$$

Finally, the production term in the control volume is computed as

$$(P_k)_p = \tau_w\left(\frac{\partial\tilde{u}_t}{\partial n}\right) = \frac{\tilde{u}_t\bar{\rho}C_\mu^{1/4}\tilde{k}_p}{n_p ln(y^+e^{\kappa B})} \tag{6.48}$$

The turbulent kinetic energy is a scalar and, thus, a frame independent quantity. The production term calculated using the above formulation is substituted as a source term into the k transport equation in near-wall control volumes without coordinate transformation. The diffusive and convective fluxes through the solid boundary are set to zero. The value of the dissipation rate ϵ_p is taken directly from its transport equation, the correction of which in near wall cells is given below.

Dissipation rate

As mentioned above it is assumed that a local equilibrium is reached between the production and the dissipation of the turbulent kinetic energy. Therefore, the ϵ equation is not solved in the CV next to the wall. Instead the value of ϵ in the CV central point is set to

$$\epsilon_p = \frac{C_\mu^{3/4}\tilde{k}_p^{3/2}}{\kappa n_p} \tag{6.49}$$

For the derivation of this formula the same strategy is applied as for the production term for k except no logarithmic law of the wall, but only experimental results for the fully developed boundary layer are used for the determination of the dynamic velocity u_τ because the logarithmic law of the wall has been already utilized by the formulation of production term.

6.1.9 Symmetry boundary conditions

Symmetry boundaries can be used to reduce the size of the problem. If we know that there is a plane where the flow field is symmetric then instead of simulating the whole configuration, we can set the appropriate boundary conditions and reduce the problem size. The symmetry boundary conditions are set as follows:

$$\frac{\partial \psi}{\partial n} = 0, \quad \psi = \left(\tilde{u}, \widetilde{u_i''u_j''}|_{i=j}, \tilde{\epsilon}, \bar{p}^c, \bar{\rho}, \tilde{z}, \widetilde{z''^2}, \tilde{y}\right) \tag{6.50}$$

$$\psi = 0 \psi = \left(\tilde{v}, \tilde{u}, \widetilde{u_i''u_j''}|_{i \neq j}\right) \tag{6.51}$$

where n is the direction normal to the symmetry plane.

6.1.10 Periodic boundary conditions

The periodic boundary conditions (between boundary I and II) make the variables at the boundary I equal the variables at the boundary II conforming to the following equation.

$$\psi(\vec{r}) = \psi(\vec{r} + \vec{L}), \tag{6.52}$$

where $\vec{r}$ is the position vector and $\vec{L}$ is the periodic length vector of the domain considered. The periodic boundary condition corresponds to zero flux. Making the boundaries periodic, this will make the inflow through one of the boundaries equal the outflow through the other.

6.1.11 Solvers

Solution of the linear equation system

The discretization of the governing equations summarized in section by means of the finite volume procedure explained in section results in a system of linear algebraic equations each having a form. This system can be written in matrix notation as

$$A\underline{\Psi} = \underline{\Psi} \tag{6.53}$$

where A is the square coefficient matrix built from the coefficients of the linear equations 6.3 for each CV,$\underline{\Psi}$ is a vector containing the values of the variable Ψ in each CV and $\underline{S}$ is the vector containing the terms on the RHS of 6.3

The system 6.53 has to be solved by means of an efficient solution method. The coefficient matrix A resulting from 6.3 is sparse, i.e. most of its elements are zero and the non-zero elements lie on a small number of well-defined diagonals (in FASTEST-3D seven diagonals). Advantage should be taken from this structure. Since direct methods like Gauss elimination or LU decomposition do not take this advantage, being quite costly, and since discretization errors are normally much larger than the computer accuracy, there is a clear reason to apply an iterative method. Furthermore, the fully implicitly discretized momentum equations are actually non-linear and cannot be solved by means of a direct method. The details of their linearization are discussed in the following section. In an iterative method some initial solution is guessed and then systematically improved. One would have after n iterations an approximate solution of 6.53, $\underline{\Psi}^n$, that is not the exact one. The nonzero residual vector $\underline{r}^n$ (a difference between the left and the right hand side of 6.53 satisfies the expression

$$A\underline{\Psi}^n = \underline{S} - \underline{r}^n \tag{6.54}$$

An iterative scheme for the linear system that should drive the residual to zero, can be written as

$$M(\underline{\Psi}^{n+1} - \underline{\Psi}^n) = B - (M - N)\underline{\Psi}^n \tag{6.55}$$

$$M(\underline{\Psi}^{n+1} - \underline{\Psi}^n) = B - (M - N)\underline{\Psi}^n \tag{6.56}$$

or

$$M(\underline{\partial}^n) = \underline{r}^n \tag{6.57}$$

Here, $\underline{\Psi}^{n+1} - \underline{\Psi}^n$ is the correction vector which is simultaneously an approximation to the convergence error. Once the computation of $N\underline{\Psi}^n$ is inexpensive and the solution of 6.56 converges rapidly the optimal iterative method is found. For rapid convergence in the solution of 6.56 the matrix M must be as good an approximation to A as possible. For that purpose the $strongly\quad implicit\quad procedure$ (SIP), originally proposed by Stone [74] and further developed for the seven diagonal coefficient matrix by Leister and Peric [75], is applied in FASTEST-3D. In this method the matrix M is chosen to be equal to the incomplete LU decomposition (ILU):

$$M = LU = A + N \tag{6.58}$$

In the ILU decomposition the procedure is the same as in standard LU factorization. But for each zero element of the original matrix A a corresponding element of the lower triangular matrix L or the upper triangular matrix U is set to zero too. Even though L and U have the non-zero elements only on the same diagonals as $A(W, E, S, N, B, T, P)$, their product LU has additional non-zero diagonals $(SE, NWetc.)$. Stone [74] found that convergence can be improved by allowing N to have non-zero elements on the diagonals corresponding to all non-zero diagonals of LU. The elements of the matrix N must be defined so that the elements of vector $N\underline{\Psi} \approx 0$ and that the matrix M to be the best approximation to A. This means that the contribution of the terms on the 'additional' diagonals $(SE, NWetc.)$ in N must be nearly cancelled by the contribution of other diagonals (W, E, S, N, B, T, P). Expecting the solution of the elliptic partial differential equations to be smooth, Stone [74] approximated the unknown function values in 'additional' nodes in terms of the known function values at nodes corresponding to the diagonals of A. Finally, one proceeds as follows. Having a matrix A the elements of N can be found. The elements of M, which are the sum of A and N, do not need to be computed. Instead, the elements of L and U are found in sequential order for the given A and N. Once the elements of L and U are known, the inner iterations begin. The system 6.57 can be rewritten as

$$LU\underline{\partial}^n = \underline{r}^n \tag{6.59}$$

$$U\underline{\partial}^n = L^{-1}\underline{r}^n = \underline{R}^n. \tag{6.60}$$

Using the advantage of LU decomposition the elements of the vector $\underline{R}^n$ are computed first using 6.60 by marching in the order of increasing CV's index (forward substitution). Then the elements of the correction vector $\underline{\partial}^n$ are calculated by marching in the order of decreasing CV's index (backward substitution). In addition to that the variable values in the CVs are updated following $\Psi^{n+1} + \underline{\Psi}^n = \underline{\partial}^n$. The iterations proceed until the sum over all elements of the residual vector $\underline{r}^n$ becomes lower than some given tolerance.

Solution of steady and unsteady problems

In steady computations a steady state solution of the governing equation system is sought. In this case the time history is of no interest. One can either neglect the unsteady terms in the governing equations or iterate until the steady equations are satisfied, or march in time without requiring full satisfaction of the equations at each time step. The iterations within one time step or during steady computations, in which the coefficient matrices and source vectors in 6.3 are updated, are called outer iterations in order to distinguish them from the inner iterations performed on the linear systems 6.3 with fixed coefficients (in the SIP solver). The changes in variables after each outer iteration may be significant and particularly at the beginning where they may cause instabilities. In order to reduce this effect the under-relaxation of the variables is applied:

$$\psi^m = \psi^{m+1} + \alpha_\psi(\psi^m - \psi^{m-1}) \tag{6.61}$$

where ψ^m and ψ^{m-1} are the values of the variable ψ after m-th and (m- 1)st outer iteration, ψ^{new} new is the result of solution of equation 6.3 and the under-relaxation factor α_ψ satisfies $0 < \alpha_\psi \leq 1$. In unsteady computations (URANS) the time accuracy is required in order to resolve in time e.g. some periodical process. In this case the iterations must be continued within each time step until the entire system of these governing equations is satisfied to within a narrow tolerance.

6.2 Numerical method of the transport equations for the dispersed phase

6.2.1 Solving the equation of motion and time discretization

Since equation 4.3 is an ordinary differential equation, it can be solved by using classical numerical methods such as Euler's forward integration method [72]:

$$x_i^{n+1} = x_i^n + \partial t u_i^n, \tag{6.62}$$

$$u_{d_i}^{n+1} = u_{d_i}^n + \frac{\partial t}{m_d} \sum F_i^n, \tag{6.63}$$

where x_i and u_{d_i} denote the parcel location and velocity component respectively. From one given time point (t_n), it is possible to find the next point at a given time step (t_{n+1}) along the same streamline and thus tracking the whole line. The Euler's forward method is fast but strongly depends on the quality of the initial velocity field. In some situations, it may lead to spirals. Then, additional stopping conditions must be added to avoid such situations. Moreover, in zones where the velocity orientation changes, the streamline presents a high curvature and its trajectory is not necessarily parallel to the initial velocity field. The Euler's method is a simple approach to implement. However, it has a low accuracy, as it is a first order method. If one wishes to compute very accurate solutions or solutions that are accurate over a long interval, then Euler's method (used for the dispersed phase in this work $\approx$ equation 4.3-) requires a large number of small steps. (accuracy $\approx$ dt), but thus one rends the simulation time impractically long.

Other time integration methods often used in literature are Runge Kutta method [126] and the backward Euler method [72], which are implicit. These methods require the resolution of a linear system per iteration, as well as the storage of the system state added to those required for the system resolution algorithm. These methods are supposed to provide approximate results that are not subject to numerical instability as the time step is increased [72]. As mentioned above, time steps within Euler's forward method, are limited by the conditions for physical processes and numerical stability according to:

$$\partial t = 0.1 \quad min(\tau_p, T_E, T_W, T_{CV}), \tag{6.64}$$

where τ_p denotes the particle relaxation time, defined in section 4.2, and T_E is the turbulent integral time scale

$$T_E = c_T \frac{k}{\epsilon} \tag{6.65}$$

The variable T_W is the time required by a parcel to traverse a turbulent eddy

$$T_W = \frac{L_E}{|\vec{u} - \vec{u}_d|}, \quad \left(L_E = T_E \sqrt{\frac{2}{3} k} \right), \tag{6.66}$$

and the variable T_{CV} represents the time taken by a parcel to cross the entire control volume.

$$T_{CV} = \frac{\partial x_i}{|u_{d_i}|} \tag{6.67}$$

6.2.2 Statistical sampling

Similarly to the Eulerian part where equations averaged for flow quantities (velocity, mass fraction, temperature, etc) are solved, in the Lagrangian part momentanous quantities are to be sampled and averaged. Mean values and variances of droplet characteristic variables (velocity components, diameter, temperature, etc.) are evaluated in each cell according to [39]:

$$\overline{\phi_d} = \frac{\sum_{k=1}^{K_d} \left(\sum_{n=1}^{N_{CV}} \phi_{d,i,j,k} N_{d,k} \right)}{\sum_{k=1}^{K_d} N_{CV}} \tag{6.68}$$

$$\overline{(\phi_d')^2} = \frac{\sum_{k=1}^{K_d} \left(\sum_{n=1}^{N_{CV}} \phi^2_{d,i,j,k} N_{d,k} \right)}{\sum_{k=1}^{K_d} N_{CV}} - (\overline{\phi_d}) \tag{6.69}$$

where K_d is the total number of numerical droplets in a considered cell, N_{CV} represents the number of time steps which a droplet needs while crossing the cell and $N_{d,k}$ is the number of real particles represented by a numerical one. One should mention here that the total number of particles/droplets within a control volume represents an important factor for the accuracy of statistics of dispersed phase properties. In order to secure smooth distribution of results, the variables $N_{d,k}$ is desired not to exceed 10^3, as pointed out in [39]. Nevertheless, regions where particles/droplets are not able to reach, due to high shear flow or due to total evaporation, are characterized by non-uniform property profiles. The particles/droplets mass concentration within a control volume is computed in the following way:

$$\sigma_d = \sum_{k=1}^{K_d} \left(\sum_{n=1}^{N_{CV}} \frac{m_d N_{d,k}}{\vec{u}_{d,k} \partial A_j \partial t_{in}} \right) \tag{6.70}$$

where ∂A_j denoted the cross section area of the considered control volume, ∂t_{in} represents a reference time, which specifies the droplets/particles mass flow at the boundary conditions.

Though the results from URANS are unsteady, one is often interested only in the time-averaged flow. Coherent motion of the velocity component can then be decomposed in

$$U = \left\langle \bar{U} \right\rangle (x) + u'(x,t) + u''(x,t) \tag{6.71}$$

$\left\langle \bar{U} \right\rangle$ is the time averaged velocity, u' is the deviation of the phase averaged from the time averaged velocity component and u'' is the turbulent fluctuation.

The time averaged mean velocity component is obtained by averaging all time steps N as

$$\left\langle \bar{U} \right\rangle = \frac{1}{N} \sum_{N}^{k=1} \left\langle \bar{U} \right\rangle (x) + u'(x,t). \tag{6.72}$$

6.3 Euler-Lagrange coupling and underrelaxation of dispersed phase source terms

6.3.1 Steady coupling

Numerically, the interaction between the continuous and the dispersed phases is taken into account by means of several couplings between the two modules involved. Following a steady method, after several iterations of gas phase alone, the gas variables are kept frozen and all the particles representing the particles are injected in the computational domain. The computed particle source terms are inserted in the calculations of gas phase and kept frozen till the next coupling takes place in which the old particle sources are replaced by newly calculated sources. The particle source terms has to be inserted in the calculation of the gas phase to ensure the full two-way physical coupling as permitted by a mean concentration of particles shown in figures 6.5. High levels of under-relaxation technique were used in order to obtain successful convergence (Chrigui et al. 2004, Sadiki et al. 2005, Kohnen et al. 1994). Due to the presence of particles source terms, the conventional residuals are characterized by a jump of residuals after each coupling. To avoid it, an additional under-relaxation technique should also be employed for particle source terms (Kohnen et al. 1994).

$$S_{\phi p}^{i+1} = S_{\phi p}^{i} * (1-\gamma) + S_{\phi p(cal.)}^{i+1} * \gamma \tag{6.73}$$

where $S_{\phi p}^{i+1}$ and $S_{\phi p}^{i}$ are the particle source terms appearing at i+1th and ith couplings, respectively. The under-relaxation factor γ takes values in the interval [0,1]. In the frame of this work, convergence of the Eulerian-Lagrangian coupling procedure is reached when the fluid's properties do not change their value from one coupling to the next in the presence of particles. This was mainly achieved after 10 couplings. Figure 6.5 shows the procedure of the steady coupling. First the carrier flow equations are solved in steady mode to reach the converged solution for statistical quantities without presence of particles. The particle motion equation would then be called and the particle will be tracked through the computation domain. The solution procedure will proceed until a converged solution is reached.

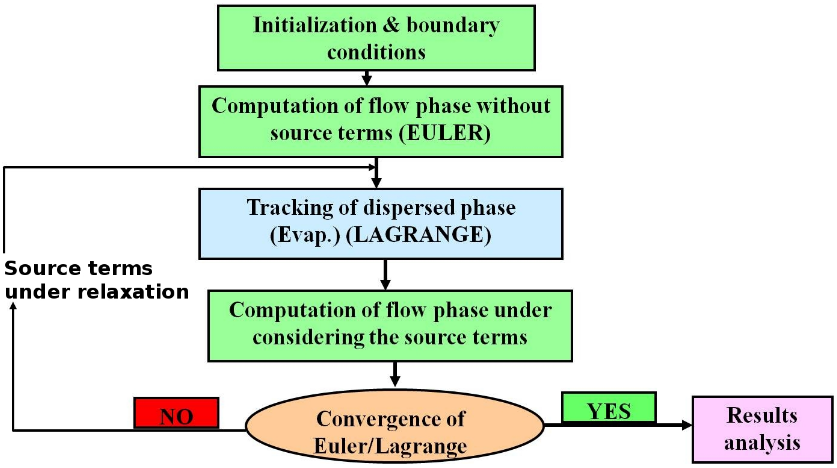

Figure 6.5: Diagram for numerical steady coupling between the continuous and dispersed phases in the frame of Eulerian/Lagrangian approach [150].

6.3.2 Unsteady coupling

In an unsteady coupling, the carrier phase is first calculated in unsteady mode to reach a converged solution for statistical quantities. The statistical data are used to calculate the turbulent time and length scales at different positions in the flow geometry. Turbulent time scales (eddy life time, T_{eddy}) are then used to determine the coupling time T_{cpl} in such a way that all physical phenomena and interactions between particles and energy containing eddies can be captured. This implies that the coupling time should be smaller than the life time of smallest energy containing eddy ($T_{cpl} < T_{eddy}$). This coupling procedure is described in Figure 6.6. After the carrier phase calculation with the FASTEST-3D the LAG3D reads the carrier phase parameters. The particles are then injected and tracked for the flow time step dt_1. The particle positions and particle source terms are calculated and stored for this time step. LAG3D is then frozen and FASTEST is started with the particle source terms. After reaching the defined residuals for FASTEST the new time step dt_2 is started. For the new time step the old positions of the particles is read and tracked during the new time step. Additionally, new particles are injected and tracked for the new time step with all actions included in 'a' (see Figure 6.6). If the residuals do not get less, one can change time step, under-relaxation, convergence criteria etc. to reach convergenced solution. The time step for the particles lies in the range of $10^{-9}s$ and $1s$ with a couplings time of $10^{-2}s$ and 100 couplings were needed to get converged solution.

6.3.3 Two-way coupling

As pointed out in 4.3 the key physics in dispersed multiphase flows are in the coupling between the phases through the mass, momentum, transported mixing and scalar quantities. In addition, extra mechanisms of turbulence modulation including turbulence production, distortion, and dissipation may become important and affect the turbulent stresses (Chrigui et al. 2004, Ahmadi et al. 2006,

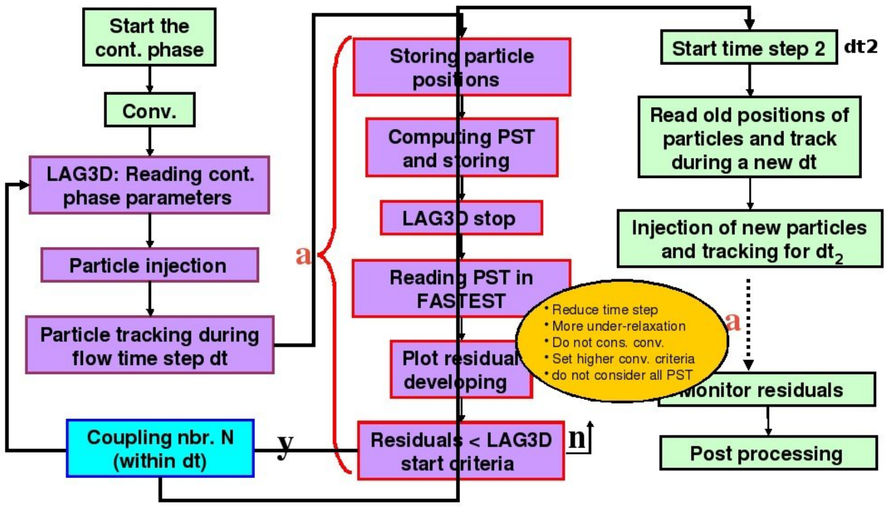

Figure 6.6: Diagram for numerical unsteady coupling between the continuous and dispersed phases in the frame of Eulerian/Lagrangian approach[151].

Tanaka et al. 2008, Beishuizen et al. 2007, Lain & Sommerfeld 2003). This is the case in configurations with higher volume fraction or when $D_p \geq \eta$ (η: Kolmogorov length scale and D_p particle diameter). In the following chemical reactions are not considered. According to the classification criteria of interphase coupling by Crowe et al. (1996) (see also Chrigui et al. 2004, Ahmadi et al. 2006, Beishuizen et al. 2007), the flow systems under study belong to dilute two-phase flows in which the particle volume fraction is of the order of 10^{-5} (see for example Figure 6.7). Therefore a full two-way phase coupling is important, whereas a four-way coupling is negligible.

In polydisperse multiphase flows different mechanisms can cause turbulence modulation, and sometimes multiple mechanisms act simultaneously, so that an overlap of particle-induced turbulence attenuation and production should be expected. As pointed out in Chrigui et al. (2004), Ahmadi et al. (2006), Tanaka et al. (2008), Beishuizen et al. (2007), Lain & Sommerfeld (2003) this complex phenomena cannot be well captured by classical approaches. Because both particle-induced attenuation and production of continuous phase turbulence due to interphase couplings are thermodynamic processes, we follow Sadiki (2005) and apply in this work a thermodynamically consistent modulation model as used in Groh et al. (2004) and also Chrigui et al. (2004), Chrigui et al. (2010), Sadiki et al. (2005), Chrigui et al. (2003). This model has been designed in Ahmadi et al. (2006) and Sadiki et al. (2005) based on the exploitation of the entropy inequality expressing the second law of thermodynamics for multiphase flows. The particle source term for the turbulent kinetic energy is then given in the model in Chrigui et al. (2004), Sadiki et al. (2005):

$$S_{k,p} = \beta^* (\overline{u_{pi} S_{ui,p}} - \overline{u_i}\,\overline{S_{ui,p}}) - (\overline{u_i S_{ui,p}} - \overline{u_i}\,\overline{S_{ui,p}}) \tag{6.74}$$

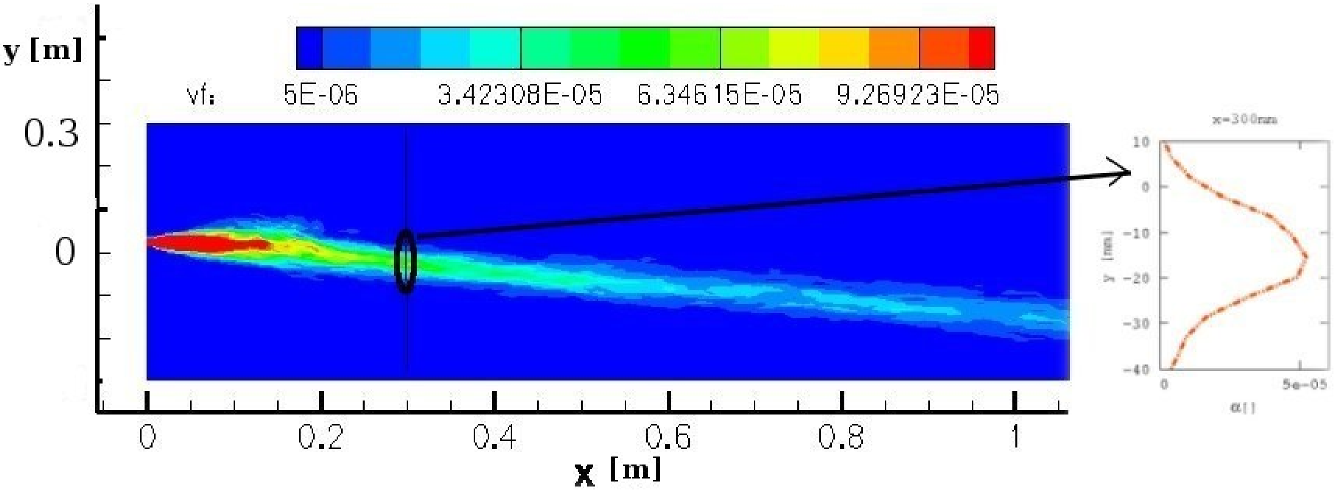

Figure 6.7: Variation of the particle volume fraction (α) in the computational domain of the configuration investigated in section 7.2: (particle laden shear flow)

where

$$\beta^* = \acute{\alpha} + \frac{(1-\acute{\alpha})(\overline{u_{pi}S_{ui,p}} - \overline{u_{pi}}\,\overline{S_{ui,p}})}{(\overline{u_{pi}S_{ui,p}} - \overline{u_i}\,\overline{S_{ui,p}})} \tag{6.75}$$

is a model parameter. Such a consistent approach is proven to improve the prediction of turbulence modulation, which in turn affects the particle dispersion. The second term in Eq. 6.74 represents the usual dissipative standard contribution as given in Table 4.1, while the first term accounts for the production of the turbulent kinetic energy. So, this thermodynamically consistent model captures well both the enhancement and the diminution of the turbulence of the gas phase due to the presence of both big and small particles in polydispersed sprays or multiphase flows. The parameter $\acute{\alpha}$ in Eq. 6.75 depends on the particles properties, as shown in Sadiki et al. (2005). The relevance of this model has already been demonstrated in the frame of RANS (Chrigui et al. 2004, Sadiki et al. 2005) and LES (Groh et al. 2004). Note that in the model by Crowe et al. (1996) which is reformulated by Lain & Sommerfeld (2003) in a Lagrangian form, the second term in Eq. 6.74 disappears while $\beta^* = 1$. In this work β^* has been set to $\beta^* = 0.7$

6.3.4 Under-relaxation of source terms

Numerical methods are used to solve the equations for fluid flow and particles/droplets evolution. The Methods often employ more iteration procedures which require a criterion which is used to decide when the iterations can be terminated. In many cases, iteration methods are supplemented with relaxation techniques. For example, over relaxation is often used to accelerate the convergence of iteration methods. Under-relaxation is sometimes used to achieve numerical stable results. Kohnen et al. showed in his work that it is mandatory to use under-relaxation factors for the particles/droplets source terms which are introduced in the transport equations of the gas phase. The under-relaxation of particles/droplets source terms is accounted for using the following expression:

$$S^{i+1}_{\phi,p(considered)} = \alpha S^{i+1}_{\phi,p} + (1-\alpha) S^{i}_{\phi,p}. \tag{6.76}$$

Here $S^{i+1}_{\phi,p}$ is the new computed particles/droplets source terms within the iteration (i+1), whereas $S^{i}_{\phi,p}$ is the old source terms (previous iteration) and $S^{i+1}_{\phi,p(considered)}$ the source terms account for the carrier phase. The variable α indicates the under-relaxation factor, which vary between zero and one. It is defined by user and cannot influence the numerical results once convergence reached.

The goal of introducing under-relaxation factors is to enhance the numerical stability and to accelerate the convergence of the Eulerian- Lagrangian coupling. Sommerfeld [25] mentioned that an underrelaxation factor of 0.1 was required for his work to get a stable numerical computation and that the total Eulerian-Lagrangian coupling was between 30 and 50 iterations.

7 Particle dispersion without droplet phase change

7.1 Particle dispersion in a vertical channel flow

To see the influence of different dispersion models a simple test case represented by a vertical channel flow is first considered. Other physical effects influencing the particle motion like wall collisions including the effect of wall roughness and transverse lift forces as well as evaporation are neglected to highlight the ability of the dispersion models.

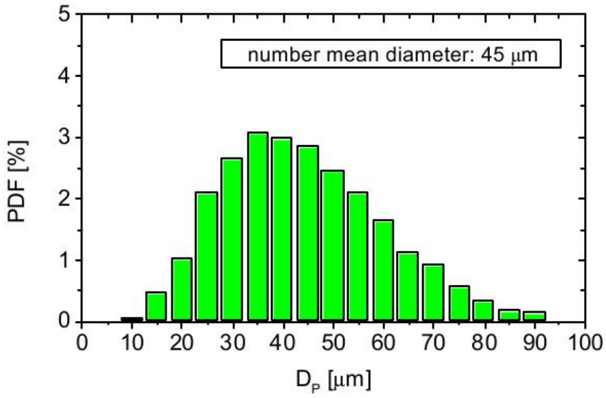

Figure 7.1: Measured size distributions of the gas beads (number fraction) [39]

7.1.1 Experimental and numerical setup

7.1.2 Configuration

The flow configuration is shown in Fig. 7.2. A plane particle- laden air jet mixes with two co-flowing plane jets within a vertical channel. The walls of the channel were made of milled alu-

Table 7.1: Particle size distributions (number fraction in size classes of $5\mu m$)

Particle Size in μm	10	15	20	25	30	35	40	45	50
Number Fraction in $\%$	0.075	0.47	1.05	2.1	2.67	3.1	3	2.86	2.48
Particle Size in μm	55	60	65	70	75	80	85	90	0
Number Fraction in $\%$	2.1	1.67	1.14	0.95	0.57	0.36	0.19	0.14	0

Table 7.2: Flow conditions for the test case, air density: ρ=1.1307 kg/m^3, dynamic viscosity of air: $\mu = 18.6 * 10^{-6}$ kg/(ms)

Properties	Number	Unit
Number mean diameter of particle	45	μm
Particle mass flow rate	0.04	g/s
Mass loading	0.002	-
Mass flow rate of air in central channel	18.93	g/s
Mass flow rate of air in both outer channels	41.59	g/s
Average air velocity in the channel $\overline{U_0}$	8.56	m/s
Reynolds number based on total channel width	13009	-
Transverse velocity fluctuation of particles $\acute{v_p}$	$0.35\acute{u_p}$	m/s

minum alloy plates. The particles were spherical glass beads ($\rho_p = 2.5g/cm^3$) with a mean number diameter of 45 μm.

The measured number size distributions of particles are given in Fig.7.1 and Table 7.1. The particle mass loading in the central channel was 0.02. Therefore, the influence of the particles on the gas phase may be neglected. The flow conditions for the test case are summarized in Table 7.2.

7.1.3 Results and discussions

Relating to different dispersion models results of the numerical prediction of the particle dispersion in a channel flow are given.

In comparison with the measurements in Figures 7.3 - 7.9. The comparison of the mean air Fig. 7.3. A slight over-prediction of the turbulent kinetic energy is observed for x = 300 mm.

The differences in turbulent kinetic energy are mainly attributed to an incomplete turbulence modeling of the fluid phase. For x = 20 mm and x = 100 mm the predicted turbulent kinetic energy values of the fluid turbulence lies above the measurements, whereas for x=300 mm the agreement near the center line is fairly good. However, the increasing fluid turbulent velocity fluctuation when approaching the wall is not possible to simulate by a standard k-ϵ model which is based on the assumption of isotropic turbulence. An improvement in this region can be only possible by taking into account the anisotropy of the turbulence.

For the simulation 250 thousand control volumes and 200 thousand particles were used in a steady mode, which were sufficient for the gas phase as well as particle phase. Fig. 7.4 - 7.6 show the measured and simulated particle velocity and particle fluctuation for all three dispersion models used. In the case of particle velocity compared to the experimental data there is no big difference between the three dispersion models used (see Figure 7.4-7.6). Differences are seen in terms of rms of axial particle velocity. For the first region x=2mm RWM and PLM overpredict the particle velocity fluctuation in the shear flow region, whereas RWM-Aniso fit the experimental date quite well. Most likely have the overpredicted turbulent kinetic energy values in these regions for the gas phase are damped by the RWMs, whereas the PLM consider this overprediction and so match better to the gas phase. Since the particles are small and consequently have a short relaxation time so for the next region x=100 mm the fluctuation of the particle velocity decay due to the adjustment to the gas phase. So the RWM-Aniso underpredicts the particle velocity fluctuation in this region,

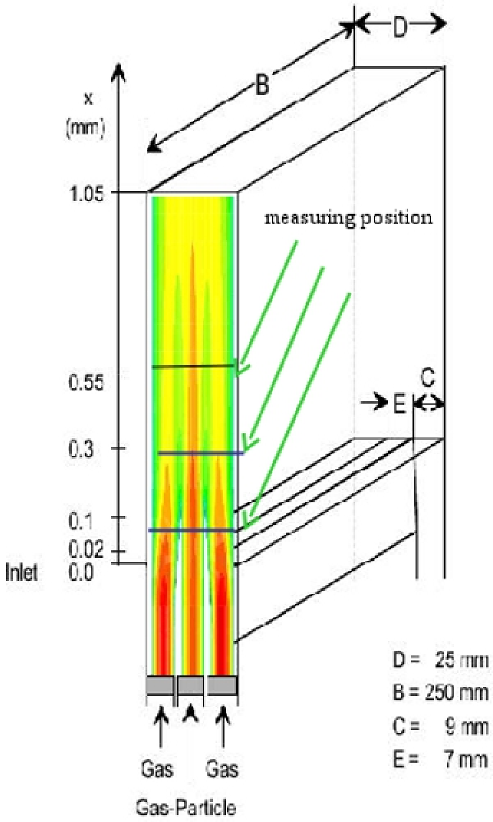

Figure 7.2: Configuration of the vertical channel flow [39]

whereas the RWM-Iso predict the velocity fluctuation also well, which is not physically. For the same region PLM provide good results. At x= 550mm the PLM predicts very well the particle velocity fluctuation, whereas RWMs predict an almost standard rms values almost throughout the chanel. Here one can see the ability of the PLM for predicting the rms values of the particle velocity in a steady mode which indicate a more physical way of simulating dispersion with this model.

7.1.4 Conclusion

In order to appraise the quality prediction of dispersion models a vertical channel flow simulation in RANS-context has been analyzed. For this purpose, three dispersion models, namely the RWM-Iso, the RWM-Aniso and the PLM have been used. Their performances with respect to the particle velocity and velocity fluctuation have been compared using the $k - \epsilon$ turbulence model to describe the turbulent carrier phase flow. Based on the results, following conclusions can be drown:

1. The use of a simple dispersion model such as Random Walk Model would not return reliable results especially far away from the particle injection inlet.
2. Advanced dispersion model such as Particle Langevin Model (PLM) seems to be able to capture the essential dynamics of the flow. This particularly improves the subsequent particle simulation.

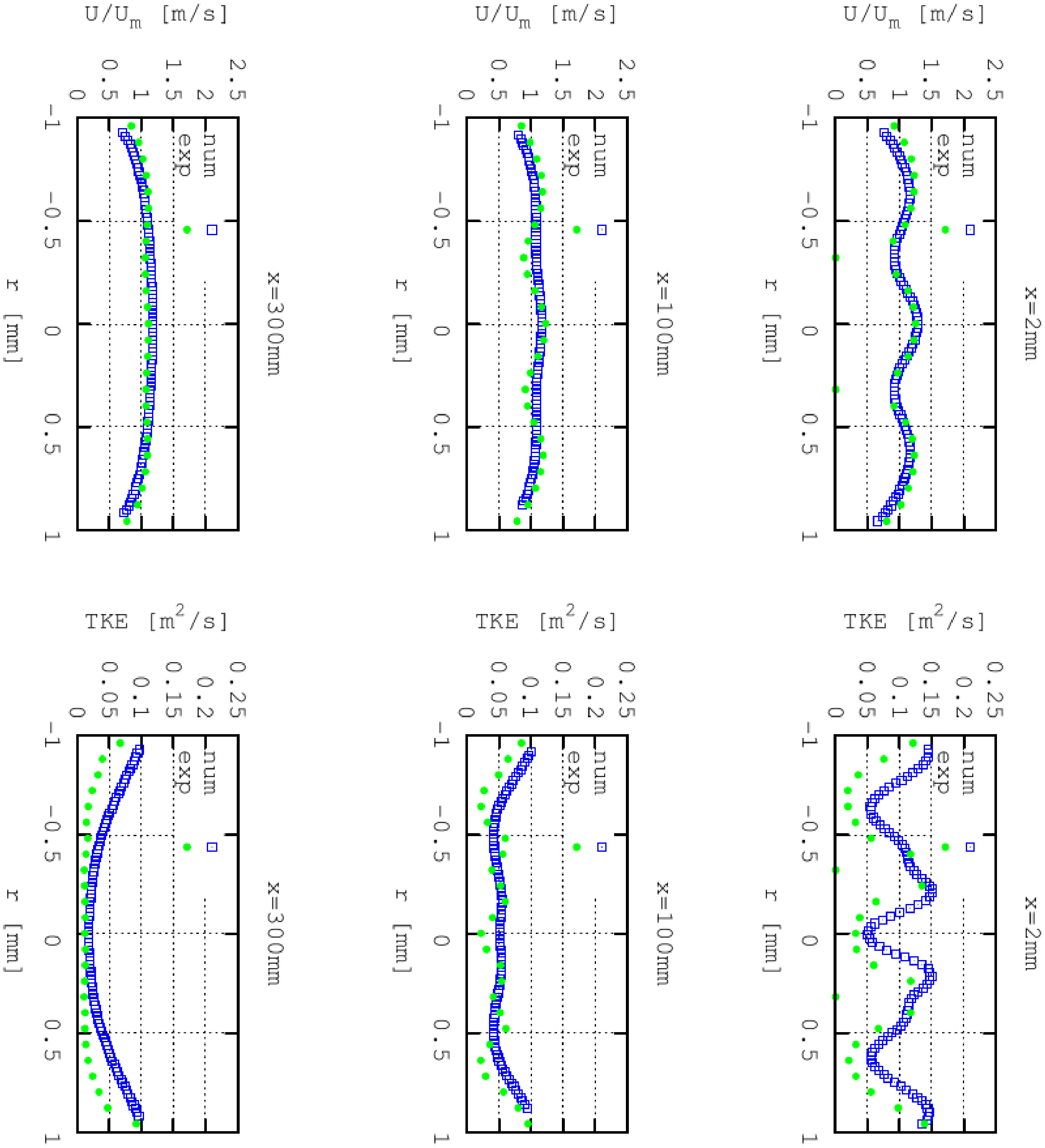

Figure 7.3: The axial velocity and turbulent kinetic energy of the gas phase in the vertical channel along the $r = y/D$

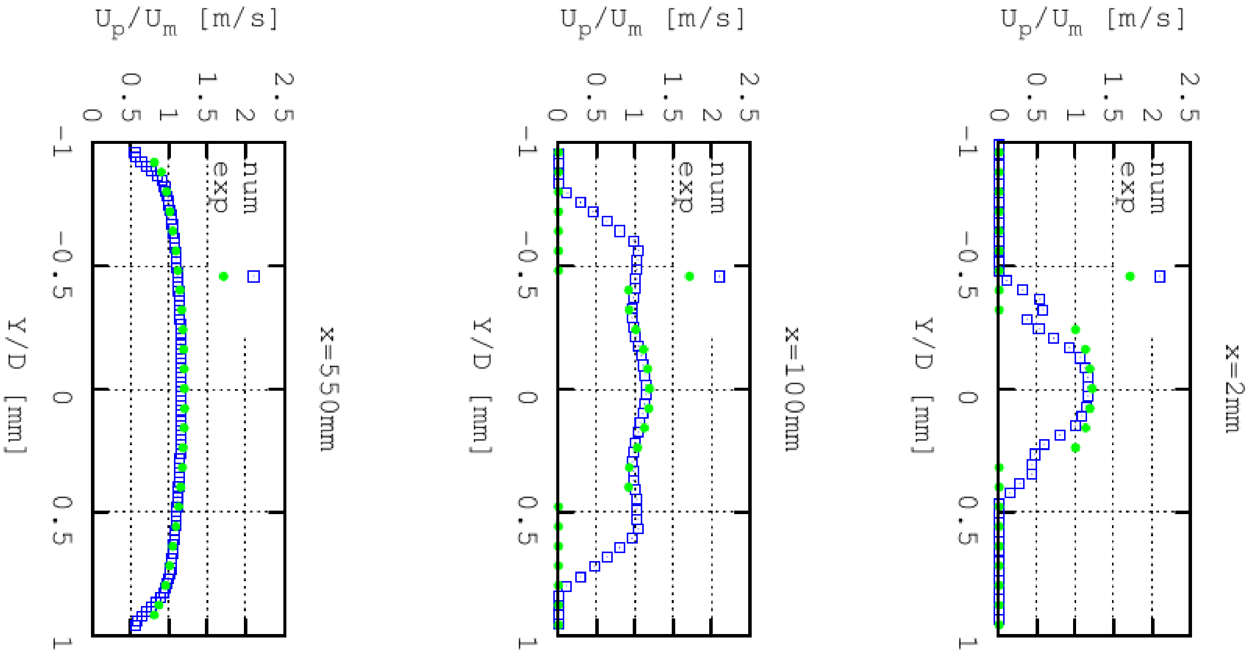

Figure 7.4: Axial velocity of the particles with RWM-Iso along the $r = y/D$

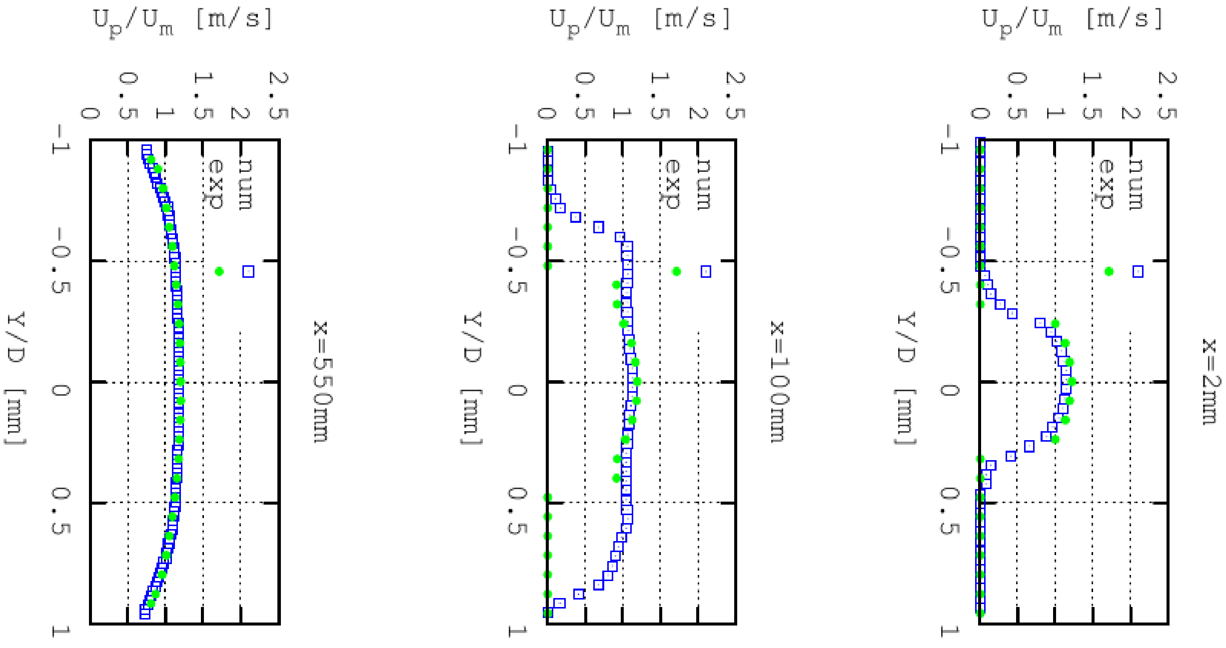

Figure 7.5: Axial velocity of the particles with RWM-Aniso along the $r = y/D$

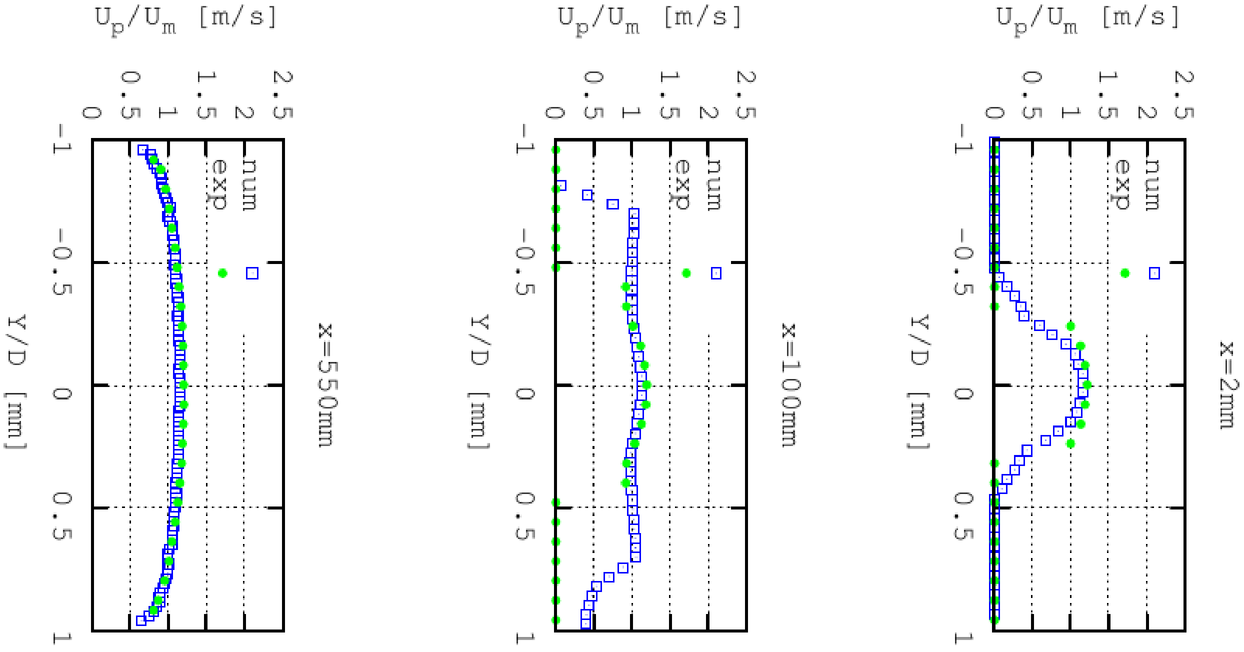

Figure 7.6: Axial velocity of the particles with PLM along the $r = y/D$

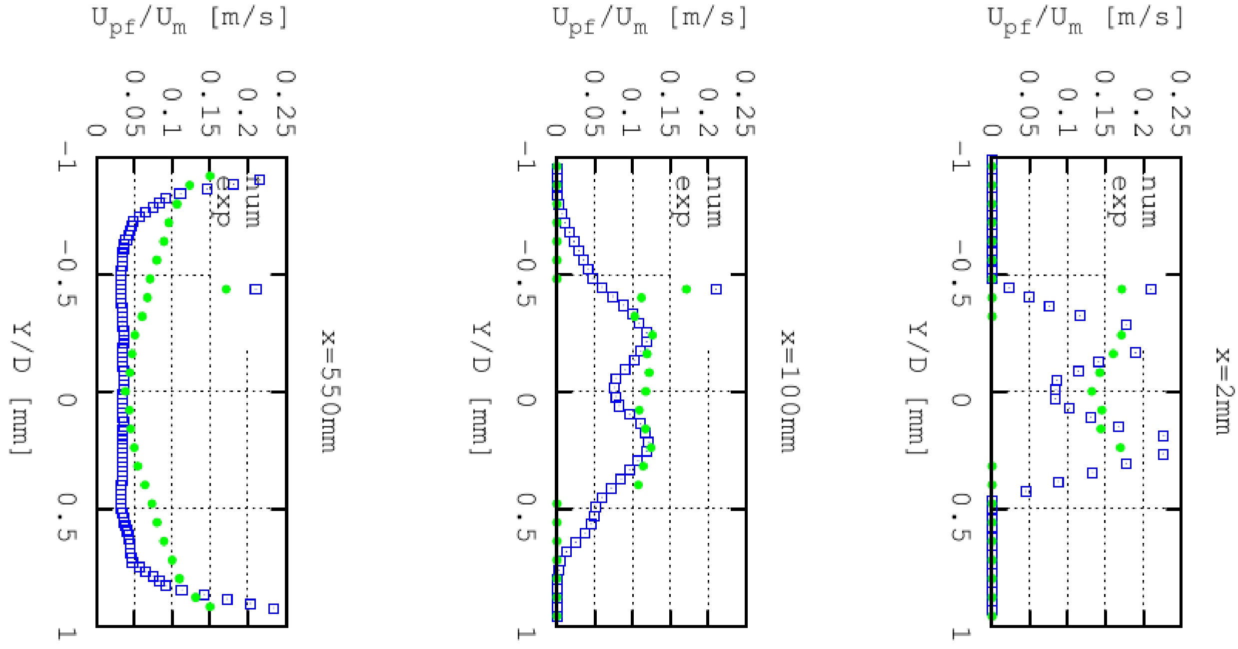

Figure 7.7: RMS of the axial velocity of the particles with RWM-Iso along the $r = y/D$

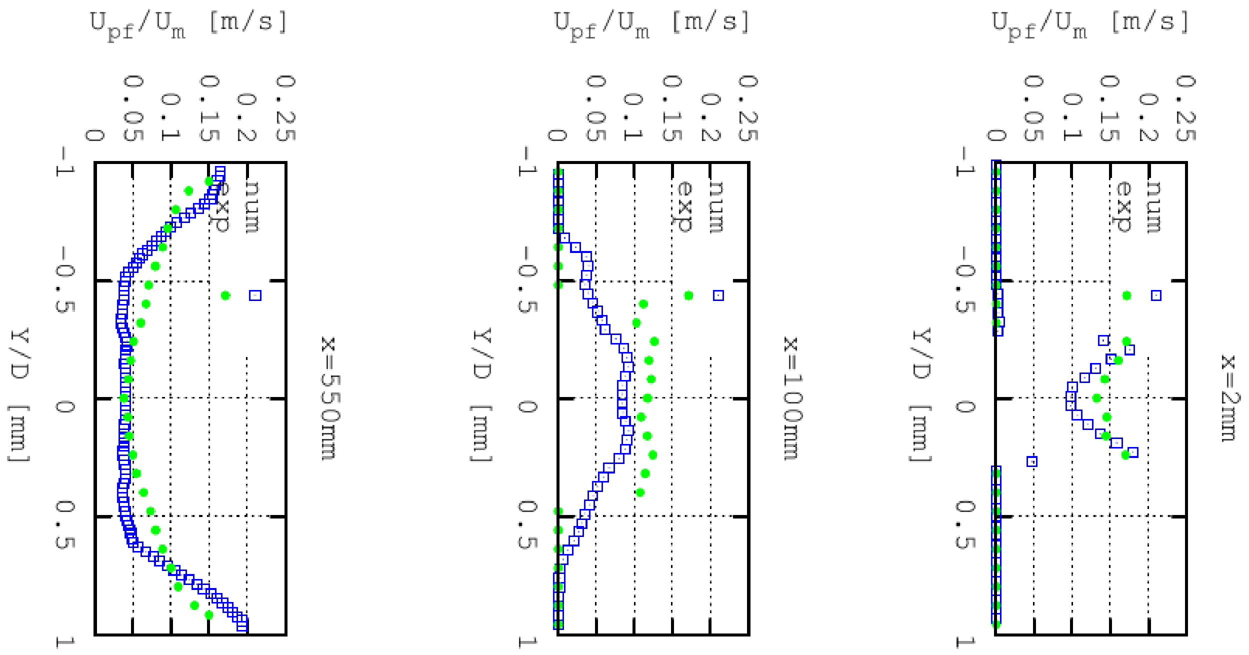

Figure 7.8: RMS of the axial velocity of the particles with RWM-Aniso along the $r = y/D$

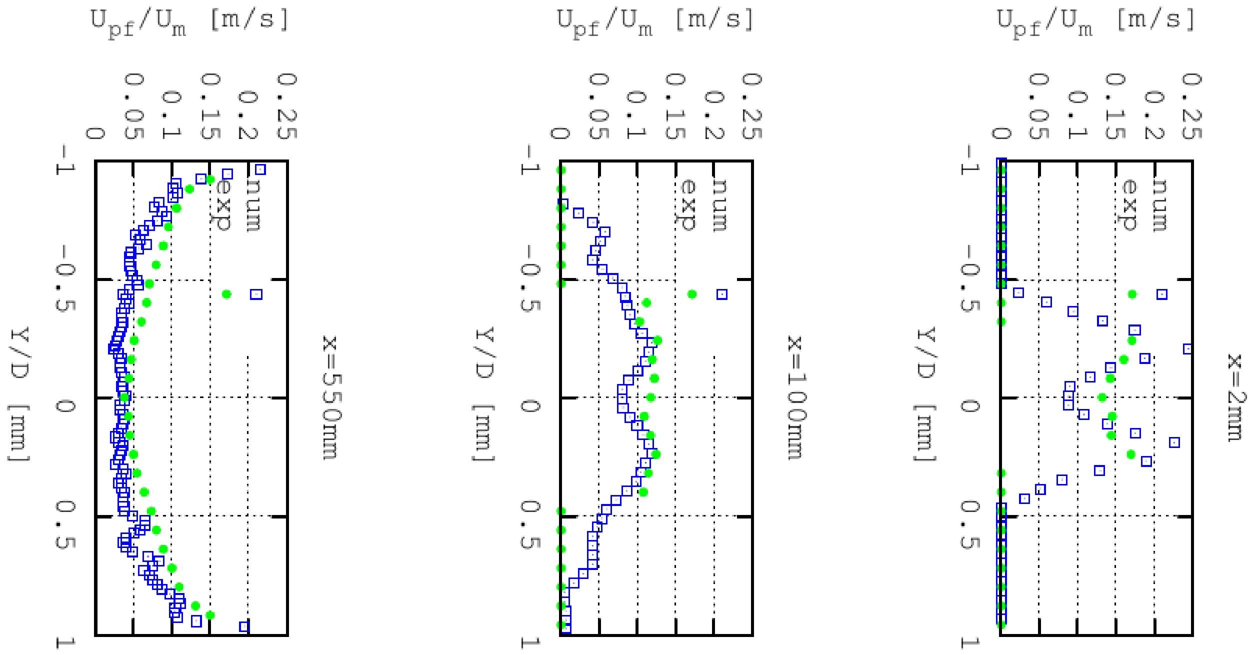

Figure 7.9: RMS of the axial velocity of the particles with PLM along the $r = y/D$

7.2 Particle-laden shear flow

For the further validation of the different dispersion modeling a particle laden shear flow is used for its non-homogeneous and non-isotropic properties.

7.2.1 Configuration

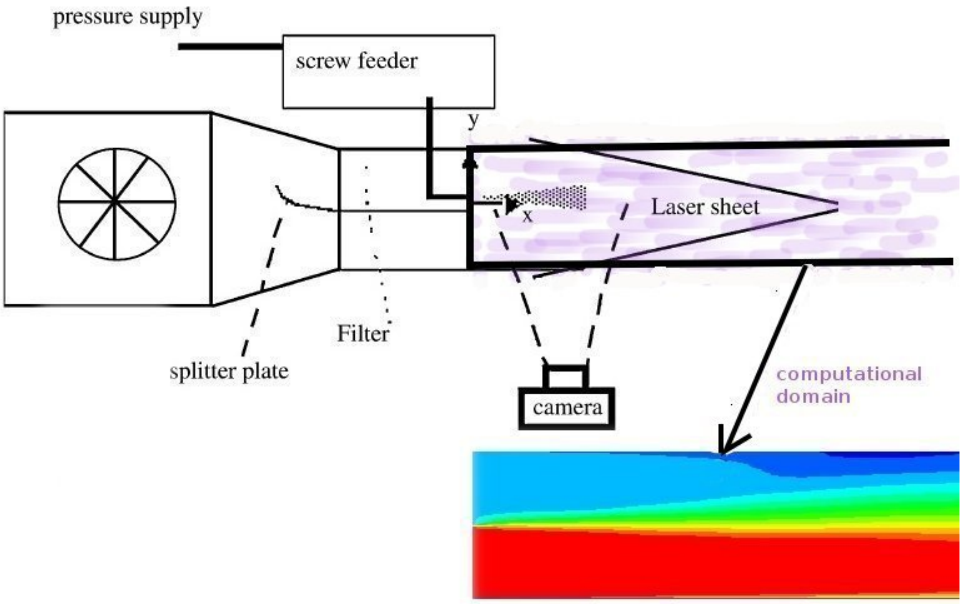

Figure 7.10: Experimental setup computational domain (velocity field)

The geometry under study is represented in Figure 7.10. It displays a shear layer flow, a well understood configuration for the single phase case while being a non-homogeneous and non-isotropic turbulent flow laden with particles. This configuration has been investigated experimentally by Horender (2005).
The Experimental results are used to validate the numerical results. The fluid velocity is $0.8m/s$ on the low speed side and $5.5m/s$ on the high speed side. The gravity is pointed from the low speed to the high speed side. The properties of air are density $\rho_f = 1.2kg/m^3$ and kinematic viscosity $\nu = 1.5 \cdot 10^{-4} m^2/s$.
The injection rate of particles is $7.0 \cdot 10^{-4}$ kg/s. The density of the particles is $2590kg/m^3$ and the particle diameter lies in the range of $70 - 110\mu m$. The inlet particle velocity is $3m/s$ with rms of stream-wise and cross-stream velocity fluctuations of $0.3m/s$ and $0.2m/s$, respectively.
The uncertainties are reported 2% and 7% for the mean particle velocity and the rms of the velocity fluctuations in Horender (2005), respectively. The uncertainties are expected to be somewhat larger in regions with few particles.

Table 7.3: Different Model combinations used

Cases	Turbulence model	Dispersion model	Coupling
X_1	k-ϵ	RWM-Iso	steady
X_2	k-ϵ	PLM	steady
X_3	k-ϵ	RWM-Iso	unsteady
X_4	k-ϵ	PLM	unsteady
X_5	k-ϵ	RWM-Aniso	steady
X_6	k-ϵ	RWM-Aniso	unsteady

7.2.2 Numerical setup

Calculations have been performed on a grid with approximately 400 thousand control volumes. This mesh resolution has been chosen to ensure a grid independent solution when the standard $k-\epsilon$ model is used. Both, steady and unsteady coupling approaches along with three dispersion models have been applied. For both approaches the convergence criteria was set to 10^{-4}. The time step for carrier phase and the coupling time for unsteady approach have been set to 10^{-4}s and 10^{-2}s, respectively. Table 7.3 summarizes the different model combinations applied.

7.2.3 Results and discussions

Let us first focus on the single-phase flow. This step is the essential one for the subsequent particle simulations. Figure 7.11 presents mean velocity profiles and turbulent kinetic energy of the single gas phase at axial positions $x = 10mm$, $x = 100mm$ and $x = 300mm$ for RANS and URANS in comparison with the experimental data from Horender (2005).

The turbulent kinetic energy in case of unsteady simulation is consisted of the modeled turbulent kinetic energy and the resolved turbulent kinetic energy. A remarkable difference between steady and unsteady mode is not observed attesting that the degree of unsteadiness is not significant at these positions. First at the axial plane $x = 1200mm$, further downstream, a difference between steady and unsteady simulations (Figure 7.12) may be observed. This is probably due to the higher turbulence intensity generated.

Note that the experimental data has been evaluated assuming that the turbulence is almost isotropic. This may justify the existing deviation between experimental data and numerical results, especially in the plane downstream at $x = 300mm$ for the turbulent kinetic energy.

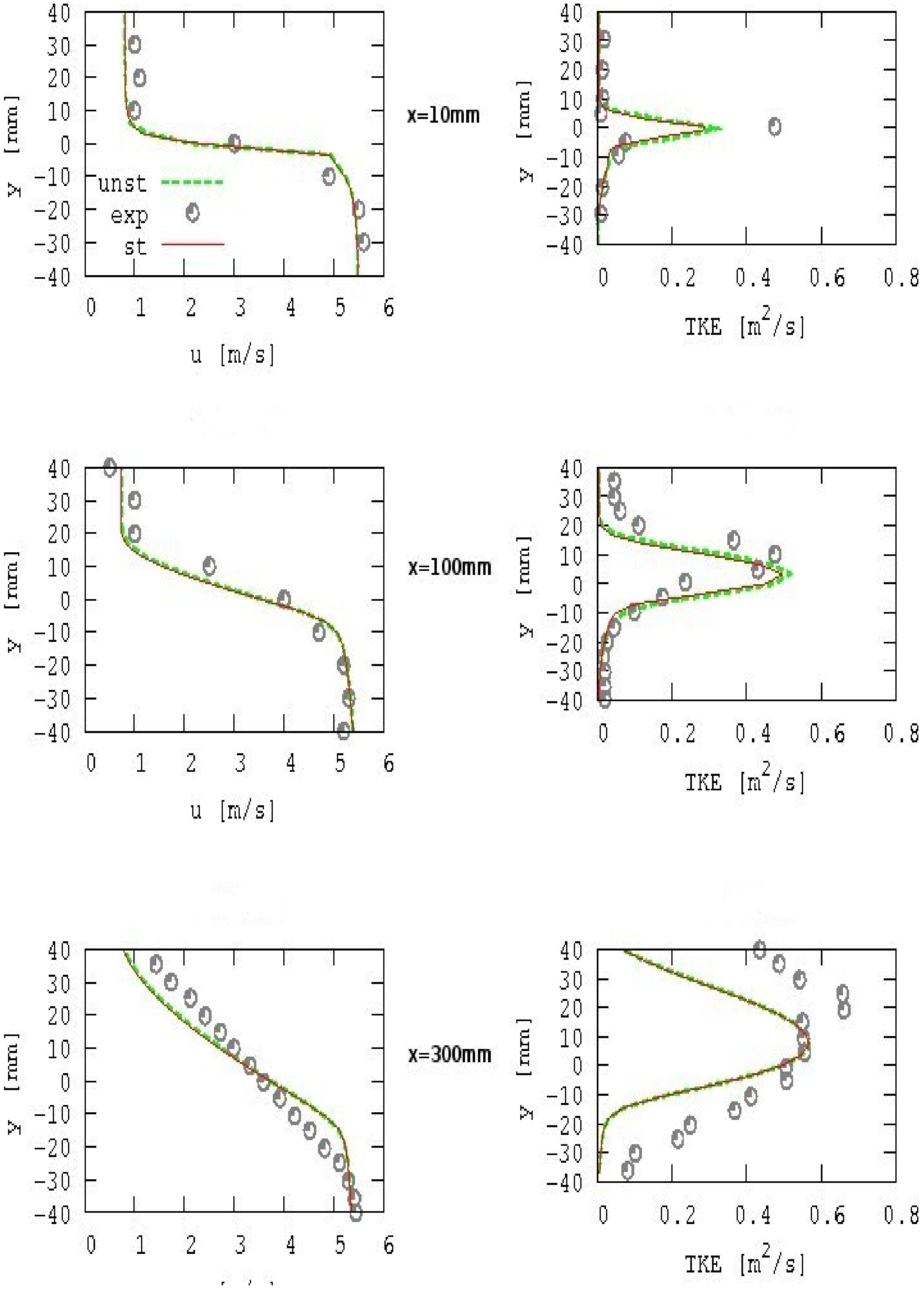

Figure 7.11: Velocity (left) and turbulent kinetic energy (right) for the gas phase: comparison of steady (dashed lines) and unsteady (lines) calculations with experimental data (dots) at axial positions $x = 10mm$,$x = 100mm$ and $x = 300mm$

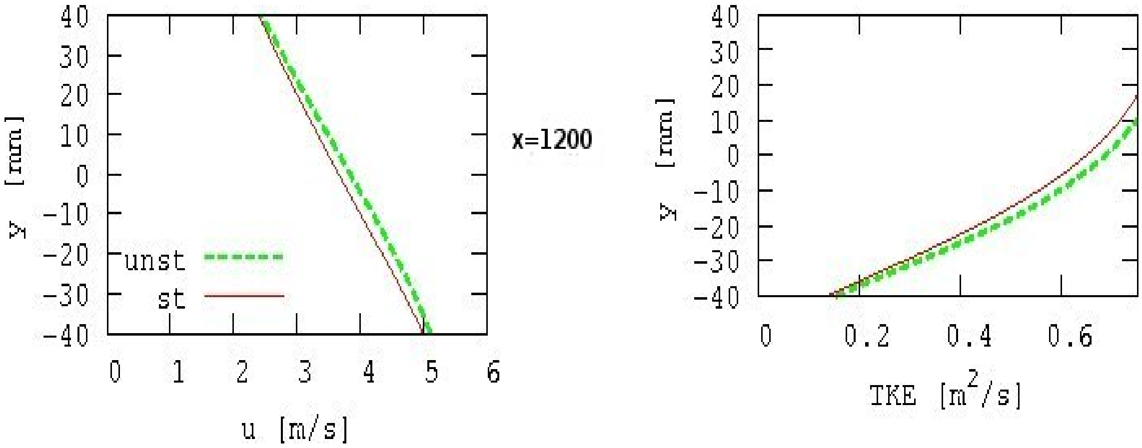

Figure 7.12: Velocity and turbulent kinetic energy for the gas phase: comparison of steady (dashed lines) and unsteady (lines) calculation at the axial position $x = 1200mm$

Concentrated now on the two-phase flow case, the results for the cases $X_1 - X_6$ as described in Table 2. will be presented and discussed.
It should here be noted that the reference experimental data for particle mean velocity and particle fluctuation and concentration are only provided at $x = 300mm$ (see Horender 2005).

Comparison of RWM-Iso to PLM in steady and unsteady mode:
Figures 7.13 and 7.14 show the numerical results for both particles mean velocity and particle fluctuation at $x = 300mm$ obtained from steady and unsteady simulations using different dispersion models (cases X_1, X_2 and X_3, X_4), respectively. The steady results indicate that the mean particle velocity is well predicted by RWM-Iso and PLM. In contrast to the particle mean velocity, the rms values of particle velocity fluctuations are predicted well by the PLM while the RWM-Iso underpredicts them. The unsteady coupling does not change significantly the results of RMW-Iso, while it improves slightly the PLM results especially for particle stream wise fluctuation. Based on the results, it can be concluded that the RMW-Iso model does not have capability to predict the particle fluctuations. It is very probably due to the fact that the RWM-Iso model is not capable to account for anisotropy of the flow induced by shear gradient effects.

Comparison of RWM-Aniso PLM in steady and unsteady mode:
In case of steady coupling, the results were comparable with the unsteady coupling. So in this section only results for unsteady coupling will be discussed. The results for The modification of RWM-Iso to RWM-Aniso improves the results to some extent but still unfortunate disagreements with experimental data can be observed (see Figure 7.15). At this point, it might be interesting to note that the RWM-Aniso model indicates some instability especially in the regions with high degree of unsteadiness ($x = 700mm$ and $x = 1200mm$) as may be seen in figures 7.17for the mean concentration of the particles. This may reveal that this model is not capable to capture the essential dynamics of complex flows.

Comparison of mean particle concentration for RWM-Iso, RWM-Aniso and PLM:
Let us first quantify the Stokes number along with the importance of the investigated dispersion process. In the absence of electrostatic and thermophoretic forces, the deposition of small particles

depends mainly on particle Stokes number (see [129]). The Stokes number for the particle is defined as the ratio of the particle response time, τ_p, to the turbulence typical Lagrangian time scale τ_l. In the present study in cases X_3 and X_4 this quantity lies in range of (0, 0.5). Therefore the use of dispersion modeling is revealed to be very important for the current configuration as pointed also by Fede et al. (2006). It is then of interest to highlight the presence of preferential concentration which is known to be caused mainly by dispersion process. Figures 10 and 7.16 show a comparison of results obtained with three dispersion models with respect to the prediction of the particle concentration. Figure 10 displays a qualitative comparison showing a large spread of particle concentration once RMW-Aniso is used and a more concentrated distribution with RMW-Iso and PLM. The quantitative results in figure 7.16 indicate that RWM is capable to deal with the present geometry and deliver comparable results with PLM at all three positions. In contrast to that, RWM-Aniso is not stable especially in regions with higher degree of instability (see also non realistic spreading in figure 7.17). This may reveal again that the modifications in RWM-Iso are not appropriate for really complex flows.

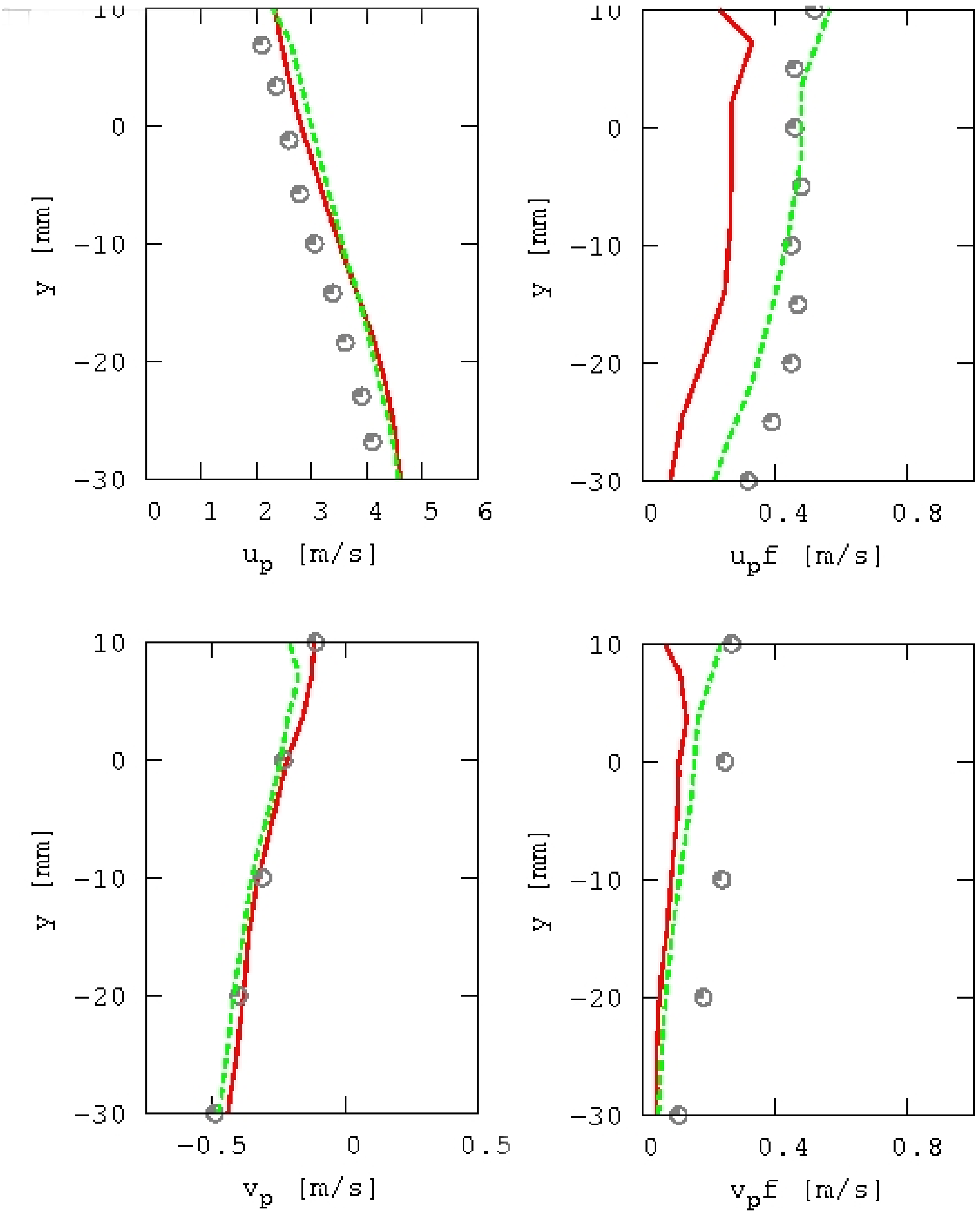

Figure 7.13: Mean particle velocity and fluctuation at x=300mm, Comparison of cases X_1 and X_2. Dots (exp), red solid lines (RWM-Iso) and green dashed lines the PLM calculations, both in steady mode.

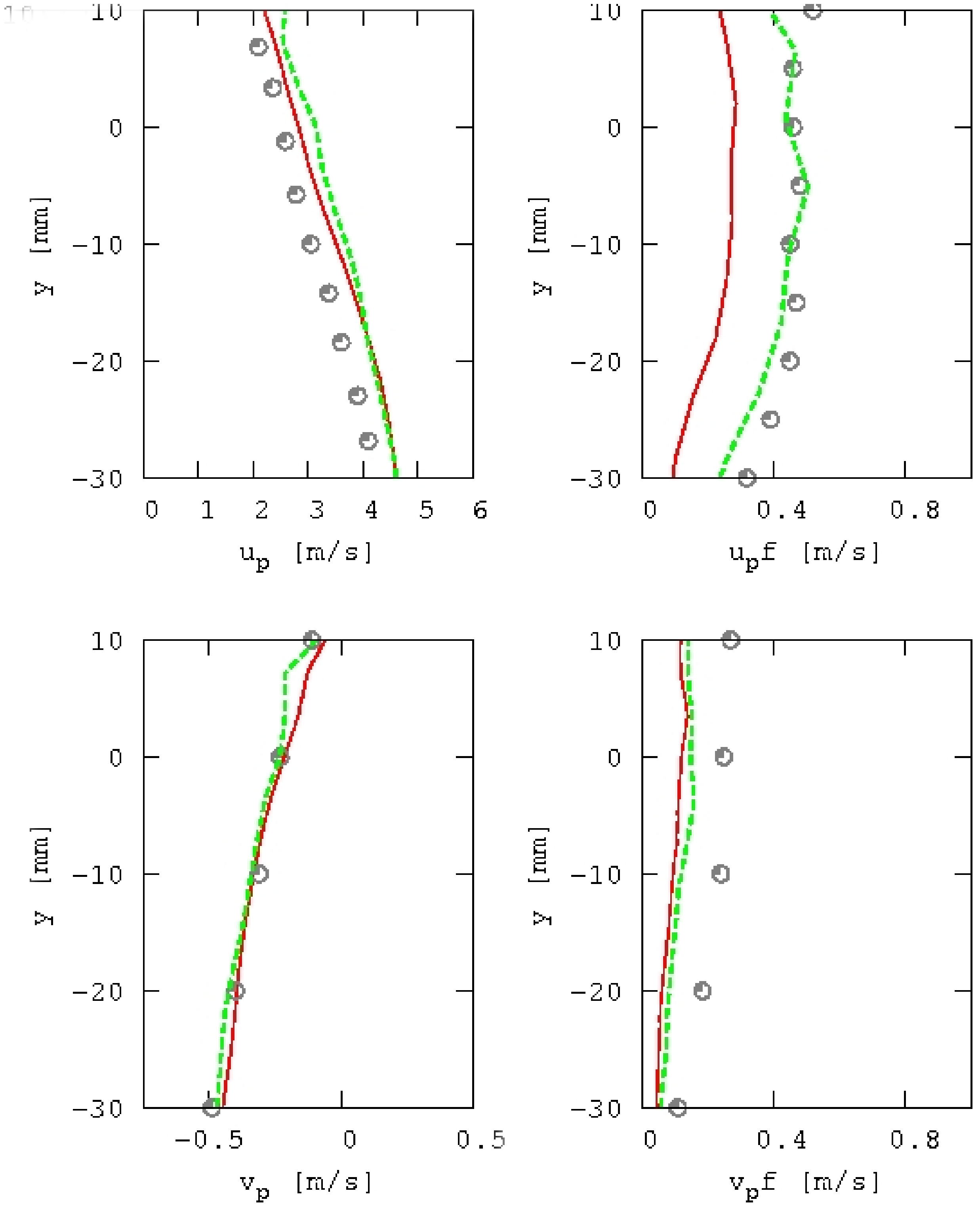

Figure 7.14: Mean particle velocity and fluctuation at x=300mm, Comparison of cases X_3 and X_4. Dots (exp), solid lines (RWM-Iso) and dashed lines the PLM calculations, both in unsteady mode.

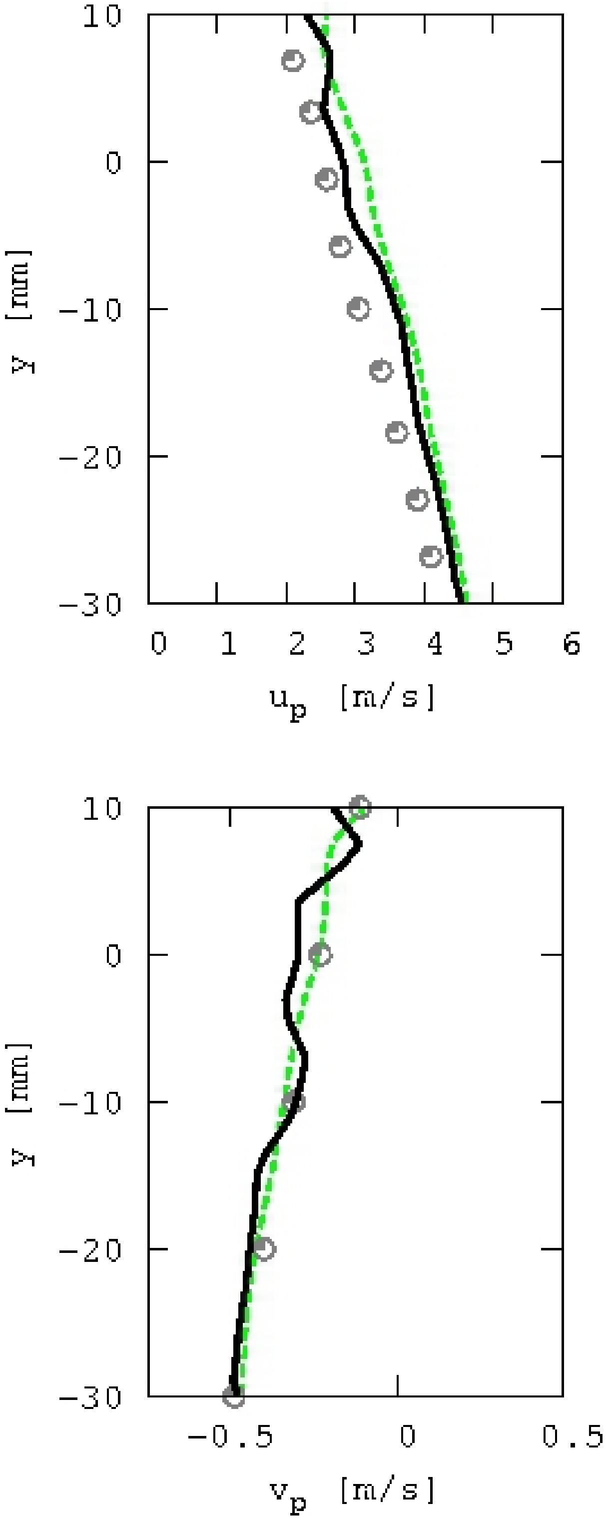

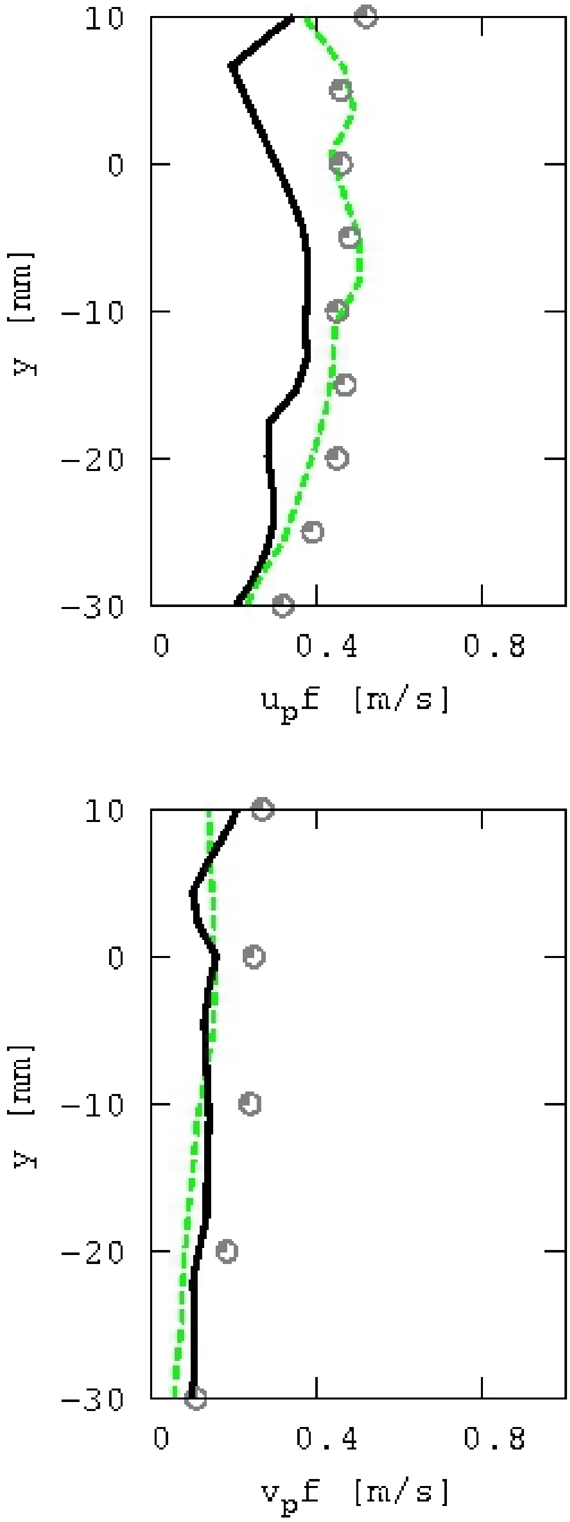

Figure 7.15: Mean particle velocity and fluctuation at x=300mm, Comparison of cases X_4 and X_6. Dots (exp), solid lines (RWM-Aniso) and dashed lines the PLM calculations, both in unsteady mode.

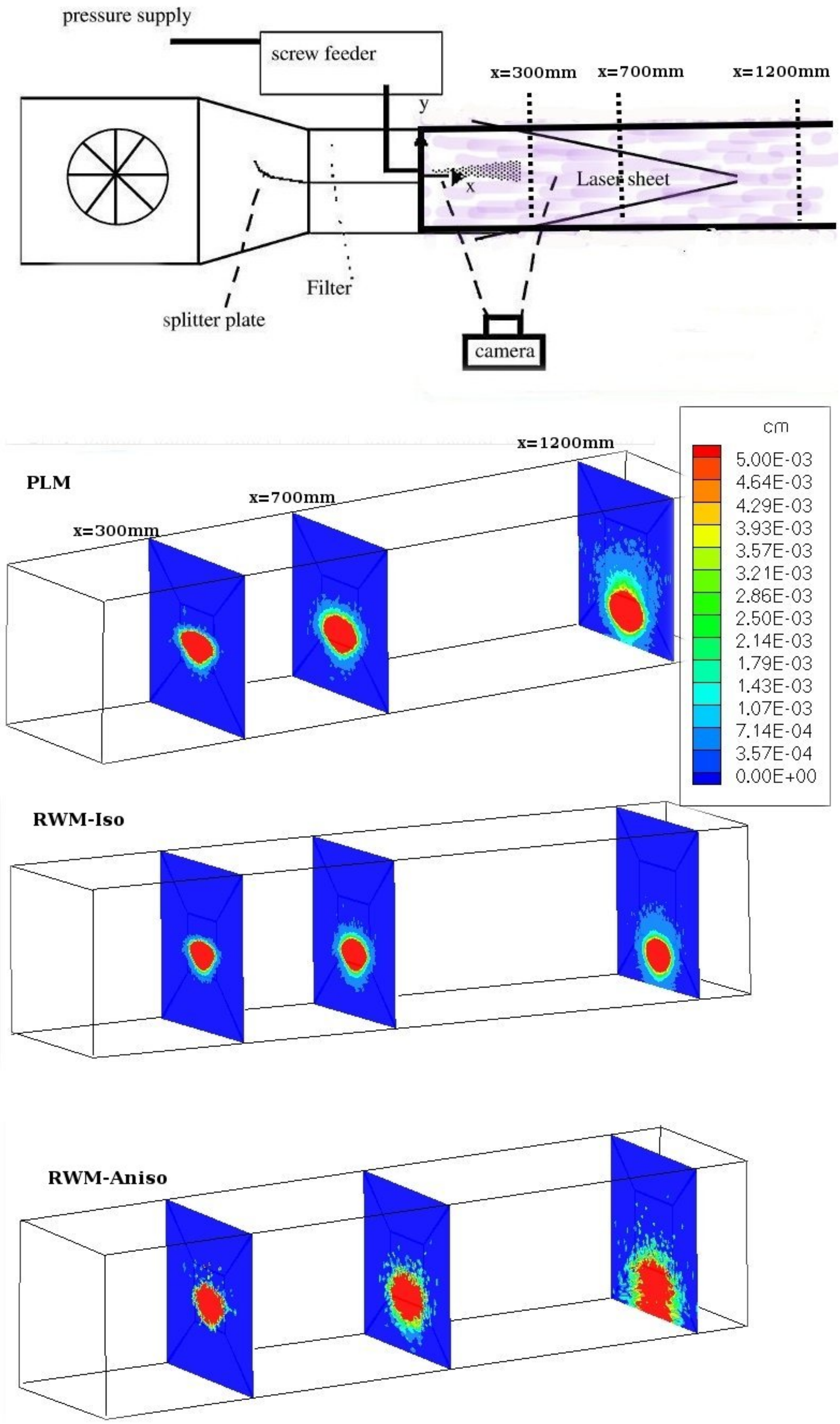

Figure 7.16: Concentration of particles predicted by various dispersion models at x=300mm, x=700mm and x=1200mm (cases X_3, X_4 and X_6)

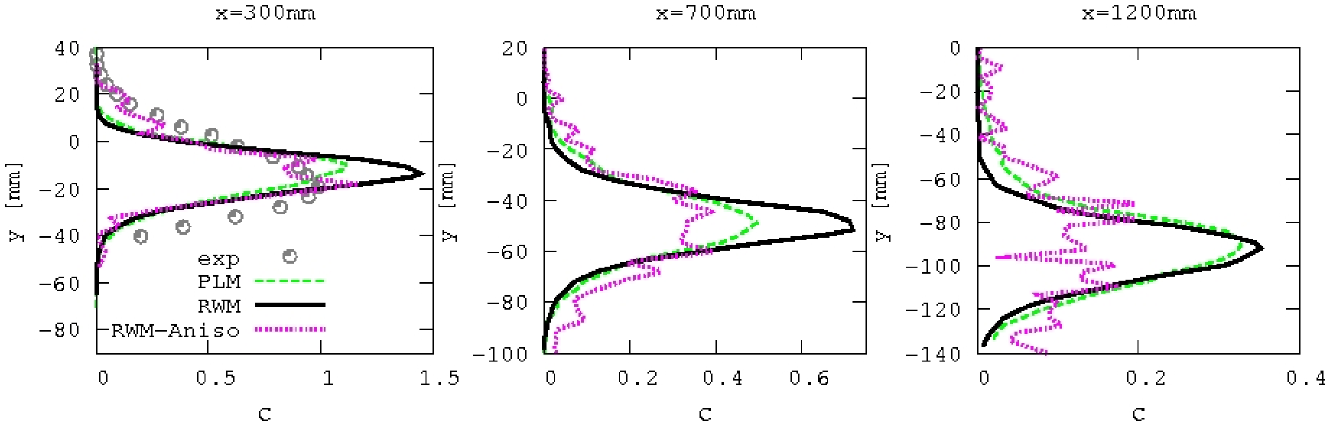

Figure 7.17: Mean concentration of particles c predicted by various dispersion models at x=300mm, x=700mm and x=1200mm (cases X_3, X_4 and X_6)

7.2.4 Conclusion

In order to appraise the quality prediction of dispersion models steady and unsteady coupling approaches have been applied to a particle laden shear flow simulation in RANS-context. For this purpose, three dispersion models, namely the isotropic Random Walk Model, the anisotropic Random Walk Model and the Particle Langevin Dispersion Model have been used. Their performances with respect to the particle velocity fluctuation and particle concentration have been compared for different simulation modes using the $k-\epsilon$ turbulence model to describe the turbulent carrier phase flow. Based on the results, following conclusions can be drown:

1. The use of a steady coupling while including a simple dispersion model such as Random Walk Model would not return reliable results.
2. Unsteady coupling approach with advanced dispersion model such as Particle Langevin Model and unsteady simulation of carrier phase seems to be able to capture the essential dynamics of the flow.
3. With respect to unsteady simulation methods like URANS, it might be essential to use an advanced dispersion model like Particle Langevin Model for better capturing dispersion process, where $\tau_p/\tau_l < 0.5$.
4. As the coupling between the dispersed and carrier phase is achieved in an Eulerian level, an averaging of representative sample of particle is required. If the sample size is too small, the statistical noises may decrease the results quality.
5. The effect of dispersion modeling on the segregation prediction has been pointed out confirming previous findings in Horender (2005). This effect suggests that advanced dispersion model on the fuel-air mixture preparation and related analysis is expected to be essential elucidating some contradictory claims in the literature with respect to the unsteady calculations, like LES, Senoner et al. (2009), Apte et al. (2009), Sommerfeld et al. (1998), Sanjose et al. (2005), Lederlin & Pitsch (2008).

8 Particle dispersion coupled to droplet phase change

In addition to the dispersion process the phase change process has also to be taken into account. After some test in 8.1, the model will be than validated in 8.2.

8.1 A simple test case for the validation of the evaporation model

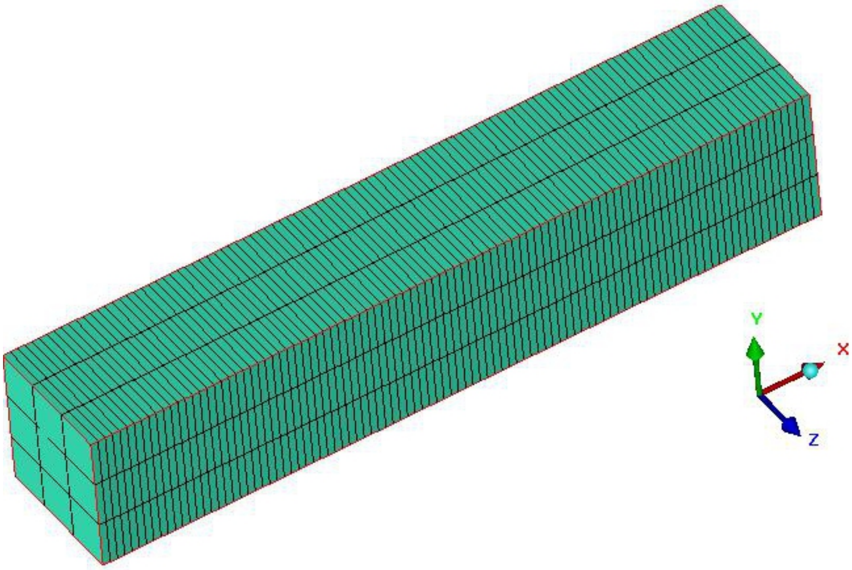

Figure 8.1: Test case for the verification of the evaporation model

Table 8.1: Properties of the gas phase

CV	U	V	W	T
200	1 m/s	0.0	0.0	370 K

To investigate the evaporation model and the flow property of the isopropanol-alcohol a simple test case was used. This test case is 1 m lang. The flow velocity and droplet velocity both were set equal along the channel to check the dependency of the droplets diameter along the channel length. The results were compared to the already implemented and validated model by Chrigui et al. [23]. Tables 8.1 and 8.2 include the properties for the channel flow configuration.

Table 8.2: Properties of the liquid phase

D_p	U_p	V_p	W_p	$\dot{m}_p$
$50 * 10^{-5}$	$1\ m/s$	0.0	0.0	$1 * 10^{-1}$kg/s

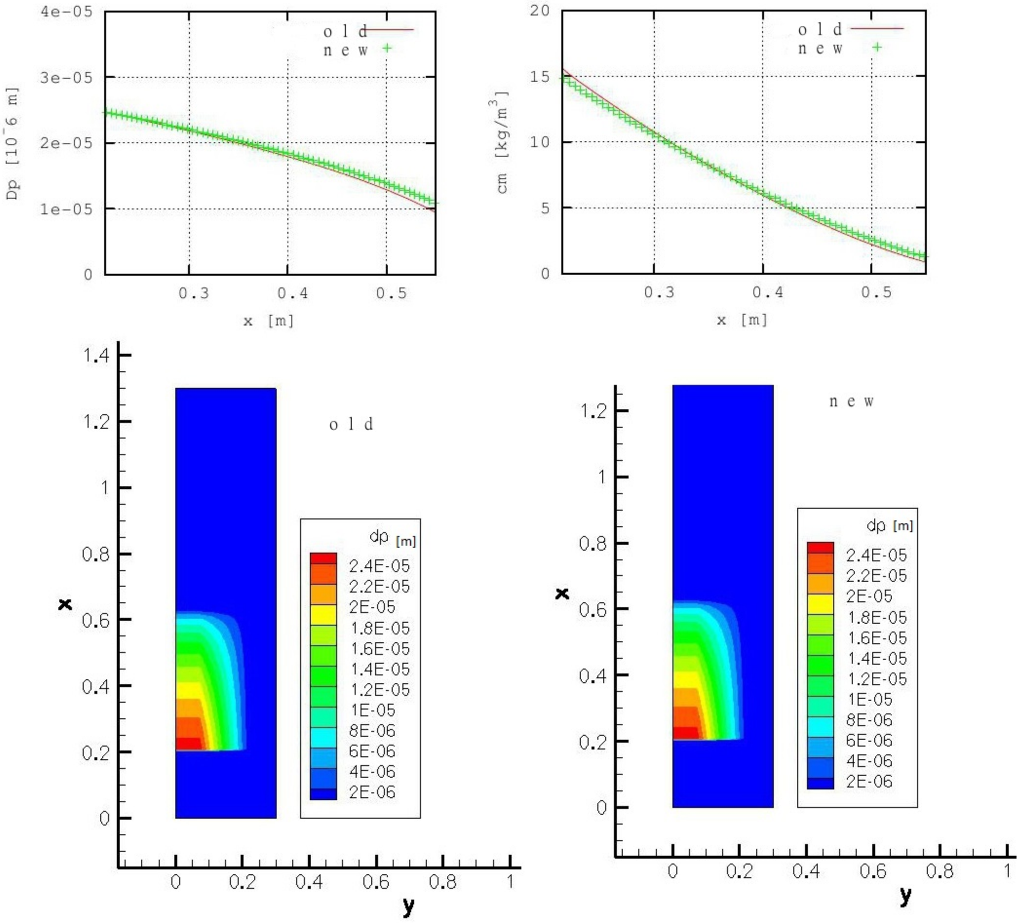

Figure 8.2: Comparison of the droplet diameter and mass concentration of the implemented evaporation model (new) to the already existing evaporation model (old)

To compare the results the evolution of the diameter and mass concentration of the droplets along the x-axis were compared. First the gas flow is calculated without including turbulence in steady mode until the convergence was reached. After the convergence of the gas flow only one droplet was tracked. In Figure the plots show that the diameter is getting smaller and the droplets diameter decrease. The same behavior can be seen for the mass concentration of the droplet. Since there is only one droplet so the average will be seen only in one control volume and this cause the non-symmetric of the droplet diameter on the plots.

8.2 Spray issuing into a co-flowing heated air stream

Simulations of two phase flows represented by a spray which is injected into a co-flowing heated air-stream are presented and discussed in this test case. The objective is to assess the ability of the (equilibrium) uniform temperature evaporation model coupled to different dispersion models, introduced above, to successfully predict the mass transfer, vapor and droplet spatial distributions. These numerical investigations are important in order to characterize the interaction regimes between processes that occur during evaporation, namely turbulence and heat transfer. These regimes govern the conditions for the fuel air mixing preparation.

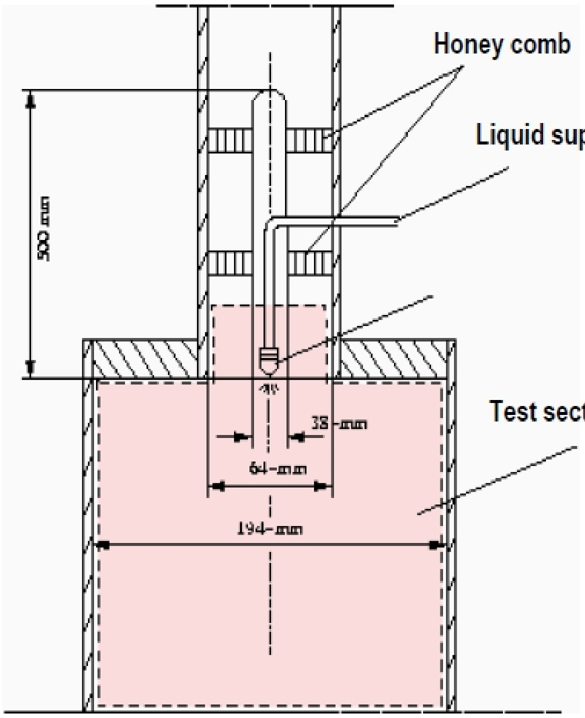

Figure 8.3: Test configuration for spray issuing into a co-flowing heated air-stream [26]

8.2.1 Configuration

The configuration under study is the experiments with polydisperse evaporating sprays reported by Sommerfeld et al. [26]. The experimental test case shows an axisymmetric, turbulent, two-phase jet. This configuration is consisted of a pipe with an expansion ratio of three, where heated air is injected through an annulus with $64mm$ outer diameter (see Figure 8.3). The nozzle holder had a size of $38mm$, and the test section had a diameter of $198mm$. A two-component phase Doppler anemometry (PDA) is used to measure droplet velocities and diameters simultaneously and to discriminate gas-phase tracers from the different size-classes of droplets. Due to its high evaporation rate an isopropanol-alcohol spray liquid was chosen. Measurements were taken for different flow conditions, such as air flow rate, droplet velocities, droplet diameter distribution and liquid flow rate in order to provide a set of reliable date. Measurements are available in six cross-sections downstream for droplets and carrier phase, namely at: $x = 25$, $x = 50$, $x = 100$, $x = 200$, $x = 300$ and $x = 400mm$. This experiment gives a valuable database of polydisperse two-phase flows since initial conditions are detailed for each droplet size class. The initial conditions are given at $3mm$ downstream due to measurement technique limitations.

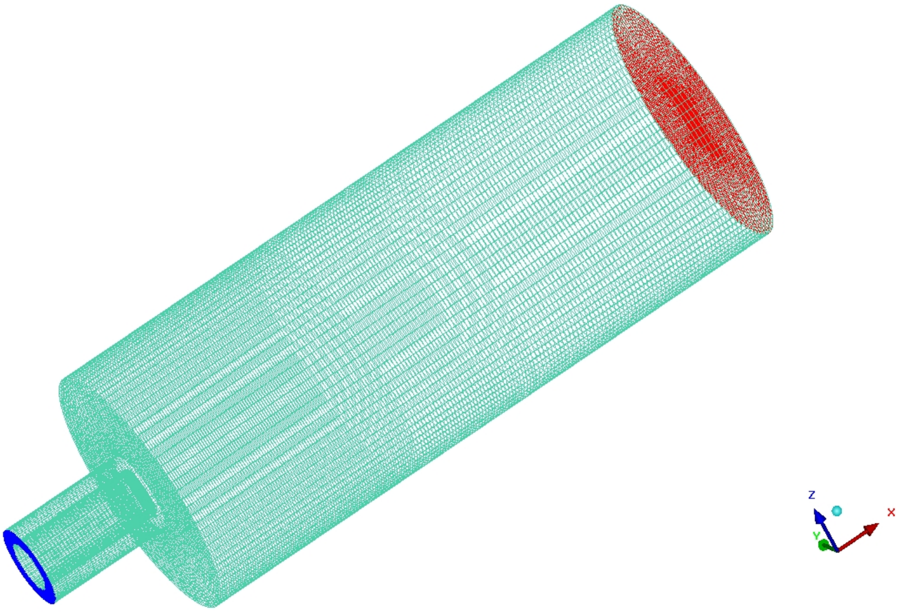

Figure 8.4: Mesh for the test configuration for spray issuing into a co-flowing heated air-stream

In order to assess the flow characteristics the first flow considered in the studies was a single phase flow case (i.e. liquid spray is not operated). In Table 8.3 the air flow conditions for the single phase are summarized .

8.2.2 Numerical setup

Grid independent solutions were obtained using enough refinements and central differencing scheme. The computational domain for the simulation was represented by a grid having almost $7 * 10^5$ control volume (see Figure 8.4). The heated air inters the configuration in x-direction the inlet with the constant velocity of $18m/s$ and $80C$.
The simulation is first performed in steady mode with k-ϵ for 3000 Iterations and the boundary condition for the turbulent kinetic energy is set to 5% of the mean flows inlet velocity. Then a SAS model is used. This practice leads to a good convergence behavior of the SAS-model. Then the simulation was changed to unsteady mode (with $\Delta t = 5 * 10^{-5}$s) and SAS-model was switched on.

For the two-phase flows, the inlet boundary conditions for the carrier phase are given in Table 8.3. For Validation purpose the measurements were performed $3mm$ downstream for all three velocity components as well as the associated rms values. More details on the test cases are provided by Sommerfeld et al. [26] in the inlet section for all carrier phase variables. 8 different classes of droplet can be generated by the hollow-cone pressure atomizer. These classes are distinguished by the droplet diameter, start velocities, start locations and rms values. the inlet properties for the different classes are given in Table 8.4. It should be mentioned here that, the mean tangential velocity of the droplet inflow during the simulation were set to zero (not conform to the experimental

Table 8.3: Flow conditions for the considered two phase flows

Cases	Air volume flow rate (g^3/s)	Air mass flow rate (g/s)	Maximum air velocity (m/s)	Air temperature (°C)	Liquid mass flow rate (g/s)	Liquid temperature at nozzle exit (°C)
1	0.032	29.0	18.0	80	0.00	0.0
2	0.032	29.0	18.0	80	0.44	32.0

Table 8.4: Flow conditions for the considered dispersed phase

z (mm)	flux $(g/m^2/s)$	size μm	Umean (m/s)	Urms (m/s)	Vmean (m/s)	Vrms (m/s)	Wmean (m/s)	Wrms (m/s)
0	88.6	18.10	7.698	3.307	0.508	1.452	-0.749	1.037
1	214.5	20.51	10.688	3.674	2.107	0.898	-0.434	0.829
2	952.5	28.22	14.386	3.021	5.054	1.225	-0.243	0.669
3	3080.7	36.54	16.017	2.442	7.785	1.248	-0.120	0.586
4	6321.3	44.61	15.93	2.022	9.766	1.530	-0.034	0.533
5	5664.5	47.47	14.295	2.126	8.740	3.443	-0.001	0.530
6	973.7	37.96	10.436	2.593	6.200	4.569	-0.095	0.606
7	95.0	27.98	6.178	2.835	2.303	3.530	-0.250	0.794

boundary conditions), since a spray nozzle without swirl was used and, therefore, the measured mean tangential velocity was due to disturbances from the flow at the edge of the nozzle exit. The Table 8.3 gives the total liquid mass flow rate and the inlet temperature at the nozzle exit. 100000 parcel trajectories are calculated every coupling iteration in order to get statistically reliable results. An increase of parcel number had no influences on the statistical droplets properties.

8.2.3 Results and discussions

It is very important to look first on the gas phase. Since the configuration under study is a high turbulent flow in addition to the turbulence induced through the inflows the inner and outside shear layer provide some more turbulence intensity. The eddies induced through the shear layer lead to the growth of the turbulent length scale.

The comparison to the experiments are shown in Figure 8.5, where axial mean velocity (top), axial RMS values of velocity (middle) and radial mean velocity (bottom) of the gas-phase along the test section are confronted with experimental data. Generally the agreement to the experimental data is well for regarding the axial velocity. Furthermore one can see that the model predicts the radial component, which is normally very difficult to capture due to its low values. The comparison of

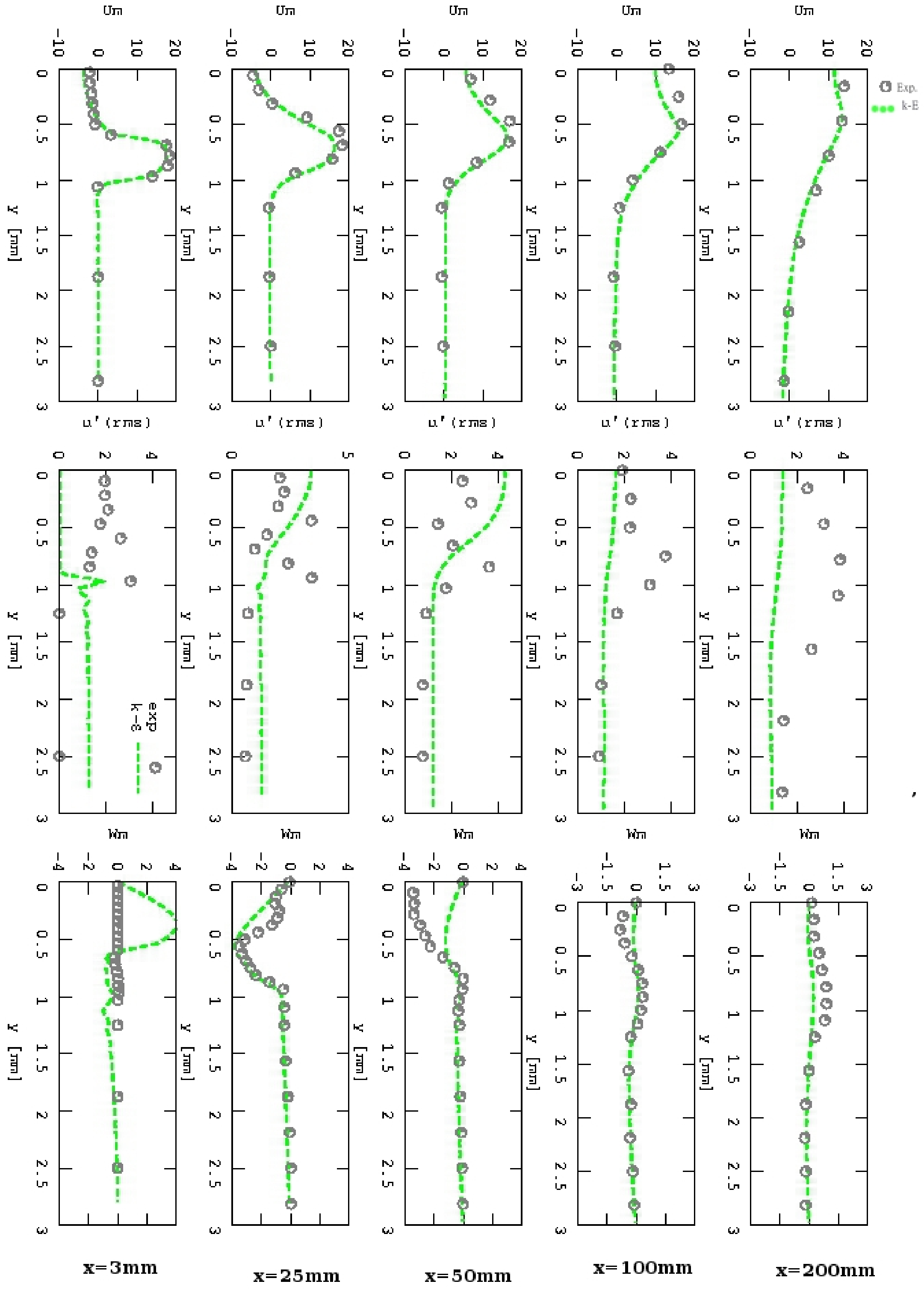

Figure 8.5: Cross sectional distributions of (top) axial mean velocity, (middle) axial RMS values of velocity and (bottom) radial mean velocity of the gas-phase along the test section using the k-ϵ model

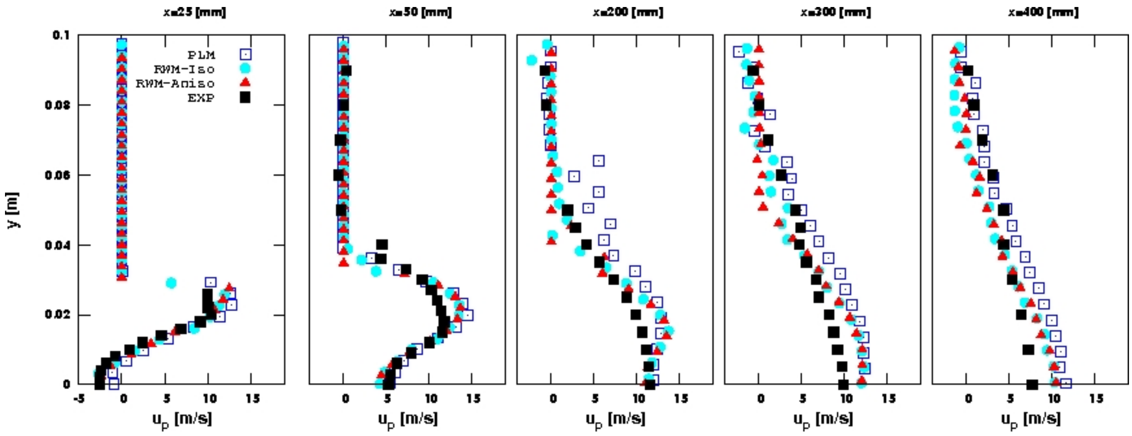

Figure 8.6: Cross-sectional distributions of axial mean velocities of droplets along the test section

the first section regarding the experimental data shows that the k-ϵ model is not able to predict the rms values very well.

For the k-ϵ model an almost steady solution was reached after almost 16000 time steps. Since the resolved rms values of the k-ϵ model were very low only $1/3$ of the turbulent kinetic energy was taken for comparison to the experimental data.

Focusing now on two-phase flow, the three dispersion models, PLM (Particle Langevin Dispersion model), RWM-Iso (Isotropic Random Walk model) and RWM-Aniso (Anisotropic Random Walk model) are used to determine the instantaneous fluid velocity seen by the droplet in the presence of evaporation.

First, the capability of the Lagrangian tracking approach to capture the dynamic droplet behavior is evaluated by comparing the calculated droplet velocities with experimental data. The velocities in axial direction are plotted in Figure 8.6 as function of radial positions at different axial positions. One observes some differences between experimental and numerical results. In particular, at $x = 300mm$ and $x = 400mm$ the computed droplet axial velocities are about $2m/s$ higher at the centerline than the measured values. However, it is remarkable that the choice of dispersion model does not influence too much the numerical droplet axial velocities. Whereas some advancement are seen by PLM model especially outside of the centerline.

Figure 8.7 shows the radial droplet velocity at different axial cross sections. It is seen that the effects of the small recirculation zones are reflected in the first two cross sections downstream of the inlet where negative radial velocities can be observed. The influence of the drift correction factor (RWM) on the droplet radial velocities is only not seen at the first axial section. The radial mean velocity of the droplets decreases when moving away from the nozzle inlet by the RWM. The RWM-Aniso improve the results, whereas the PLM capture the radial velocity very well. The Comparison of the numerical and experimental results of the radial mean velocities show that the radial position of the spray is not well reproduced at the first two positions downstream of the nozzle. The deviations from the experiment may lie in initial conditions of droplets at the nozzle exit such as the radial velocity and positions which were very difficult to be extracted from the experimental data.

In Figure 8.8 the radial distribution of the mean droplet diameter is shown at different axial positions (x= 25, 50, 200, 300 and $400mm$) which were close to inlet, center and outlet regions. Due to the evaporation and spreading of the droplets, the mean diameter becomes more uniform when

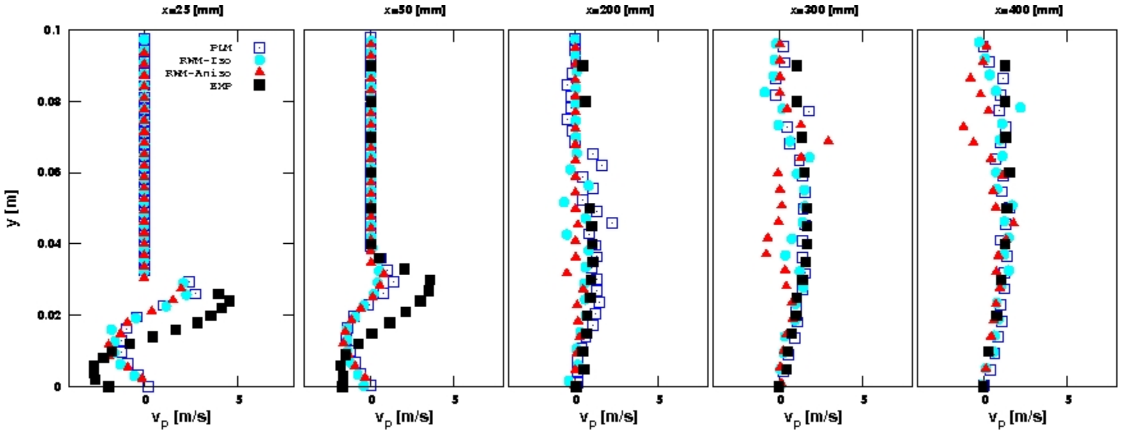

Figure 8.7: Cross-sectional distributions of radial mean velocities of droplets along the test section

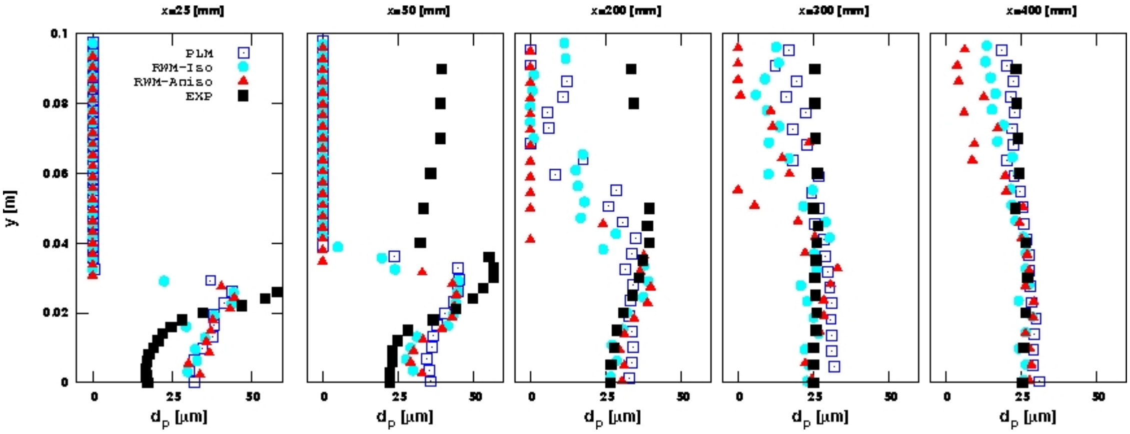

Figure 8.8: Cross-sectional distributions of axial mean diameter of the droplets along the test section

moving away from the inlet nozzle. The droplet diameter decreases while moving downstream of the nozzle exit. At sections of x$=25$ and 50 one observes a zero mean diameter (radius > $0.03m$) while including fluctuating diameter for the sections x$=200$ and $300mm$. This lies on the fact that no droplets or very less droplets are registered within the control volumes. This lead in case of less droplets to a fluctuating variable fields of the statistical averaging (see Figure 8.8 x$=200$, 300 and $400mm$).

Th axial mean values (RMS) of the droplet velocity is shown in Figure 8.9. Based on the results, it can be concluded that the RWM-Iso underpredict the particle fluctuations, which might be due to the fact that the RWM-Iso is not capable to account for anisotropy of the flow induced by shear gradient effects. The RWM-Aniso improves the results to some degree but still some disagreements with experimental data can be observed (see Figure 8.9 x $=50mm$ and x $=200mm$). For x $=25mm$ the PLM results overpredict the fluctuation, whereas x $=50mm$ and x $=200mm$ are predicted very well. The sections x $=300mm$ and x $=400mm$ are characterized by a fluctuating variable field which is due to wider spreading of droplets by PLM and the statistical averaging.

The radial distribution of the droplet mass flux at different axial positions ($0.025m$, $0.05m$, $0.1m$, $0.2m$, $0.3m$ and $0.4m$ far away from the inlet) are presented in Figure 8.10. It is well seen, that the concentration of droplets decreases while moving away from the nozzle due to the evaporation. This fact is illustrated by all three dispersion models (RWM, RWM-Aniso and PLM). A compari-

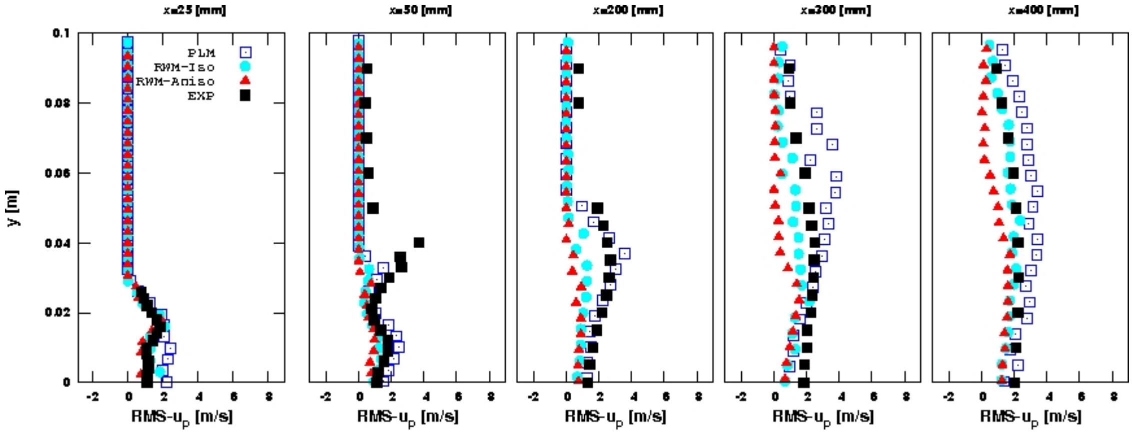

Figure 8.9: Cross-sectional distributions of axial mean velocity fluctuations of droplets along the test section

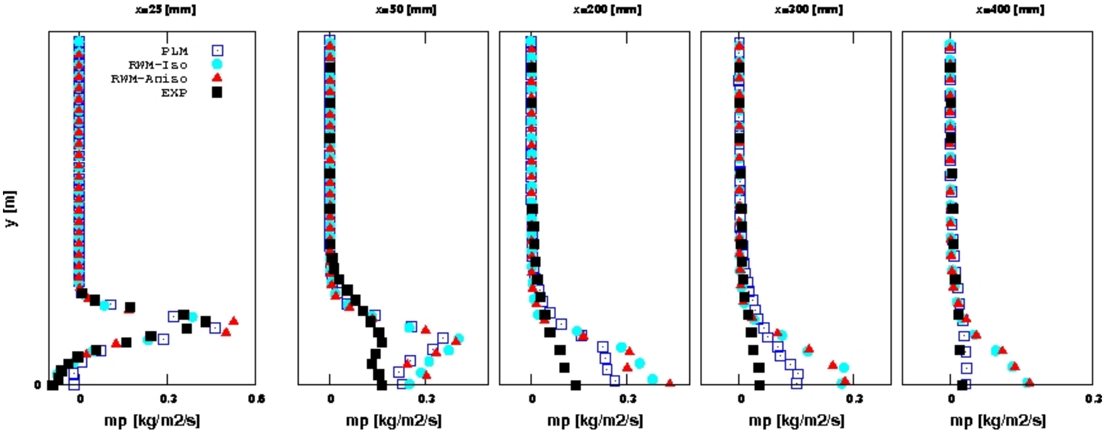

Figure 8.10: Cross-sectional distributions of the droplet-mass flux along the chamber

son between these models reveals that the PLM delivers results much closer to experimental results and especially far away from the nozzle. In the absence of thermophoretic forces, the deposition of small particles depends mainly on particle Stokes number (see [129]). The Stokes number for the particle is defined as the ratio of the particle response time, τ_p, to the turbulence typical Lagrangian time scale τ_l. In the present study, in which the thermophoretic effect is low, this quantity lies in the range of $(0, 0.5)$ making the use of dispersion modeling very important for the current configuration according to P. Fede et al. [44].

8.2.4 Comparison of k-ϵ and SAS models

Note that the gas phase calculation is very important for the subsequent particle calculation. AS turbulence closure in URANS-context should be used that captures the unsteadiness better. A first attempt has been done by implementing the scale adaptive simulation (SAS) model. In the following the k-ϵ and the new implemented SAS model in the FASTEST-Solver are compared.

Figure 8.11 shows the instantaneous picture of the axial velocity of fluid phase for the SAS (top) and k-ϵ model (bottom). The turbulent nature of the flow is very well seen by the SAS model, whereas the k-ϵ model shows a strongly converged solution. A close look at the SAS picture 8.11

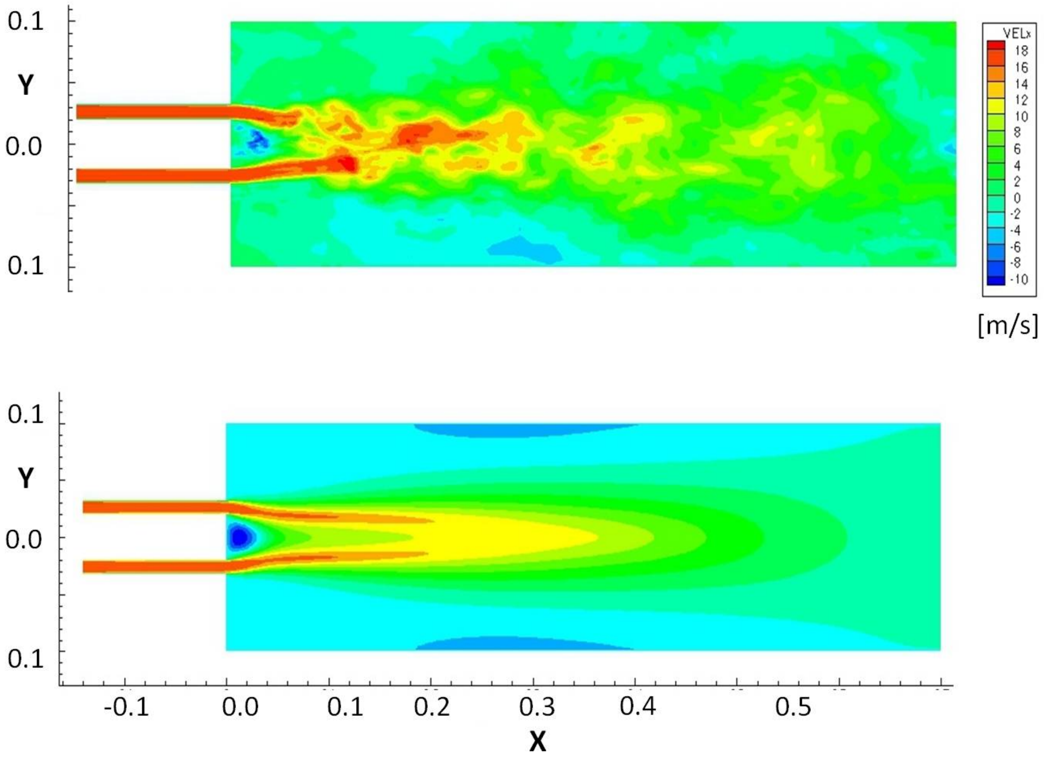

Figure 8.11: Instantaneous picture of the axial velocity of fluid phase for the SAS (top) and k-ϵ (bottom). two dimensional cut through the symmetry axis

gives an impact of the captured scales. The big scales that are very important for the unsteady evolution of the droplet are well captured.

The comparison to the experiments are shown in Figure 8.12, where axial mean velocity (top), axial RMS values of velocity (middle) and radial mean velocity (bottom) of the gas-phase along the test section are confronted with experimental data. Generally the agreement to the experimental data is well for both models regarding the axial velocity. Furthermore one can see that the SAS model is able to predict the radial component very well compared to the k-ϵ model, which is normally very difficult to capture due to its low values. The comparison of the first section regarding the rms values shows that the k-ϵ model is not able to predict the rms values in this section, whereas the SAS model is able to reproduce the trend of the rms values in the high unsteady area while achieving a satisfactory agreement away from this area. The results are getting better the more one goes away from the pipe inlet.

The rms values of the velocity in x-direction is very well captured by the SAS model. This ensures that the the energy is successfully transferred from the modeled to the resolved part and the spectral distribution improves with time as the process is controlled by the momentum equations and the eddy-viscosity provided by the SAS model. The coupling of the SAS model to a Lagrangian tracking is expected to deliver better results than using k–ϵ. Unfortunately this task could not be achieved in the time frame of this work.

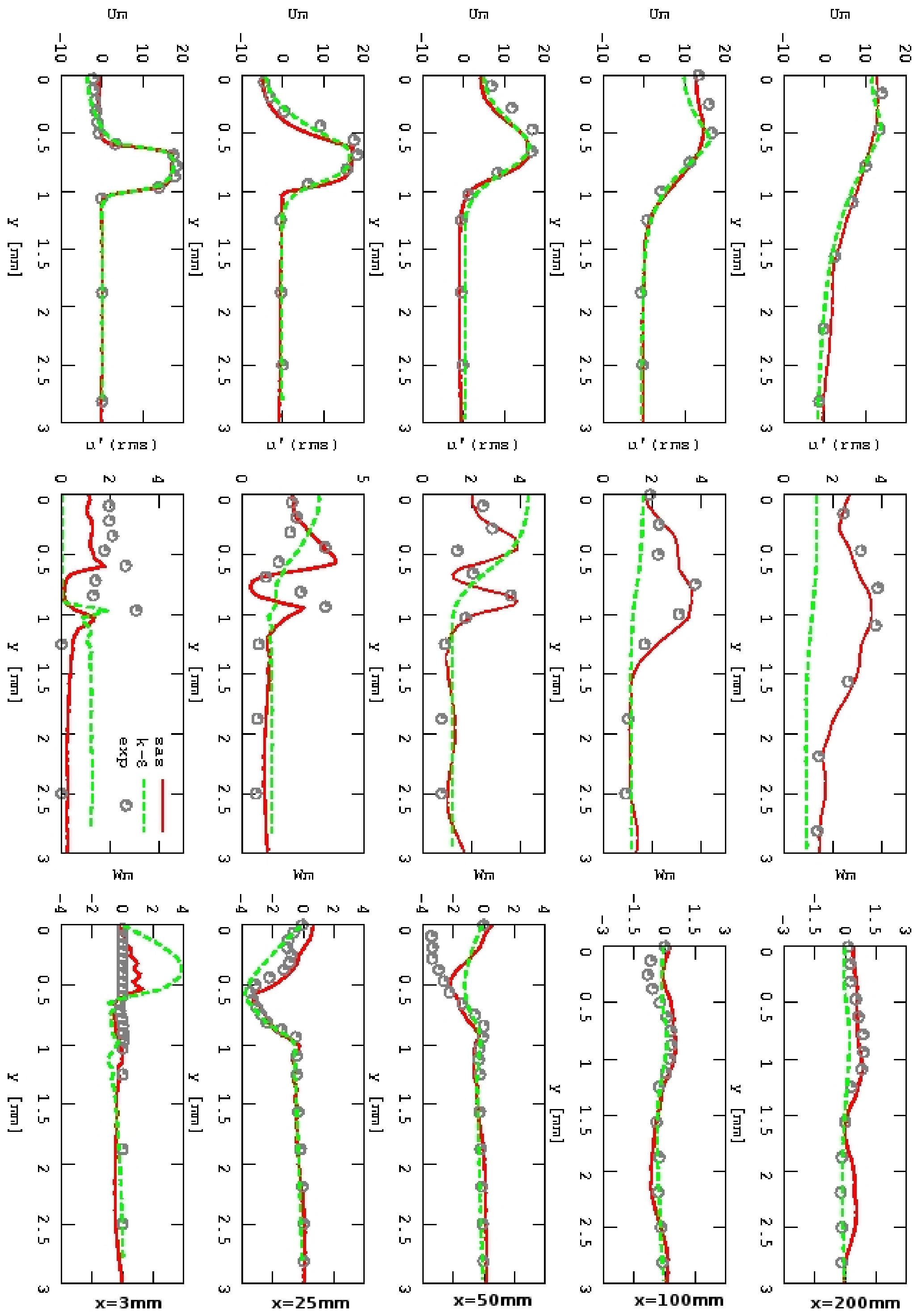

Figure 8.12: Cross sectional distributions of (top) axial mean velocity, (middle) axial RMS values of velocity and (bottom) radial mean velocity of the gas-phase along the test section

8.2.5 Conclusion

In this section different dispersion models were used in combinations with the uniform temperature evaporation model to investigate the spray and droplet properties under non isothermal and non reacting conditions. The results show that the PLM is able to achieve better results with respect to radial mean velocities, mean diameter and axial mean velocity fluctuations of droplets. So the simulations have shown that the PLM model agreed very well with the experimental measurement of the droplet mass flux in particular in upper sections. This means that the consideration of an advanced dispersion model like PLM accounts well for anisotropic turbulence and vortex structures inherent to complex turbulent two phase flows.

In regard to the used turbulence models one can say that the agreement to the experimental data is well for both models regarding the axial velocity. The radial component is reproduced by SAS model very well compared to the k-ϵ model, which is normally very difficult to capture due to its low values. Rms values with SAS are in a satisfactory agreement away from the inlet.

The rms values of the velocity in x-direction is very well captured by the SAS model.

The coupling of the SAS model to the dispersed phase is still work in progress, so that the next step is to compare the two phase flow results for k-ϵ model and SAS model.

9 Particle dispersion coupled to breakup process

This section deals with the impact of the breakup of liquid drops on the dispersion of droplets using the Kolmogorov's scenario of breakup as described in section 5.1.2. For this purpose, a test case representing an experiment on air-blast atomization at atmospheric pressure is used.

9.1 Air-blast Configuration

A schematic of the injector is shown in Figure 9.1. The inlet parameters for the configuration are used from the experiment on air-blast atomization at atmospheric pressure [106]. In this experiment a round jet of water goes from the central tube ($D_l = 1.8mm$) at low velocity and atomizes by a parallel flow of air, which is issued at high velocity from an annular duct ($D_l = 3.4mm$). To evaluate the far field of a round water jet atomized by a high speed annular air jet, a series of measurements of the Sauter mean diameter was provided by Lasheras et al. [53],[101]. In this experiment, the nozzle diameters of water and annular air jets are $D_l = 3.5mm$ and $D_g = 5.6mm$, respectively. The measurements were taken at the constant gas velocity while varying the velocity of water. The computation of spray in the given geometry [101] was performed; the downstream variation of the Sauter mean diameter, D_{32} , at the given section was compared to the measurements.

On the numerical side 10000 particle were sufficient and were used for the simulation. The average of 10 simulation were compared to the experimental data. The diameter were recorded for 10 seconds in 7 sections and the average was taken for comparison. To ensure the grid independency the simulation were carried out with three different grid resolution.A standard k-ϵ model is used for the turbulence closure. The used three different grids have $1 * 10^5 CV$, $3 * 10^5 CV$ and $9 * 10^5 CV$. Fig. 9.2 exemplary shows a computational domain for an air-blast atomizer. According to the results there is a high dependency of the Kolmogorov's breakup model from the grid resolution. So the grid with $1*10^5 CV$ gives the worst and the grid with $9*10^5 CV$ the best results compared to the experimental data. Therefore all the simulation are carried out with the finest grid, $9 * 10^5 CV$. Table 9.1 give a short summary of the investigated cases.

9.2 Results and Discussion

9.2.1 Qualitative Results

The spatial distributions of blobs in Fig. 9.3 and its zooming in Fig.9.4 show that a broad spectrum of droplet size is presented at each spray location, which include large as well as small droplets.

Table 9.1: Different Model combinations used

Konfig.	$\dot{m}_{liq}$	Dispersion model	$\dot{m}_{air}$	Grid	Konfig.	Collision
Konfig-1	0.8m/s	RWM-Iso	115 m/s	$9*10^5$ CV	$d_i = 1.8\ d_a = 3.4$	No
Konfig-2	0.13m/s	RWM-Iso	140 m/s	$1*10^5$ CV	$d_i = 3.5\ d_a = 5.6$	No
Konfig-2	0.13m/s	RWM-Iso	140 m/s	$3*10^5$ CV	$d_i = 3.5\ d_a = 5.6$	No
Konfig-2	0.13m/s	RWM-Iso	140 m/s	$9*10^5$ CV	$d_i = 3.5\ d_a = 5.6$	No
Konfig-2	0.31m/s	RWM-Iso	140 m/s	$9*10^5$ CV	$d_i = 3.5\ d_a = 5.6$	No
Konfig-2	0.55m/s	RWM-Iso	140 m/s	$9*10^5$ CV	$d_i = 3.5\ d_a = 5.6$	No
Konfig-2	0.13m/s	RWM-Iso	140 m/s	$9*10^5$ CV	$d_i = 3.5\ d_a = 5.6$	yes
Konfig-2	0.31m/s	RWM-Iso	140 m/s	$9*10^5$ CV	$d_i = 3.5\ d_a = 5.6$	yes
Konfig-2	0.55m/s	RWM-Iso	140 m/s	$9*10^5$ CV	$d_i = 3.5\ d_a = 5.6$	yes

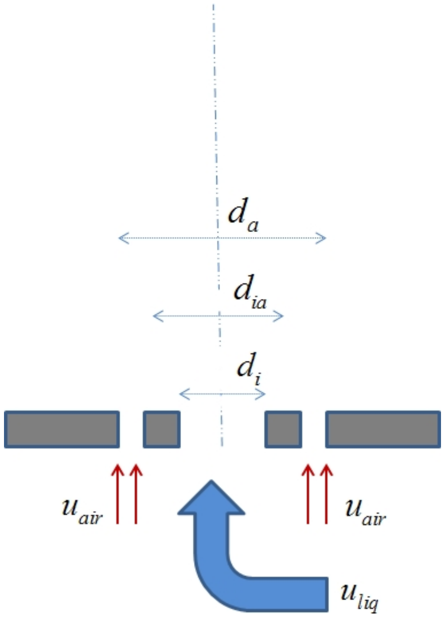

Figure 9.1: Coaxial jet nozzle configuration

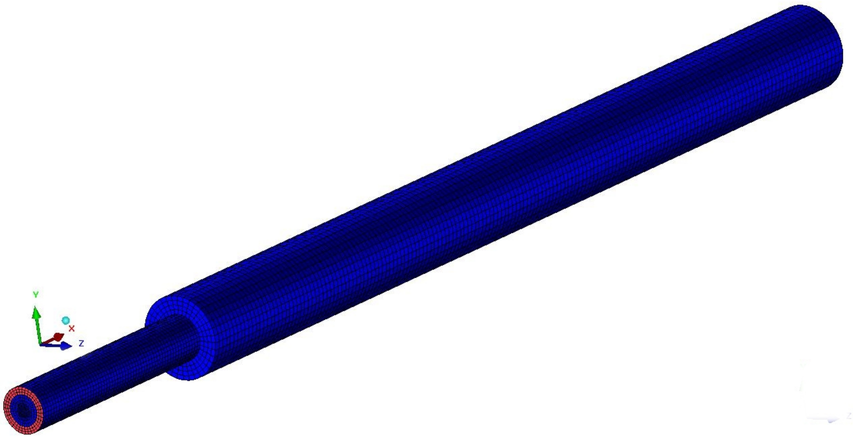

Figure 9.2: Computational domain with $9 * 10^5$ CV

By reason of experimental technique, which is not accessible to measurements of size distribution in the near-nozzle region, these numerical distributions can be assessed only qualitatively. The distributions of droplets near to the injector orifice are mostly large unbroken drops, which have the size of injector orifice but including also small droplets. It can be also seen that little far away from the injector the droplets which are the size of the injector orifice get down to smaller droplets.

9.2.2 Quantitative Results

The comparison is shown for three different liquid flow rates: $U_liq = 0.13m/s$; $0.31m/s$; $0.55m/s$, and for the gaseous rate $U_g = 140m/s$. It is seen that computed values of D_{32} are in general agreement with the experiment. The non-monotonic dependency of D_{32} on x/D_g , first decreasing (region dominant by breakup) and then increasing (region dominant by coalescence), was observed [101]. Such behavior can also be seen from the computations.

The simulation were carried out at the beginning without coalescence model 9.7 and than with coalescence model 9.7. A first look on the results show that there is no impact of coalescence on the breakup model.

It seems that the use of Breakup model with the coalescence perform slightly better results (see Fig. 9.8-9.10). However, in contrast to the previous results [104] the new implemented kolmogorov's model shows quite better results which certainly do not confirm the conclusion in [101] about a significant role of coalescence effects. According to the results achieved in this work one may conclude, that the effect of coalescence can be seen in all region of the configuration, which is not so strong as reported by [104].

The impact of dispersion model on the breakup was compared at centerline which was not very high for the sauter diameter. Other data for the comparison of dispersion models were not available for the current configuration.

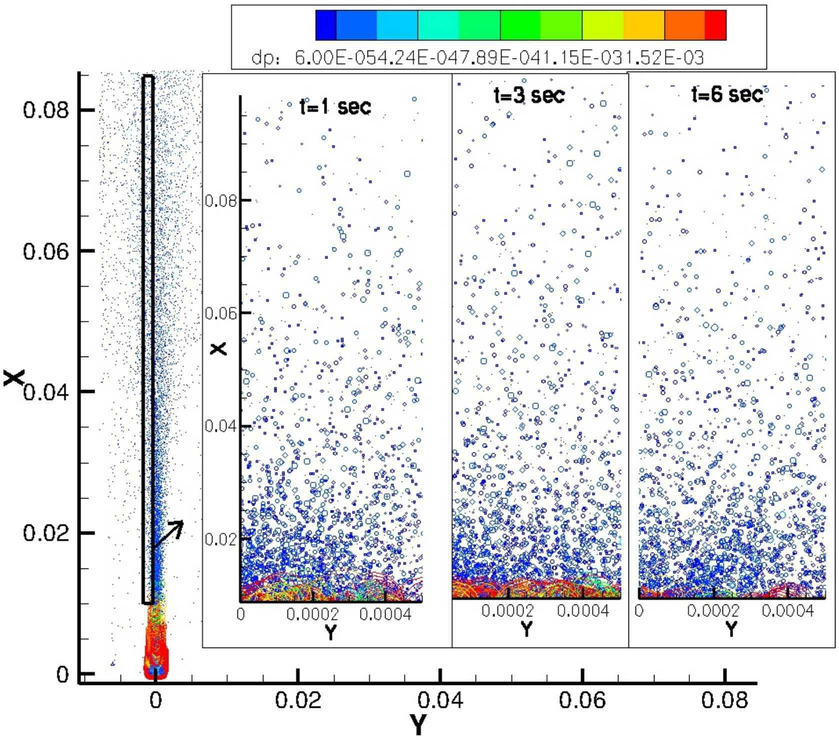

Figure 9.3: Computed spatial distributions of drops at different time in the spray of water atomizing by the coaxial air jet ($U_{liq} = 0.8 m/s$, $U_g = 115 m/s$). The ratio of gas-to-liquid momentum at the exit of injector is equal to 26.4. The vertical lines are given in m.

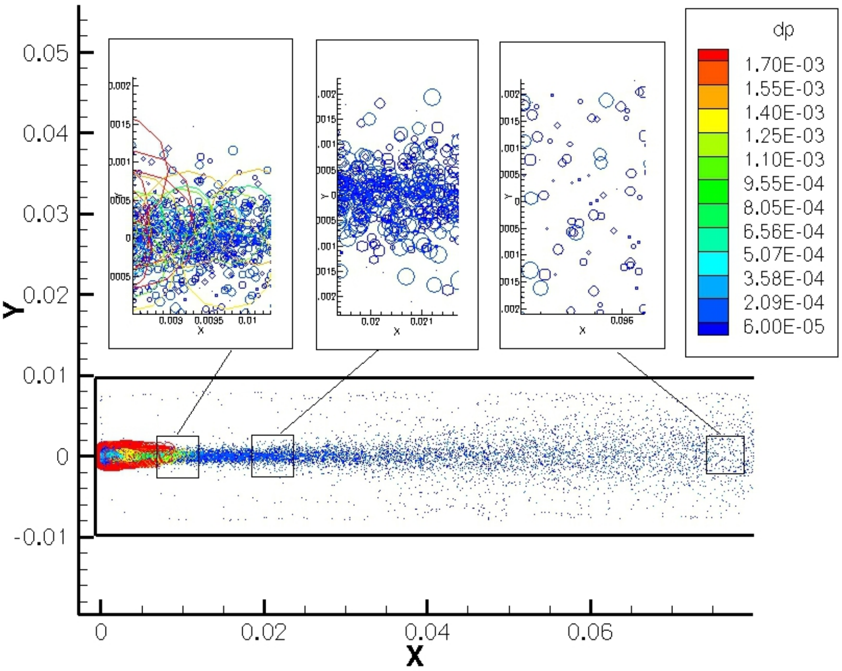

Figure 9.4: An example of zooming of spatial distributions of drops in the spray presented in Fig.9.3. A co-existence of droplets of different size is seen at every region of spray

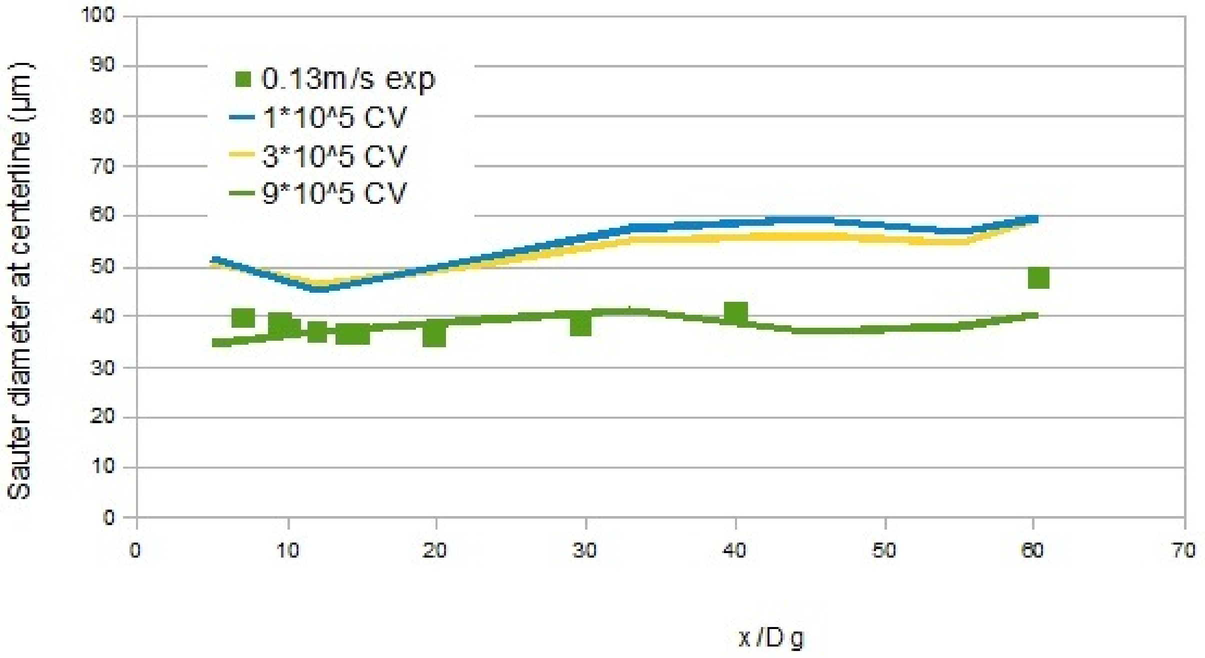

Figure 9.5: Comparison of the Sauter mean diameter at the given section with measurements in Refs. [53] and [103] in the far-field of a round water jet atomized by a high speed annular air jet. The measurements and computations without coalescence model are presented by symbols, $1{*}10^5 CV$ blue, $3{*}10^5 CV$ yellow and $9{*}10^5 CV$ green. The gas velocity and water velocity is held constant ($D_g = 5.6mm$, $U_g = 140m/s$), $U_{liq} = 0.13m/s$.

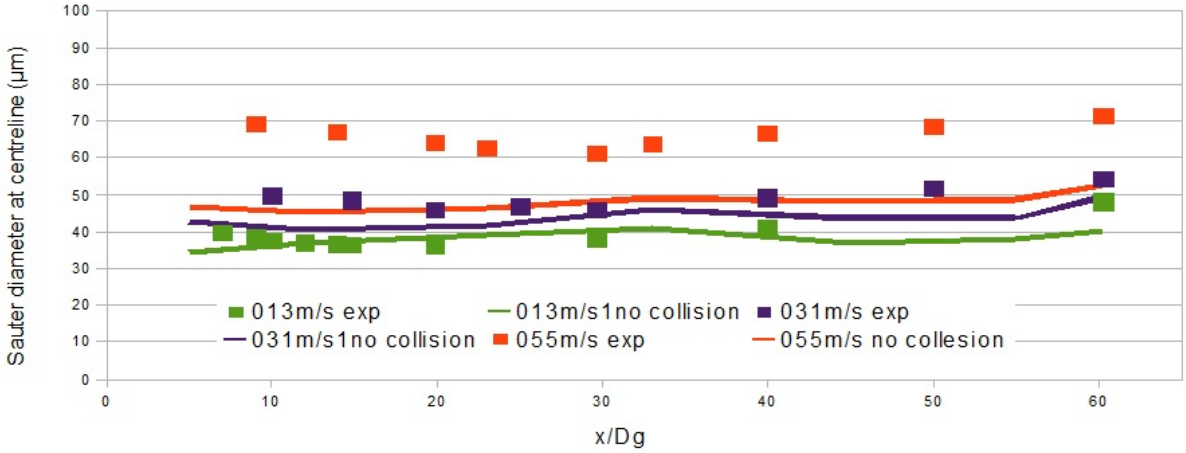

Figure 9.6: Comparison of the Sauter mean diameter at the given section with measurements in [53] and [103] in the far-field of a round water jet atomized by a high speed annular air jet. The measurements and computations without coalescence model are presented by symbols and continuous lines, correspondingly. The gas velocity is held constant ($D_g = 5.6mm$, $U_g = 140m/s$), while varying the velocity of water, $U_{liq} = 0.13; 0.31; 0.55m/s$.

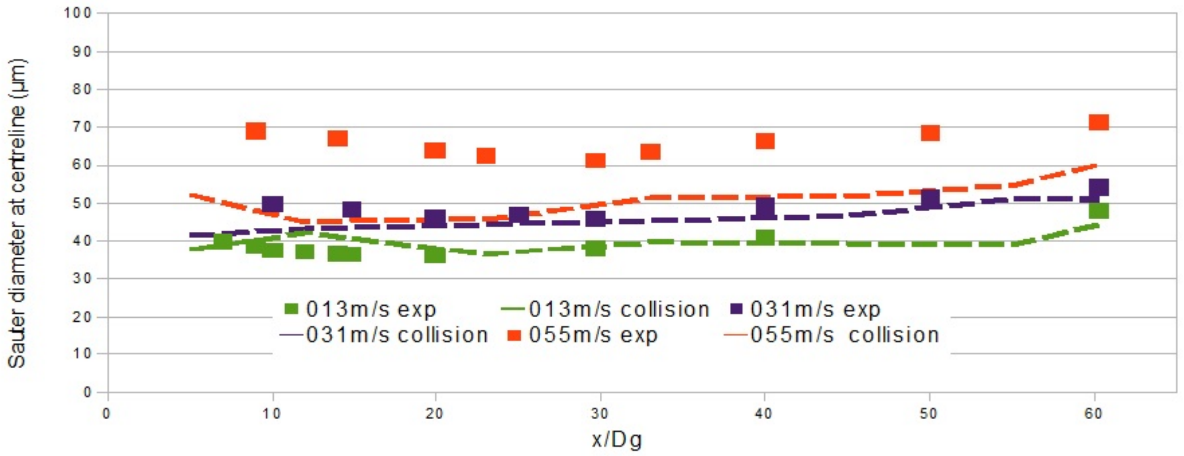

Figure 9.7: Comparison of the Sauter mean diameter at the given section with measurements in [53] and [103] in the far-field of a round water jet atomized by a high speed annular air jet. The measurements and computations without coalescence model are presented by symbols and discontinuous lines, correspondingly. The gas velocity is held constant ($D_g = 5.6mm$, $U_g = 140m/s$), while varying the velocity of water, $U_{liq} = 0.13; 0.31; 0.55m/s$.

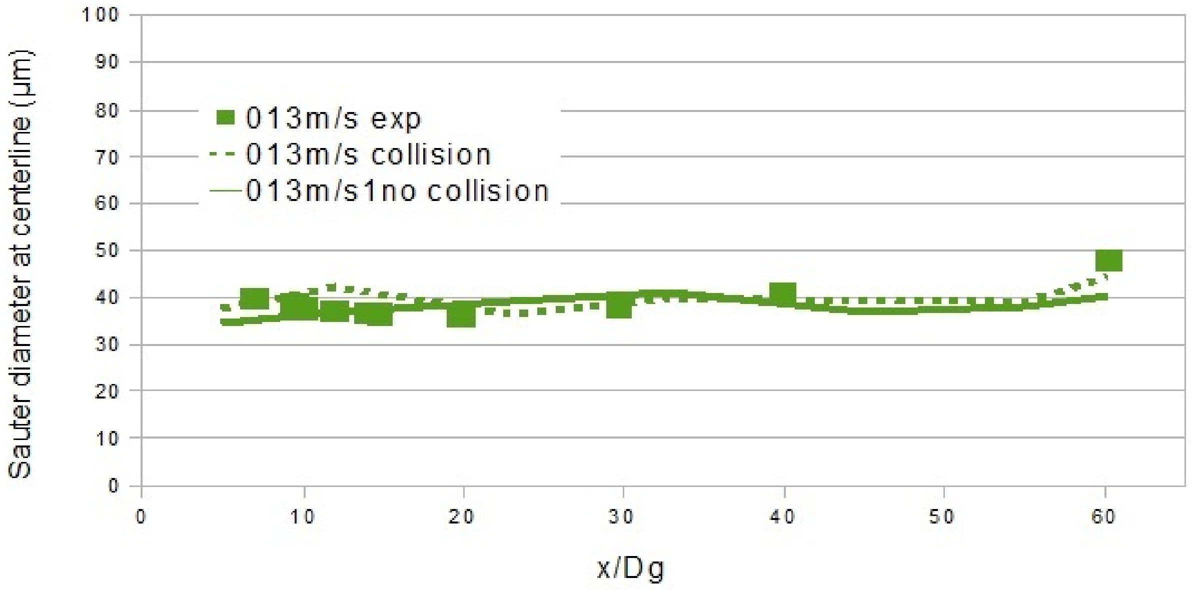

Figure 9.8: Comparison of the Sauter mean diameter at the given section with measurements in [53] and [103] in the far-field of a round water jet atomized by a high speed annular air jet. The measurements and computations with and without coalescence model are presented by symbols continuous and discontinuous lines, correspondingly. The gas velocity water velocity is held constant ($D_g = 5.6mm$, $U_g = 140m/s$), $U_{liq} = 0.13m/s$.

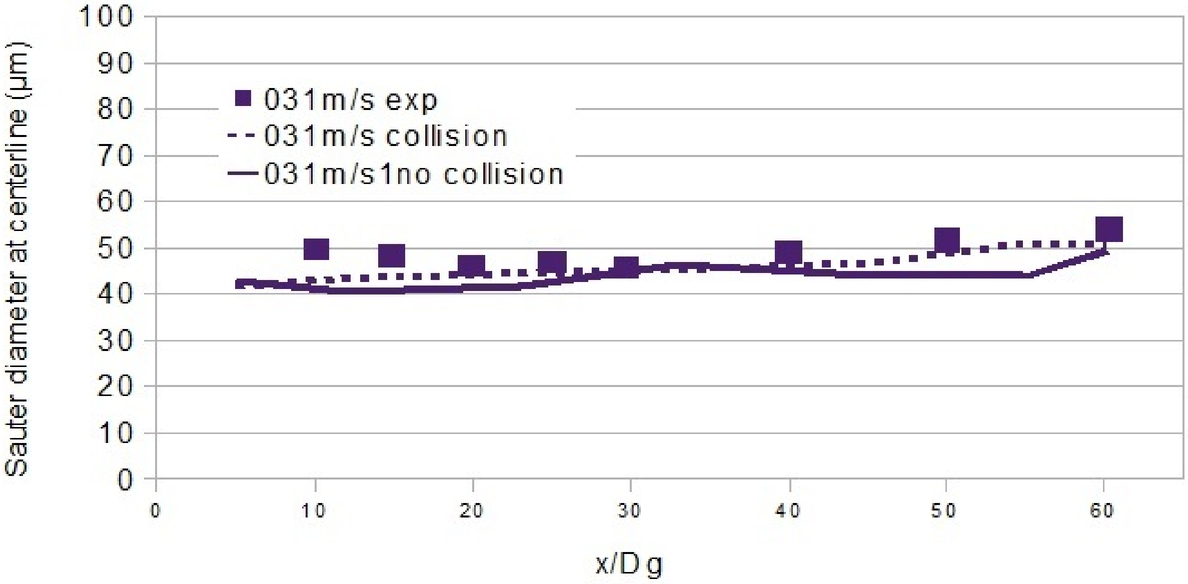

Figure 9.9: Comparison of the Sauter mean diameter at the given section with measurements in [53] and [103] in the far-field of a round water jet atomized by a high speed annular air jet. The measurements and computations with and without coalescence model are presented by symbols continuous and discontinuous lines, correspondingly. The gas velocity and water velocity are held constant ($D_g = 5.6mm$, $U_g = 140m/s$, $U_{liq} = 0.31m/s$.)

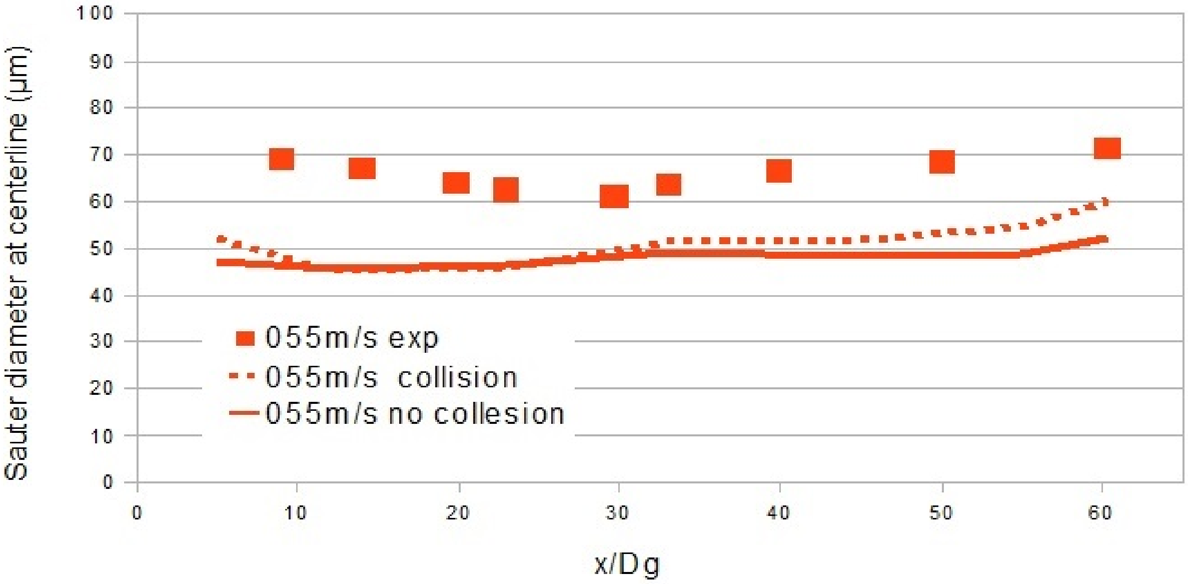

Figure 9.10: Comparison of the Sauter mean diameter at the given section with measurements in [53] and [103] in the far-field of a round water jet atomized by a high speed annular air jet. The measurements and computations with and without coalescence model are presented by symbols continuous and discontinuous lines, correspondingly. The gas velocity water velocity are held constant ($D_g = 5.6mm$, $U_g = 140m/s$), $U_{liq} = 0.55m/s$.

9.3 Conclusion

In this section the stochastic model of drops air-blast breakup, Kolmogorov´s model, was presented and validated. The computations were performed for two configurations. The first one showed quantitative results , which confirm the existence of a broad spectrum of droplet size at each spray location. The computations on the second configuration were performed for different liquid inlet velocities. The downstream Sauter mean diameter was compared to the far field spray experiment. The simulation results were in a good agreement with experimental data. Like the experimental observation the sauter mean diameter first decreased and then increased in the downstream direction. Opposite to finding in [104] the effect of coalescence was not very strong at the beginning as it was claimed as due to the existing two regions dominant by coalescence (at the beginning) and breakup (at the end). The calculation shows that in fact the effect of coalescence and breakup exist in every region of the spray. The impact of dispersion model on the breakup was compared at centerline which was not very high for the sauter diameter. Other data for the comparison of dispersion models were not available for the current configuration.

10 Summary and Outlook

Following the E-L (Eulerian Lagrangian) context, the present work aimed at studying the effect of dispersion modeling on multiphase flow properties for statistically unsteady flows. For this purpose, the study has included the essential processes that may be impacted by the turbulent particle dispersion, like

1. break up process along with four-way coupling
2. phase change phenomena
3. interaction between phases

Especially, the unsteady numerical coupling within URANS context has been adapted to capture the unsteadiness of the two-phase flows.

Three dispersion models, namely RWM-Iso, RWM-Aniso and PLM, were integrated and compared. Three configurations have been used for model appraisal with respect to their ability to retrieve unsteady behavior of the turbulent dispersion. In a vertical simple channel flow 7.1, where the unsteady effects are not very high for the near field, all three models achieved comparable results. In the far field PLM provided better results in regard to the particle velocity fluctuation, whereas the other two models show a constant particle velocity fluctuation especially in the center region.

For the shear layer configuration (see 7.2) where the unsteady effects are higher than in the vertical channel flow the RWMs underpredicte the particle velocity fluctuation too much compared to the PLM.

Based on these results, following conclusions can be drawn:

1. The use of a steady numerical coupling while including a simple dispersion model such as Random Walk Model would not return reliable results.
2. Unsteady coupling approach with advanced dispersion model such as Particle Langevin Model and unsteady simulation of carrier phase seems to be able to capture the essential dynamics of the flow.
3. With respect to unsteady simulation methods like URANS, it might be essential to use an advanced dispersion model like Particle Langevin Model for better capturing dispersion process when $\tau_p/\tau_l < 0.5$ in accordance to [44].
4. As the coupling between the disperse and carrier phase is achieved in an Eulerian level, an averaging of representative sample of particle is required. If the sample size is too small, the statistical noises may decrease the results quality.
5. The effect of dispersion modeling on the segregation prediction has been pointed out confirming previous findings by [13]. This effect suggests that advanced dispersion model on the fuel-air mixture preparation and related analysis is expected to be essential elucidating

some contradictory claims in the literature with respect to the unsteady calculations, like LES, [36], [37], [43], [41].

In order to assess the ability of the equilibrium uniform temperature evaporation models to successfully predict the mass transfer and vapor distributions, the test case experimentally investigated by Sommerfeld et al. [26], which consists of spray issuing into a co-flowing heated air stream, has been numerically studied. A systematical study of different dispersion models and their influence on mass transfer has been satisfactory carried out (see 8.2).

The results show that the PLM is able to achieve better results with respect to radial mean velocities, mean diameter and axial mean velocity fluctuations of droplets. So the simulations have shown that the PLM model allows for achieving results that agree very well with the experimental measurement of the droplet mass flux in particular in upper sections. This means that the consideration of the advanced dispersion models like PLM enables to account well for anisotropic turbulence as well as vortex structures inherent to complex turbulent two phase flows.

In order to better capture unsteady dynamics using RANS calculation, a modified SAS model (see 8.2) has been adopted. Comparisons of k-ϵ and SAS model (see 8.2) results show huge differences with respect to the fluctuating velocity in axial direction for the spray case issuing into a co-flowing heated air-stream. With regard to experimental data for the fluctuating velocity the SAS model is able to capture this behavior very well especially far away from the expansion, whereas k-ϵ model shows a very raph tendency in the near expansion region and underpredicts very strongly the far away region. The coupling of SAS model with the dispersed phase solver, LAG3D, is left for the future work.

The first step for representing inflow boundary conditions for the dispersed phase in vicinity of particle injection nozzle is achieved using stochastic model of drops air-blast breakup following the Kolmogorov´s model. Two different configurations of an air-blast atomizer were investigated. For the first configuration qualitative results showed good agreement with the experimental data with respect to coexistence of large and small droplets.
In the second configuration, the effect of different liquid inlet velocities were investigated. The downstream Sauter mean diameter was compared with the far field spray experiment. The computational values reproduce in a good agreement the experimental data: the sauter mean diameter first decreases and then increases in the downstream direction. The effect of coalescence was found not very strong at the beginning as it was claimed in other papers by existing of two regions dominate by coalescence (at the beginning) and breakup (at the end). Here the calculation showed that the effect of coalescence and breakup exist in every region of the spray.

Due to the lack of experimental data for the above configurations, the influence of dispersion models on the breakup could not be investigated. In a future work the validation of the breakup model in a complex configuration has to be accomplished.

11 Zusammenfassung und Ausblick

In der vorliegenden Arbeit wurden Effekte der Dispersion im Euler-Lagrange Kontext in Bezug auf Mehrphasenströmung untersucht. Hierbei wurde besonderes Augenmerk auf

1. Breakup Prozess sowie vierwege Kopplung
2. Verdampfung
3. Interaktion zwischen den Phasen

gelegt. Die Rechnungen wurden im URANS Kontext mit instationärer Kopplung durchgeführt.

Dabei wurden 3 Dispersionsmodelle, RWM-Iso, RWM-Aniso und PLM, zusammengefasst und miteinander verglichen. Für den Vergleich wurden 3 Konfiguration herangezogen, um die Modelle in unterschiedlichen instationäre Intensitäten zu testen und zu vergleichen.

Die erste Konfiguration war ein Vertikal Kanal, wo die instationäre Effekte vergleichsweise niedrig waren. Der Vergleich von berechneten und experimentellen Daten für Partikelgeschwindigkeit und Partikelgeschwindigkeitsfluktuationen im Inlet-Bereich der Konfiguration zeigte für alle drei Modelle gleich gute Übereinstimmung. Weit weg von dem Inlet-Bereich leistete PLM bessere Übereinstimmung mit den experimentellen Daten. Die RWMs lieferten dagegen in diesem Bereich konstante Fluktuationen.

Für die Shear-Layer Konfiguration waren die RWMs Ergebnisse für die Partikelgeschwindigkeitsfluktuationen sehr niedrig im Vergleich zu den experimentell ermittelten Partikelgeschwindigkeitsfluktuationen.
Da die instationäre Effekte in dieser Konfiguration höher im Vergleich zu dem Vertikal-Kanal waren, wurde die turbulente kinetische Energie modifiziert, indem auch die gelöste Strukturen zu dem turbulenten kinetischen Energie hinzuaddiert wurden. Bezogen auf die Ergebnisse folgende Rückschlüsse könnten gezogen werden:

1. Eine stationäre Kopplung mit einem einfachen Dispersionsmodell, z.B. RWM, führt nicht zu verlässlichen Ergebnissen.
2. Instationärer Kopplung mit einem fortgeschrittenen Dispersionsmodell, PLM, und instationäre Berechnung erfasst die grundlegende Dynamik der Strömung.
3. In instationärer Rechnung wie URANS, ist es sinnvoll ein fortgeschrittenes Dispersionsmodell, wie PLM zu verwenden, um Partikeldispersion besser zu simulieren, vor allem wenn $\tau_p/\tau_l < 0.5$ (siehe [44]).
4. Die Anzahl der Partikeln/Tropfen ist sehr wichtig für die Berechnung. Um statistisch zuverlässige Ergebnisse zu bekommen, muss die Anzahl der Tropfen/Partikeln sinnvoll gewählt werden.

5. Dispersion spielt ebenfalls eine große Rolle bei der Segregationsvorhersage und bestätigt die Ergebnisse im [13]. Die Verwendung von einfachen Dispersionsmodelle für Öl-Luft-Gemische führt zu unrealistischer Ansammlung von Tropfen/Partikeln [36], [37], [43], [41].

Um die Dispersionsmodelle im Falle von Verdampfung miteinander zu vergleichen, wurde das Equilibrium-Uniform-Temperature Verdampfungsmodell implementiert. Für die Untersuchung wurde eine Konfiguration von Sommerfeld [26] gewählt.

Die Berechnung von Verdampfung mit dem PLM zeigte eine bessere Übereinstimmung mit den experimentellen Daten in Bezug auf radiale mittlere Tropfengeschwindigkeit, mittlere Tropfendurchmesser und Tropfen mittlere axiale Geschwindigkeitsfluktuationen. Die Ergebnisse bestätigten, dass das PLM gute Anisotropie und Vortex Strukturen abbilden kann.

Um mehr Instationarität im RANS-Kontext zu bekommen, wurde eine modifizierte SAS Modell (siehe 8.2) adaptiert und für die Berechnung der Gasphase in der Verdampfungskonfiguration eingesetzt. Der Vergleich von SAS Modell und k-ϵ mit den experimentellen Daten zeigte (siehe 8.2), dass die axiale Geschwindigkeitsfluktuation mit dem SAS Model gut prädektiert wird, wobei das k-ϵ Modell eine sehr grobe Tendenz der Geschwindigkeitsfluktuationen vorhersagt.

Insbesondere weit weg vom Inlet-Bereich werden die Geschwindigkeitsfluktuationen mit dem k-ϵ Modell stark unterpredektiert. Die Kopplung von SAS Modell mit der dispersen Phase ist noch nicht abgeschlossen und wird als nächster Schritt definiert.

Ferner wurde ein stochastisches Breakupmodell, das Kolmogorov's Model, implementiert und an zwei experimentell untersuchten Airblast Atomizer validiert. In der ersten Konfiguration wurde parallel zu den experimentellen Untersuchung bestätigt, dass in allen Regionen der Konfiguration große und kleine Tropfen nebeneinander existieren.
In der zweiten Konfiguration wurde der Tropfen-Sauter-Durchmesser mit den experimentell ermittelten Tropfen-Sauter-Durchmesser verglichen. Der Vergleich zeigte sehr gute Übereinstimmung. Hierbei wurde auch der Einfluss von Koaleszenz untersucht. Im Gegensatz zu früheren Untersuchungen wurde festgestellt, dass der Einfluss von Koaleszenz nicht sehr groß ist. Ferner wurde herausgefunden, dass Koaleszenz nicht nur in bestimmten Regionen auftritt, sondern überall auftreten kann.

Mit den vorhandenen experimentellen Daten konnte der Einfluss von Dispersionsmodell auf dem Breakupmodell nicht festgestellt werden. Als Ausblick ist es Interessant, das Breakupmodell, Kolmogorov's Model, für eine komplexe Konfiguration zu berechnen und mit experimentellen Daten zu vergleichen.

Bibliography

[1] Core,J.-L. Estivalezes, S. Vincent, O. Simonin, S. Glockner, (2009): *Simulation of a fluidized bed using a hybrid Eulerian Lagrangian method for particle tracking*, to appear in Notes on Numerical Fluid Mechanics and Multidisciplinary Design. 2, 3

[2] Sadiki A., Chrigui M., Janicka J. and Maneshkarimi M. R. (2005): *modeling and Simulation of effects of turbulence on vaporization, mixing and combustion of liquid fuel sprays*, Journal of Flow, Turbulence and Combustion, 2005. 1, 9, 29

[3] Lars Davidson (2006): *Unsteady RANS*, MTF270 Turbulence Modelling

[4] Tian, L., & Ahmadi, G. (2007) *Particle deposition in turbulent duct flows-comparisons of different model predictions.* journal of Aerosol Science, **38**, 377–397 (2007).

[5] Parker, Foat, & Preston, (2008): *Towards quantitative prediction of aerosol deposition from turbulent flows* journal of Aerosol Science,**39**, 99–112. 2, 3

[6] Zahmatkesh, I. (2008): *On the importance of thermophoresis and Brownian diffusion for the deposition of micro- and nanoparticles*. International Communications in Heat and Mass Transfer, **35**, 369–375 (1995). 3

[7] Zhang, Z., & Chen. Q. (2009): *Prediction of particle deposition onto indoor surfaces by CFD with a modified Lagrangian method.*,**43**, 319–328 (1995).

[8] Cheng, Y. s.(2003): *Aerosol deposition in the extrathoracic region.*,**37**, 659–671.2

[9] Matida, E. A., Finlay, W. H., Lange, C. F., & Grgic, B. (2004): *Improved numerical simulation of aerosol deposition in an idealized mouth-throat.* . Journal of Aerosol Science, **35**, 1–19 2, 3

[10] Shi, H., Kleinstreuer, C., A-Zhang, Z. (2008): *Dilute suspension flow with nanoparticle deposition in a representative nasal airway model*. Physics of Fluids, **20**, 013301.

[11] Pope, S. (1994): *Lagrangian pdf methods for turbulent flows*.Annu. Rev. Fluid Mech., , **26**, 23–62 2
3

[12] Pope, S. b., (2000): *Turbulent Flows.*. Cambridge University Press, Cambridge, United Kingdom. ISBN 52159886., 494-505 3

[13] Horender, S. (2005): *Modeling of the vortex-structure in a particle-laden mixing-layer*.ASME Fluid Engineering Division Summer Meeting and Exhibition Houston, TX, USA, (2005). 2, 4, 5, 41, 82, 83, 85, 91, 113, 116

[14] Minier, J.-P., (1999): *Closure proposals for the langevin equation model in lagrangian two-phase flow modelling*, In Proceedings of the 3rd ASME/JSME Joint Fluids Engineering Conference. 5

[15] E. Peirano, S. Chibbaro, J.Pozorski, J.-P. Minier (2005): *Mean-field/PDF numerical approach for polydispersed turbulent two-phase flows*, **37**, 659–671. Progress in Energy and Combustion Science, **32**, 315–371 (2005). 3, 4, 5, 42

[16] Nomura, H.,Hayasaki, M., Ujiie, Y. (2007): *Effects of fine fuel particles on a lminar flame stabilized in a partially prevaporized spray stream.*. Proc. Combus. Inst. **31**(2), 2265-2272. 9

[71] Berlemont, A., Grancher, M.S., Gouesbet, G. (1995): *Heat and mass transfer coupling between vaporizing particles and turbulence using a Lagrangian approach.*. J.Heat Mass Transf.**38**, 3023-3034 3, 47

[18] Kohnen, G., Rüger, M., Sommerfeld, M. (1994): *Convergence behavior for numerical calculations by the Euler/Lagrange method for strongly coupled phases.*. FED-Vol 185, Numerical method in Multiphases Flows. ASME, Houston Texas . 4, 5, 28, 70, 73

[19] Melheim, J., Horender, S., sommerfeld, M. (2005):*Modeling of the vortex-structure in a particle laden mixing-layer.*. In: Proceeding of FEDSM 2005, ASME 2005, Houston, 19-23. 3, 28, 43

[20] Crowe, C.T., Troutt, T.R., Chung, J.N. (1996):*Numerical models for Two-phase turbulent flows.*. Ann. Rev. Fluid Mech **28**,11-43. 3, 29, 72, 73

[21] Crowe, C.T., Troutt, T.R., Chung, J.N. (1998): *Lagrangian stochastic modeling of turbulent flows. Advances in Turbulence Modeling*. Von Karmon Institute for Fluid Dynamics, Belgium 3

[22] Bart Merci, Dirk Roekaerts, Amsini Sadiki (2011): *Experiments and Numerical Simulations of Diluted spray turbulent combustion.*. Proceedings of the 1st international workshop on turbulent spray combustion 78-79 3, 4, 5, 9

[23] Chrigui, M., Ahmadi, G., Sadiki, A.(2004):*Study on interaction in spray between evaporating particles and turbulence using second-order turbulence RANS models and a Lagrangian approach.*.Prog. Comput. Fluid Dyn.**4**(3-5), 162-174 29, 43, 46, 70, 71, 72, 73, 93, 127

[24] Ahmadi, G., Cao,J., Schneider, L., Sadiki, A. (2006): *A thermodynamically formulation for chemically active multiphase turbulent flows.*. Int. J. Eng. Sci. **44**, 699–720. 29, 71, 72

[25] Lain, S., Sommerfeld, M. (2003): *Turbulence modulation in dispersed two-phase flow laden with solids from a Lagrangian perspective.*. Int. J. Heat Fluid Flow, **24**, 616–625. 29, 43, 72, 73, 74

[26] Sommerfeld, M., Qiu, H.H., Reuger, M., Kohnen, G., Spies, P.J., Meuller, D.,(1993): *Spray evaporation in turbulent flow.* Proceedings of the 2nd Int. Symp. on Engineering Turbulent Modeling and Measurements, Florence, Italy, 31 May untel 2 june, pp. 932-945.

[27] Balachandar, S., Eaton, J.K. (2010):*Turbulent dispersed multiphase flows.*.Annu. Rev. Fluid Mech., **42**, 111–133. 95, 96, 114, 116, 128

[28] Tanaka, T., Eaton, J.K. (2008):*Classification of turbulence modification by dispersed spheres using a novel dimensionless number.*.Phys. Rev. Lett. **11**, 114502 . 29

[29] Beishuizen, N.A., Naud, B., roekaerts, D.J.E.M. (2007): *Evaluation of a modified Reynolds stress model for turbulent dispersed two-phase flows including two-way coupling.*.Flow Turbul. Combust. **79**(3), 321-341 72

[30] Sadiki, A. (2005): *Extended thermodynamics as modeling tool of turbulence fluid flows.*. Trends in Applications of Mathematics to Mechanics, pp. 451-462, Shaker Verlag, Aachen 72

[31] Groh, B., Sadiki, A., Janicka, J. (2004): *Large eddy simulation of particle-laden vertical channel flow under consideration of a consistent modeling of turbulence modulation.*. In: Proceedings of the 3rd International Symposium on Two-Phase Flow Modeling and Experimentation, Pisa, Italy. 72

[32] Walklate, P.J. (1995): *A Markov-chain partilce dispersion model based on air flow data: extension to large water particles.* Bound-Lay. Meteorol. **37**, 313–318 72, 73

[33] Chrigui, M., Moesl, K., Ahmadi, W., Sadiki, A., Janica, J. (2010): *Partially premixed prevaporized kerosene spray combustion in turbulent fow*. Exp. Therm. Fluid Sci., **34**, 308–315. 43

[34] Sadiki, A., Chrigui, M., Janicka, J., Maneshkarimi, M.R. (2005): *Modeling and simulation of effects of turbulence on vaporization, mixing and combustion of liquid-fuel sprays.*. Flow Turbul. combust. **75**, 105–130. 9, 43, 72

[35] Sadiki, A., Chrigui, M., Janicka, J., Maneshkarimi, M.R. (2005): *CFD-Analysis of conjugate effects of turbulence and swirl intensity on spray combustion in a single gas turbine combustor*. ASME TURBO EXPO 2004; 14-17 June 2004; Vienna, Austria 4, 5, 43, 70, 72, 73

[36] J..M. Senoner, M. Sanjose', T. Lederlin, F. Jaegle, M. Garcia, E. Riber, B. Cuenotm L. Gicquel, H. Pitsch, T. Poinsot (2009): *Eulerian and Lagrangian Large-Eddy Simulations of an evaporating two-phase flow.* Comptes Rendus Mecanique. 28

[37] S. V. Apte, K. Mahesh, P. Moin (2009): *Large-eddy simulation of evaporating spray in a coaxial combustor* Proceedings of the combustion Institute, Volume **32**, Issue 2, pp 2247-2256 2, 3, 91, 114, 116

[38] M. Sommerfeld, H. -H. Qiu (1998): *Experimental studies of spray evaporation in turbulent flow* Int. J. Heat Fluid Flow, Issue 19 pp, 10-22 2, 3, 4, 91, 114, 116

[39] M. Sommerfeld: *Modellierung und numerische Berechnung von partiklebeladenen turbulenten Strömungen mit Hilfe des Euler/Lagrange-Verfahrens.* Shaker Verlag Aachen 1996. ISBN 3-8265-1951-5

[40] J. Ph. Carlier, M. Khalij, B. Oesterle (2005): *A Improved Model for Anisotropic Dispersion of Small Particles in Turbulent Shear Flows,* Aerosol Science and Technology, Volume 39, Number 3, March 2005 , pp. 196-205(10), France 28, 43, 69, 75, 77, 127
4, 5

[41] T. Lederlin AND H. Pitsch (2008): *Large-eddy simulation of an evaporating and reacting spray.* Center of Turbulence Research Annual Research Briefs 91, 114, 116

[42] M. Chrigui and A. Sadiki (2003): *Effects of Turbulence Modulation on Mass and Heat Transfer: 3D-Numerical Prediction Based on Coupled Advanced Models for Turbulence and Evaporation* 4th Int. Symp. On Turbulence, Heat and Mass Transfer, October 12-17, Antalya, Turkey 28, 45, 72

[43] Sanjose, N. Garcia-Rosa, Ro (2005): *Contribution of the Drift Correction Effect on Mass and Heat Transfer in Evaporating Sprays* Journal of Fluids, Proceeding of the 11th workshop on Twophase Prediction, April 5th -8th, 2005, Merseburg, Germany 91, 114, 116

[44] P. Fede, O. Simonin, P. Villedieu and K. D. Squires (2006): *Stochastic modeling of the turbulent subgrid fluid velocity along iertial particle trajectories* Proceeding of the Summer Program 2006, Center for Turbulence Research 2, 3, 4, 86, 101, 113, 115

[45] Amine Mehel, Anne Taniére, Benôit Oesterlé, Jean-Raymond Fontaine (2010): *The influence of an anisotropic Langevin dispersion model on the prediction of micro- and nanoparticle deposition in wall-bounded turbulent flows*, journal of Aerosol Science 41 729-744 2

[46] Coimbra, C. F. M., Shirolkar, J. S., and MeQuay, M. Y. (1998): *Modeling particle dispersion in a turbulent multi phase mixing layer*, J. of Wind Eng. and Ind. Aerodynam., 73, pp. 79-97 3

[47] Hishida, K., Ando, A., and Maeda, M., (1992): *Experiments on particle dispersion in a turbulent mixing layer*, Int. J. Multiphase Flow, 18 (2), pp. 181-194 3, 5

[48] Minier, J.-P., and Peirano, E., (2001): *The pdf approach to turbulent plydispersed two-phase flows*, Physics Reports, 352, pp. 112-126 4, 5, 41, 43

[49] O. Simonin, E. Deutsch and J. P. Minier, (1993): *Eulerian prediction of fluid/particle correlated motion in turbulent two-phase flows*, Applied Scientific Research, 51, p. 275-283

[50] Legg, B. J. and Raupach, M. R., (1982): *Makrov-Chain Simulation of Particle Dispersion in Inhomogeneous Flows: the Mean Drift Velocity induced by a Gradient in Eulerian Velocity Variance*, Boundary-Layer Meteorol. 24,3-13 4, 5, 44

[51] Simonin, O., (1996): *Continuum Modeling of Dispersed Turbulent Two-phase Flows.*, In VKI lectures: Combustion in Two-phase Flows, Jan 29-Feb. 2. 26, 27

[52] N. Chigier and R. D. Reitz (1996): *Regimes of jet breakup mechanisms (physical aspects) in Recent Advances in Spray Combustion : Spray Atomization Drop Burning Phenomena* edited by K. K. Kuo (AIAA, Reson), Vol.**1**, pp. 109-135. 35

[53] J. C. Lasheras and E. J. Hopfinger (2000): *Liquid jet instability and atomization in a coaxial gas stream,* Annu. Rev. Fluid Mech. **32**, 275. 7, 105, 109, 110, 111, 129

[54] T. L. Georjion and R. D. Reitz (1999): *A drop-shattering collision model for multidimensional spray computations,* J. Atomization and Sprays ,**9**,231.

[55] A. N. Kolmogorov (1941): *On the log-normal distribution of particles sizes during break-up process,* Dokl. Akad. Nauk SSSR **31**, 99. 7, 35

[56] E. A. Novikov and D. G. Dommermuth, (1997): *Distribution of droplets in a turbulent spray,* Phys. Rev. E **56**, 5479. 8

[57] E. A. Novikov (1990): *The effects of intermittency on statistical characteristics of turbulence and scale similarity of breakdown coefficients,* Phys. Fluids, A **2**, 814. 8

[124] G., Lefebvre (1989): *Atomization and Sprays,* Hemisphere Publishing Corporation, New York, ISBN 0-89116-603-3. 6, 33

[59] PILCH, M., ERDMANN C. A. (1987): *Use of breakup time data and velocity history data to predict the maximum size of stable fragments,* International Journal of Multiphase Flow, vol. **13**, Nr.6, pp. 741-757. 34, 39

[60] Techen C. M. (1947): *mean value and correlation problems connected with the motion of small particles suspended in a turbulent fluid,* Dissertation, University of Technology, Delft, Netherlands, 1947

[61] Maneshkarimi M. R. (2006): *A RANS-based CFD Analysis of Microprocesses in Turbulent Reactive Spray Configurations,* Dissertation, University of Technology, TU Darmstadt, Germany, 2006 5, 13, 127

[62] Hansell D., Kennedy I.M. and Kollmann W.,(1992): *A simulation of particle dispersion in a turbulent jet,* Int. J. Multiphase flows, **18** (1992), S. pp. 559

[63] Morsi S. A. and Alexander A. J.,(1972): *An investigation of particle trajectories in two phase flow systems,* J. Fluid Mech., **55** (1972), pp. 193-208

[64] Morsi S. A. and Alexander A. J.,(1972): *Bubbles, drops and particles,* Kluwer Academic 1978

[65] Morsi S. A. and Alexander A. J.,(1972): *numerical modeling of the hydrodynamics in a bubble column using the Euler-Lagrange approach.,* Proc. On Int. Symp. On Multiphase Flow and Transport Phenomena, Antalya, Turkey.

[66] Odar F. and Hamilton W.S.,(1964): *foces on a Sphere accelerating in a viscous fluid.,* J. Fluid Mech., 18 (1964), pp. 302-314

[67] Chrigui, M., Ahmadi, G., Sadiki, A.,(2004): *Study on Interaction in Spray between Evaporating Droplets and Turbulence Using Second Order Turbulence RANS Models and a Lagrangian Approach,* Progress in Computational Fluid Dynamics, Special issue, 2004

[68] Kohnen G. und Sommerfeld M.,(1998): *Numerische Berechnung verdampfender Sprühnebel*, Chemische Technik 50 (1998) Heft 5 pp:225-234 28

[69] Law C. K.: *Unsteady droplet vaporization with droplet heating.*, Combustion and Flame, 26: 17-22, 1976 46

[70] Park J. H., Yoon Y., Hwang S. S.(2002): *Improved Tab-Model for Prediction of Spray Droplet Deformation and Breakup,*,atomization and Sprays, 12, (2002) 387-402 46

[71] Park J. H., Yoon Y., Hwang S. S.(2002): *Heat and mass transfer coupling between vaporizing droplets and turbulence using a Lagrangian approach.*, J. of. Heat and Mass Transfer Vol.38 (1995) 3023-3034 3, 47

[72] Ferziger J.H. and Peric M.:(1999): *Computational Methods for Fluid Dynamics.*, (second edition). Springer Verlag, Berlin, Heidelberg, 1999 51, 53, 57, 58, 60, 61, 68

[73] Schäfer M.:(1999): *Numerik im Maschinenbau*, ISBN 3-540-65391-0, Springer Verlag Berlin, 1999. 57, 60, 64

[74] Stone, L. H.(1968): *Iterative solution of implicit approximations multidimensional partial differential equations*, SIAM J. Numer. Anal. Vol.5, No. 3, pp. 530-558, 1968 66, 67

[75] Stone, L. H.(1968): *Vectorized strongly implicit solving procedure for seven-diagonal coefficient matrix*, Int. J. Numer. Meth. Heat Fluid Flow, vol. 4, pp. 159-172, 1994 66

[76] Jones W.P.(1979): *Models for turbulent flows with variable density and combustion*, Prediction method for turbulent flows, Band 1979-02. Von Karman Institute for fluid dynamics, 1979

[77] Jones, W.P. and Musonge, P. (1988): *Closure of the Reynolds stress and scalar flux equations*, Phys. Fluids 31:3589-3604.

[78] Rotta J. C.: *Statistische Theorie nichthomogener Turbulenz*,, Zeitschrift für Physik, Vol. 129, pp.547-572 18, 19

[79] Boussinesq, J. (1877): *Theorie de l' ecoulement tourbillant.*, Mem. Acad. Sci., 23:46, 1877. 17

[80] Launder, B. E. und D. B. Spalding (1974): *The Numerical Computation of Turbulent Flow.*, Comp. Meth. Appl. Mech. Eng., 3: 269-289, 1974. 23

[81] David C. Wilcox (1974): *Turbulence modeling for CFD" DCW Industries.* Inc. La Canada, California 1993, ISBN 0-9636051-0-0

[82] Gatski T. B. and Speziale C. G.(1993): *On Explicit Algebraic Stress Models for Complex Turbulent Flows* J. of Fluid Mech., Vol. 254, 1993, pp. 59-78. 18

[83] Wallin S., (2000): *Engineering turbulence modeling for CFD with a focus on explicit algebraic Reynolds stress models* Doctoral Thesis, Norsteds Tryckeri AB, Stockholm, Sweden, 2000.

[84] Lumley J L, (1978): *Computational modeling of turbulent flows* 1978 Adv. Appl. Mech.18 123-76

[85] Jones W. P. (1994): In P.A. Libby and F. A. Williams, editors, *Turbulent Reacting Flows* , pp. 309-374. Academic Press, London, San Diego, New York, 1994.

[86] Launder B: E., Reece, G.J. and Rodi, W. (1975), *Progress in the development of a Reynolds-Stress Turbulence Closure*, Journal of Fluid Mechanics, 1975 Vol.68, Pt.3, pp. 537-56

[87] Crowe, C. T., Sharma, M. P. & Stock, D. E., (1977), *The particle-source-in-cell (PSICELL) model for gas-droplet flows.*, ASME Trans. J. Fluids Eng. June. 31

[88] J.K. Dukowicz, (1980), J. Comp. Phys. 35 (1980) 229. 34

[89] P.J. O'Rourke, A.A. Amsden (1987), SAE Technical Paper 87-2089, 1987. 34, 35, 40

[90] R.D. Reitz (1987), Atom. Spray Technol. 3 (1987) 307. 34, 35

[91] Sazhin, S.S. (2006) *Advanced models of fuel droplet heating and evaporation,*, Progress in Energy and Comb. Science, 32, (2006), 162-214 6

[92] Georjion, T.L., Reitz, R.D., (1999) *A drop-shattering collision model for multidimensional spray computations.*, Atomization Sprays 9, 231-254 35

[93] Lefebvre, A.H., (1989), Atomization & Sprays. Hemisphere, New York. 35

[94] Chigier, N., Reitz, R.D., (1996), *Liquid jet atomization and droplet breakup modeling of non-evaporating diesel fuel sprays.*, SAE Transactions. J. Engines 106, 127-140 35

[95] Kolmogorov A.N., (1941), *On the Log-Normal Distribution of Particles Sizes During Break-Up Process*, Dokl. Akad. Nauk. SSSR , XXXI, 2, 99-101 (1941) 35, 37

[96] Williams F.A., (1958), *Spray combustion and atomization*, Phys. Fluids, 1, 541, 1958.

[97] Dukowicz J.K., (1980), *A particle-fluid numerical model for liquid sprays*, J. Comput. Phys., 35, 229 (1980) 37

[98] Dukowicz J.K., (1980), *A Computer Program for Chemically Reactive Flows with Sprays,* LA- 11560-MS (1989) 37

[99] Gel'fand B.E., Gubin S.A., Kogarko S.M., Komar S.P.,(1975), *Singularities of the Breakup of Viscous Liquid Droplets in Shoc Waves,* J. Engng Phys., vol. 25, pp. 1140-1142. 1975. 39

[100] Kolmogorov A.N.,(1949), *On the Drops Breakup in the Turbulent Flow,* Gidromekanika, DAN. vol. LXVI, NS, pp. 825-828, 1949. 39

[101] Lasheras J.C., Villermaux E., Hopfinger E.J.,(1998), *Break-up and atomization of round water jet by a high-speed annular air jet,* J. Fluid Mech., 357, 351-379, 1998 39, 105, 107

[102] Kuznezov V.R., Sabel'nikov V.A.,(1990), *Turbulence and Combustion,* Hemisphere Publishing Corporation, 362 p., 1990. 39

[103] G. M. Faeth,,(1990), *Structure and atomization properties of dense sprays,* Int. Symp. Combustion, Pittsburgh, PA (Combustion Institute, Pittsburgh 1990) 109, 110, 111, 129

[104] Gorokhovski, M.M.,(2001), *The stochastic lagrangian model of drops breakup in the computation of liquid sprays.* Atomization Sprays 11, 505-520 7, 35, 107, 112

[105] E. Bluemcke, M. Brandt, H. Eickhoff, und C. Hassa (1993): *Particle Dispersion in Highly Swirling, Turbulent Flows,* Particle and Particle Systems Characterization 10. 3

[106] D. Stepowski, and O. Werquin 2001: *Break-up and atomization of a round water jet by a high speed annular air jet,* J. Fluid Mech. 357, 351. 105

[107] S.K., Aggarwal, A.Y., Tong and W.A. Sirignano (1984): *A comparison of vaporization models in spray calculations,* AIAA J. J.**22** (10). 1448-1457. 6, 49

[108] J. Bellan, M., Summerfield 1987: *Theoretical examination of assuptions commonly used for the gas phase surrounding a burning droplet,* Cob. Flame,**33** 107-133 6

[109] B., Abramzon W.A. Sirignano 1984: *Droplet vaporization model for spray combustion calculations,* Int. J. Heat Mass Transfer **32** 9. 1605-1618 6, 45

[110] Berlemont A., Desjonqueres PH., Guesbet G. (1990): *Particle Lagrangian simulation in turbulent Flows,*, Int. J. Multiphase Flow, 16-1, pp 19-34.

[111] R. D. Reitz (1987): *Modeling atomization processes in high-pressure vaporizing sprays.,* J. Atomization Spray Tech. **3**,309. 7, 33, 34

[112] Gosman A. D., Ionnides I. E. (1981): *Aspects of computer simulation of liqued fuelled combustors*, AIAA aerospace sciences meeting, paper 81-0323, St.louis,MO. 3, 4, 5

[113] Yuu, S., Yasukouchi N., Hirosawa Y. and Tomosada Jotaki, (1978): *Particle Turbulent Diffusion in a Dust Laden Round Jet*, The american Institute of Chemical Engineers 3, 5

[114] A. B. Liu and R. D. Reitz (1993): *Mechanism of air-assisted liquid atomization,* J. Atomization and Sprays , **3**,55. 7

[115] Domelevo K. and Sainsaulieu L. 1997: *A numerical method for the computation of the dispersion of a cloud of particles by a turbulent gas flow field*, J. Comput. Phys. 133, pp 256-278. 26

[116] Liu Z., Zheng C. and Hzou L (2002): *A joint model for turbulent spray evaporation/Combustion* Proceedings of the Combustion Institzute, Volume 29, 2002/pp. 561-568. 27, 28

[117] Domelevo K. and Sainsaulieu L. 1997: *Particle flow modeling on spiral concentrators: Benefits of dense media for coal processing*, Second international conference on CFD in the minerals and process industries CSIRO, Melbourne, Australia 1999 27

[118] Domelevo K. and Sainsaulieu L. 1997: *Solving stiff mass transfers in compositional multiphase flow models: Numerical stability and spurious solutions*, : Computational Geosciences, 1999, vol. 3, no. 2, pp. 161-183(23) 27

[119] Fluent user guide, version 6.0:

[120] Stojanovic Z., Chrigui M.,. Sadiki A., Dreizler A., Geiß S. and Janicka J.: *Experimental Inverstigation and Modeling of Turbulence Modification in a dilute Two-Phase Turbulent Flow*,10th Workshop on Two-Phase Flow Predictions, Merseburg, Deutschland, 2002 28

[121] Stojanovic Z., Chrigui M.,. Sadiki A., Dreizler A., Geiß S. and Janicka J.: *Numerical Prediction of Coal Particles Evolution Behavior in Swirled Flow with and without Combustion using an Euler-Lagrangian Coupling*,ISCC, 2003, China 28

[122] Hall, C.D.: *The simulation of particle motion in the atmosphere by a numerical random-walk model.*, Quart. J. R. Met. Soc., 101, 235-244 (1975) 4, 5

[123] Buenos Aires: *Weltenergiekonzern 2001* 1

[124] Lefebvre, A.H. : *Atomization and Sprays.*, p. 27, Hemisphere Publishing Corporation, New York, (1989). 6, 33

[125] R. S. Miller, K. Harstad und J. Bellan: *Evaluation of equilibrium and non-equilibrium evaporation models for many droplet gas-liquid flow simulations.*, Int. J. Multiphase Flow, 24:S. 1026-1055 (1998) 6

[126] Spalart, P. R., Jou, W-H. Strelets, M. and Allmaras, S.R., *Comments on the feasibility of LES for wings and on a Hybrid RANS/LES approach* , Advances in DNF/LES, Proc. First AOOSR International Conference on DNS/LES. Louisiana Tech University, eds: Chaoqun Liu, Zhining Liu and Leonidas Sakell (1997). 23

[127] Menter, F., *Two-equation eddy-viscosity turbulence model for engineering applications*, AIAA Journal, **32**, 1598–1605 (1994). 21

[128] Fröhlich, J., von Terzi, D *Hybrid LES/RANS Methods for the Simulation of Turbulent Flows*, Progress in Aerospace Science,**44/5**, 349–377 (2008). 17, 18, 21

[129] Pope, S. B., *Turbulent flows*, Cambridge Univ.Press, Cambridge, UK, (2000). 18, 23, 86, 101

[130] Bluman, G. A., Kumei, S. *Symmetries and Differential Equations*, 2nd edn. Springer Verlag (1996). 14, 19

[131] Truesdell, C., Noll, W. *The non-linear field theories of mechanics*, Third Edition, Springer-Verlag, Germany, (2004).

[132] Sadiki, A. Hutter, K. *On Thermodynamics of Turbulence: Development of First Order Closure Models and Critical Evaluation of Existing Models*, J. Non-Equilib. Thermodyn., **25**, pp. 131–160 (2000)

[133] Launder, B.E., and Sharma, B. I., *Application of Energy Dissipation Model of Turbulence to the Calculation of Flow Near a Spinning Disc*, Letters in Heat and Mass Transfer,**1, No. 2**, 131–138 (1974) 17

[134] Bourbaki, N., *Topological vector space*, Springer Verlag, ISBN: 3-540-13627-4 (1987).

[135] Horton, W., Kim, J.-H., Chagelishvili, G.D., Bowman, J.C. and Lominadze, J. G., *Angular redistribution of nonlinear perturbations: A universal feature of non-uniform flows*, PYSICAL REVIEW E **81**, 066304 (2010). 23

[136] Prandtl., L *Über ein neues Formelsystem für die ausgebildete Turbulenz*, Nachr. Akad. Wiss., Göttingen, Math-Phys. Klasse, 6–19 (1945).

[137] Rose, W.G., *Results for an attempt to generate a homogeneous turbulent shear flow*, j.Fluid Mech., **25**, 97–120 (1966). 19

[138] Sommerfeld M.;Qiu H.-H., *Experimental studies of spray evaporation in turbulent flow*, International Journal of heat and fluid flow,**19, No. 1**, 10–22(13) (1998).

[139] Rotta, J.C., *Turbulente Srtömungen*, Teuber Verlag, Stuttgart (1972).

[140] Hahn, F., *Zur Vorhersage technischer Verbrennungssysteme im Hinblik auf flüssige Brennstoffe*, Ph.D thesis, Department of Mechanical Engineering, Technische Universität Darmstadt, VDI Verlag, ISBN 978-3-18-358206-8, ISSN 0178-9414 (2009).

[141] Menter, F. R., Egorov Y., *The Scale Adaptive Simulation Method for Unsteady Turbulent Flow Prediction*, Part 1: Theory and Model Description, Flow Turbulence and Combustion, DOI 10.1007/s10494-010-9264-5 (2010). 20, 21

[142] Chien, K.-Y., *Prediction of Channel and Boundary-layer Flows with a Low-Reynolds-Number Turbulence Model*, AIAA Journal, **20, No,1**, 33–38 (1982). 23

[143] H.P. Trinh: *Modeling of Turbulence Effect on Liquid Jet Atomization.*, Marshall Space Flight Center, Alabama (2007); <https://www2.sti.nasa.gov> 7, 127

[144] Mehdizadeh A. (2010): *Direct Numerical Simulation, Lie Group Analysis and Modeling of a Turbulent Channel Flow with Wall-normal Rotation,* Dissertation, T echnical University of Darmstadt, germany, 2010 21, 23, 24

[145] Mehdizadeh A. (2010): *On the development of a spray model based on drop-size moments,* Proc. R. Soc. Lond. A, 459:1365-1394, 2003 27

[146] V. John, I. Angelov, A. A. öncül and D. $Th\grave{e}venin$ (2007): *Techniques for the reconstruction of a distribution from a finite number of moments* Chemical Engineering Science, 62:2890-2904, 2007 27

[147] D. L. Marchisio and R. O. Fox (2007): *Multiphase Reacting Flows: Modelling and Simulation* SpringerWienNewYork, 2007. 27

[148] Varaksin AY, Zaichik LI (2000): *Effect of particles on the carrier flow turbulence.* Thermophys Aeromech 7:237-248. 45

[149] Gumprich, Werner; Sadiki, Amsini; Sommerfeld, Martin (2011): *3D Simulation and Analysis of Dense Turbulent Sprays Using an Eulerian Approach coupled to the DQMOM* 13th International Conference on Numerical Combustion, Corfu, Greece, 2011. 27

[150] M. Chrigui (2005): *Eulerian-Lagrangian Approach for Modeling and Simulations of Turbulent Reactive Multi-Phase Flows under Gas Turbine Combustor Conditions* Dissertation, TUD, Germany 2005. 16, 71, 127

[151] W. Ahmadi, A. Mehdizadeh, M. Chrigui, P. Pantangi (2011):: *:Effect of unsteady calculations and their influence on the dispersion modeling* International Symposium on Multiphase flow and Transport Phenomena April 22-25, 2012, Agadir, Morocco 72, 127

[152] McGraw R. (1997): *Description of aerosol dynamics by the quadrature method of moments,* Aerosol Science and Technology, 27, 1997, pp.255-265.

List of Figures

1.1 Sketch of primary and secondary liquid jet breakup regimes [143]. 7

2.1 Two-point velocity correlation function versus the distance between two point Δx for homogeneous isotropic turbulence 12
2.2 Schematic representation of the turbulent kinetic energy spectrum as a function of the wavenumber κ for isotropic homogeneous turbulence. (ξ_0, ξ_l, ξ_T and ξ_η correspond to the very large length scales, the integral length scale, the Taylor length scale and Kolmogorov length scale, respectively.) [61] 13
2.3 Time average for any variable ϕ: a) stationary case, b) unsteady case. 16

5.1 schematic description of evaporation [23] 46

6.1 Topology and control volume notification 52
6.2 Collocated grid 53
6.3 Variables arrangement on staggered grid 54
6.4 Local coordinate system arranged in the CV central 55
6.5 Diagram for numerical steady coupling between the continuous and dispersed phases in the frame of Eulerian/Lagrangian approach [150]. 71
6.6 Diagram for numerical unsteady coupling between the continuous and dispersed phases in the frame of Eulerian/Lagrangian approach[151]. 72
6.7 Variation of the particle volume fraction (α) in the computational domain of the configuration investigated in section 7.2: (particle laden shear flow) 73

7.1 Measured size distributions of the gas beads (number fraction) [39] 75
7.2 Configuration of the vertical channel flow [39] 77
7.3 The axial velocity and turbulent kinetic energy of the gas phase in the vertical channel along the $r = y/D$ 78
7.4 Axial velocity of the particles with RWM-Iso along the $r = y/D$ 79
7.5 Axial velocity of the particles with RWM-Aniso along the $r = y/D$ 79
7.6 Axial velocity of the particles with PLM along the $r = y/D$ 80
7.7 RMS of the axial velocity of the particles with RWM-Iso along the $r = y/D$ 80
7.8 RMS of the axial velocity of the particles with RWM-Aniso along the $r = y/D$ . . 81
7.9 RMS of the axial velocity of the particles with PLM along the $r = y/D$ 81
7.10 Experimental setup computational domain (velocity field) 82
7.11 Velocity (left) and turbulent kinetic energy (right) for the gas phase: comparison of steady (dashed lines) and unsteady (lines) calculations with experimental data (dots) at axial positions $x = 10mm$,$x = 100mm$ and $x = 300mm$ 84
7.12 Velocity and turbulent kinetic energy for the gas phase: comparison of steady (dashed lines) and unsteady (lines) calculation at the axial position $x = 1200mm$. 85

7.13 Mean particle velocity and fluctuation at x=300mm, Comparison of cases X_1 and X_2. Dots (exp), red solid lines (RWM-Iso) and green dashed lines the PLM calculations, both in steady mode. 87
7.14 Mean particle velocity and fluctuation at x=300mm, Comparison of cases X_3 and X_4. Dots (exp), solid lines (RWM-Iso) and dashed lines the PLM calculations, both in unsteady mode. 88
7.15 Mean particle velocity and fluctuation at x=300mm, Comparison of cases X_4 and X_6. Dots (exp), solid lines (RWM-Aniso) and dashed lines the PLM calculations, both in unsteady mode. 89
7.16 Concentration of particles predicted by various dispersion models at x=300mm, x=700mm and x=1200mm (cases X_3, X_4 and X_6) 90
7.17 Mean concentration of particles c predicted by various dispersion models at x=300mm, x=700mm and x=1200mm (cases X_3, X_4 and X_6) 91

8.1 Test case for the verification of the evaporation model 93
8.2 Comparison of the droplet diameter and mass concentration of the implemented evaporation model (new) to the already existing evaporation model (old) 94
8.3 Test configuration for spray issuing into a co-flowing heated air-stream [26] 95
8.4 Mesh for the test configuration for spray issuing into a co-flowing heated air-stream 96
8.5 Cross sectional distributions of (top) axial mean velocity, (middle) axial RMS values of velocity and (bottom) radial mean velocity of the gas-phase along the test section using the k-ϵ model 98
8.6 Cross-sectional distributions of axial mean velocities of droplets along the test section 99
8.7 Cross-sectional distributions of radial mean velocities of droplets along the test section 100
8.8 Cross-sectional distributions of axial mean diameter of the droplets along the test section 100
8.9 Cross-sectional distributions of axial mean velocity fluctuations of droplets along the test section 101
8.10 Cross-sectional distributions of the droplet-mass flux along the chamber 101
8.11 Instantaneous picture of the axial velocity of fluid phase for the SAS (top) and k-ϵ (bottom). two dimensional cut through the symmetry axis 102
8.12 Cross sectional distributions of (top) axial mean velocity, (middle) axial RMS values of velocity and (bottom) radial mean velocity of the gas-phase along the test section 103

9.1 Coaxial jet nozzle configuration 106
9.2 Computational domain with $9 * 10^5$ CV 107
9.3 Computed spatial distributions of drops at different time in the spray of water atomizing by the coaxial air jet ($U_{liq} = 0.8m/s$, $U_g = 115m/s$). The ratio of gas-to-liquid momentum at the exit of injector is equal to 26.4. The vertical lines are given in m. 108
9.4 An example of zooming of spatial distributions of drops in the spray presented in Fig.9.3. A co-existence of droplets of different size is seen at every region of spray 108

9.5 Comparison of the Sauter mean diameter at the given section with measurements in Refs. [53] and [103] in the far-field of a round water jet atomized by a high speed annular air jet. The measurements and computations without coalescence model are presented by symbols, $1 * 10^5 CV$ blue, $3 * 10^5 CV$ yellow and $9 * 10^5 CV$ green. The gas velocity and water velocity is held constant ($D_g = 5.6mm$, $U_g = 140m/s$), $U_{liq} = 0.13m/s$. 109

9.6 Comparison of the Sauter mean diameter at the given section with measurements in [53] and [103] in the far-field of a round water jet atomized by a high speed annular air jet. The measurements and computations without coalescence model are presented by symbols and continuous lines, correspondingly. The gas velocity is held constant ($D_g = 5.6mm$, $U_g = 140m/s$), while varying the velocity of water, $U_{liq} = 0.13; 0.31; 0.55m/s$. 109

9.7 Comparison of the Sauter mean diameter at the given section with measurements in [53] and [103] in the far-field of a round water jet atomized by a high speed annular air jet. The measurements and computations without coalescence model are presented by symbols and discontinuous lines, correspondingly. The gas velocity is held constant ($D_g = 5.6mm$, $U_g = 140m/s$), while varying the velocity of water, $U_{liq} = 0.13; 0.31; 0.55m/s$. 110

9.8 Comparison of the Sauter mean diameter at the given section with measurements in [53] and [103] in the far-field of a round water jet atomized by a high speed annular air jet. The measurements and computations with and without coalescence model are presented by symbols continuous and discontinuous lines, correspondingly. The gas velocity water velocity is held constant ($D_g = 5.6mm$, $U_g = 140m/s$), $U_{liq} = 0.13m/s$. 110

9.9 Comparison of the Sauter mean diameter at the given section with measurements in [53] and [103] in the far-field of a round water jet atomized by a high speed annular air jet. The measurements and computations with and without coalescence model are presented by symbols continuous and discontinuous lines, correspondingly. The gas velocity and water velocity are held constant ($D_g = 5.6mm$, $U_g = 140m/s$, $U_{liq} = 0.31m/s$.) 111

9.10 Comparison of the Sauter mean diameter at the given section with measurements in [53] and [103] in the far-field of a round water jet atomized by a high speed annular air jet. The measurements and computations with and without coalescence model are presented by symbols continuous and discontinuous lines, correspondingly. The gas velocity water velocity are held constant ($D_g = 5.6mm$, $U_g = 140m/s$), $U_{liq} = 0.55m/s$. 111

Publications

Journals/Conferences

Ahmadi, W. ; Chrigui, M. ; Sadiki, A. (2010): *Effect of evaporation on the combustion behaviour of kerosene spray flame. ASME-Turbo expo*, ASME-Turbo expo. [Conference]

Chrigui, M. ; Moesl, K. ; Ahmadi, W. ; Sadiki, A. ; Janicka, J. , (2010): *Partially premixed prevaporized kerosene spray combustion in turbulent flow.*, In: Experimental Thermal and Fluid Science, 34 (3) pp. 308-315, [Journal].

Chrigui, M. ; Moesl, K. ; Ahmadi, W. ; Sadiki, A. ; Janicka, J. , (2009) : *Partially Premixed Prevaporized Kerosine Spray Combustion in Turbulent Flow.*, . In: 6th Md. Com. Symp., Corsica [Workshop]

W. Ahmadi, M. Chrigui, A. Sadiki and J. Janicka, (2010) : *Influence of air temperature and evaporation zone length on evaporation and combustion.*, 7th international conference on multiphase flow ICMF 2010 Tampa, FL USA [Conference]

W. Ahmadi, M. Chrigui, A. Sadiki and J. Janicka (2011): *Toward the Impact of fuel evaporation-combustion interaction on spray combustion in gas turbine combustion chamber. Part 1: Effect of partial fuel vaporization on spray combustion*, Experiments and numerical simulations of diluted spray turbulent combustion, proceedings of the 1st international workshop on turbulent spray combustion [Book].

W. Ahmadi, M. Chrigui, A. Sadiki and J. Janicka (2011): *Toward the Impact of fuel evaporation-combustion interaction on spray combustion in gas turbine combustion chamber. Part 1: Effect of partial fuel vaporization on spray combustion*, Experiments and numerical simulations of diluted spray turbulent combustion, proceedings of the 1st international workshop on turbulent spray combustion [Book].

W. Ahmadi, M. Chrigui, A. Sadiki and J. Janicka (2010): *'Effect of Fuel-Evaporation Zone Length on Spray Combustion in a Gas Turbine*, ILASS - Europe 2010, 23rd Annual Conference on Liquid Atomization and Spray Systems, Brno, Czech Republic. [Conference].

W. Ahmadi, A. Mehidzade, M. Chrigui, P. Pantangi, A. Sadiki (2012): *Effect of unsteady calculations and their influence on the dispersion modeling*, International Symposium on Multiphase flow and Transport Phenomena April 22-25, 2012, Agadir, Morocco. . [Conference].

W. Ahmadi, A. Mehidzade, A. Sadiki (2012): *Analysis of Dispersion Process of Evaporating Spray Droplets Using Novel Scale Adaptive Simulation Approach coupled to a Langevin Dispersion Model*, ICLASS - Europe 2012, 12th International Conference on Liquid Atomization and Spray Systems, Heidelberg, Germany. [Conference].

Curriculum Vitae

Name	Wahidullah Ahmadi	
Birthdate	04.03.1982	
Birthplace	Kabul	
Highschool	08/1997 - 06/1999	Comprehensive school Joachim-Schumann-Schule Babenhausen Secondary school certificate
Highschool	08/1999 - 08/2002	Bachgauschule Babenhausen University-entrance diploma
University	10/2002 - 01/2009	Technische Universität Darmstadt Diploma in Mechanical Engineering
Employer	07/2008 - 05/2012	Technische Universität Darmstadt at the department of Energy and Power Plant Technology (EKT) Prof. Dr.-Ing. Johannes Janicka
Employer	09/2012 -	Freudenberg Sealing Technology (FST) in Weinheim at the department of Advanced Product Development (APD)